Title

A Novel Biomarker for Disease: Using Biophysical Cues to Detect, Treat, and Study Cancer

Author

Zhang, Shirley

Publication Date

2018

UNIVERSITY OF CALIFORNIA,
IRVINE

A Novel Biomarker for Disease: Using Biophysical Cues to Detect, Treat, and Study Cancer

DISSERTATION

submitted in partial satisfaction of the requirements
for the degree of

DOCTOR OF PHILOSOPHY

in Biomedical Engineering

by

Shirley Xian Zhang

Dissertation Committee:
Associate Professor Weian Zhao, Chair
Assistant Professor Michelle Digman
Associate Professor Wendy Liu

2018

DEDICATION

To

my mother and father

for support and inspiration
for paving the way with sacrifice and hard work

And to
my better half

for believing in me on days when I myself did not

TABLE OF CONTENTS

LIST OF FIGURES

LIST OF TABLES

ACKNOWLEDGMENTS

Firstly, thank you to Dr. Weian Zhao for the opportunities, as well as your continued support and encouragement. I am constantly inspired by your work ethic and your willingness to take chances, to try new things and to think big; these are philosophies that I will carry with me in the future thanks to your mentorship. Thank you also to Dr. Michelle Digman and Dr. Wendy Liu, for serving on my committee, for being excellent collaborators, and for being approachable and supportive mentors throughout my time at UCI.

Thank you to all Zhao Lab members, past and present. To Dr. Jerry Liu, I cannot thank you enough for taking me under your wing all those years ago. I have learned so much from you, and I greatly appreciate not only your mentorship but your friendship. To Henry P. Farhoodi and Menglu Han, thank you for your hard work and for always lending an ear when I needed it. To Mengrou "Mary" Lu and Claire C. Chen, it was a privilege to have worked with you and learn from you. To Chi Wut "William" Wong and Lily P. Nguyen, to see students like you be so dedicated and passionate was an inspiration. To Dr. Wenbin "Vincent" Liao, Dr. Aude Ségaliny, Dr. Egest J. Pone, Dr. Emily Guo, and Dr. Jan Zimak, thank you for imparting some of your vast knowledge over the years, for encouraging me to keep going and for being exemplary scientists that I look up to. The best teachers are sometimes the ones who make you realize how much you do not yet know.

Thank you to all those outside of the lab who collaborated and helped on the scientific details and technical difficulties. Thank you to Dr. Jenu V. Chacko for support on imaging, Dr. Devon A. Lawson for animal models, and Dr. Felix Grun for mass spectrometry. Thank you also to Dr. Shivani Sharma at UCLA for assisting with the AFM, and thank you to Dr. Adam

Engler at UCSD for sharing your technical knowledge. None of these were easy to accomplish, but would have been impossible without your help.

Last but by no means least, thank you to all of the friends who have gone through this journey with me.

CURRICULUM VITAE

Shirley Xian Zhang

EDUCATION

University of California, Irvine	Irvine, CA
Ph.D., Biomedical Engineering	2013 - 2018
University of California, Irvine	Irvine, CA
M.S., Biomedical Engineering	2013 - 2016
University of California, San Diego	La Jolla, CA
Bachelor of Science, Bioengineering (Biotechnology)	2009 - 2013
Cum Laude	

RESEARCH EXPERIENCE

Department of Pharmaceutical Sciences (Zhao Lab) ▪ Engineering of human mesenchymal stem cells and cancer cells ▪ In vitro, ex vivo, and in vivo assessment of engineered mesenchymal stem cells for cancer therapy	UCI Jan 2014 – Present
Department of Biomedical Engineering (George Lab) ▪ Induced and cultured cardiomyocytes using human induced pluripotent stem cells (iPSCs) ▪ Tested effects of decellularized cardiac extracellular matrix on stem cell differentiation	UCI Aug 2013 – Dec 2013
Department of Biomedical Engineering (Liu Lab) ▪ Mechanical testing of extracellular matrix materials ▪ Assessed effects of cell culture substrate mechanical properties on macrophage polarization	UCI Jun 2013 – Aug 2013
Department of Bioengineering (Christman Lab) ▪ Cardiac tissue histology, immunohistochemistry and image analysis	UCSD May 2011 – May 2013

- Experience with small animal surgery and in vivo experiments
- Work with injectable and degradable biomaterials

Department of Physiology (Soeller Lab) — University of Auckland
Study Abroad – Pacific Rim Experiences for Undergraduates (PRIME) — Jun 2012 – Aug 2012

- Co-localization of intracellular proteins in cardiomyocytes using super-resolution stochastic imaging
- Cell immunofluorescent staining

Jacob’s School of Engineering (Fainman Lab) — UCSD
Sept 2009 – Mar 2011

- Fabrication of microfluidic and nanofluidic chips with PDMS

PUBLICATIONS

Shirley X. Zhang, Linan Liu, and Weian Zhao. "Targeting Biophysical Cues: a Niche Approach to Study, Diagnose, and Treat Cancer." *Trends in Cancer* 4.4 (2018): 268-271.

Linan Liu †, **Shirley X. Zhang** †, Wenbin Liao, Henry P. Farhoodi, Chi W. Wong, Claire C. Chen, Aude I. Ségaliny, Jenu V. Chacko, Lily P. Nguyen, Mengrou Lu, George Polovin, Egest J. Pone, Timothy L. Downing, Devon A. Lawson, Michelle A. Digman, Weian Zhao*. “Mechano-Responsive Stem Cells to Target Cancer Metastases Through Biophysical Cues.” *Science Translational Medicine*, 9.400 (2017): eaan2966. †: co-first authors

Claire C. Chen, Linan Liu, Fengxia Ma, Chi W. Wong, Xuning E. Guo, Jenu V. Chacko, Henry P. Farhoodi, **Shirley X. Zhang**, Jan Zimak, Aude Ségaliny, Milad Riazifar, Victor Pham, Michelle A. Digman, Egest J. Pone and Weian Zhao. “Elucidation of exosome migration across the blood-brain barrier model in vitro.” *Cellular and Molecular Bioengineering*, 9.4 (2016): 509-529.

Wenbin Liao, Victor Pham, Linan Liu, Milad Riazifar, Egest J Pone, **Shirley Xian Zhang**, Fengxia Ma, Mengrou Lu, Craig M. Walsh and Weian Zhao. “Mesenchymal stem cells engineered to express selectin ligands and IL-10 exert enhanced therapeutic efficacy in murine experimental autoimmune encephalomyelitis.” *Biomaterials*, 77 (2016): 87-97.

Liu, Linan, Shirley X. Zhang, Rangoli Aeran, Wenbin Liao, Mengrou Lu, George Polovin, Egest J. Pone, and Weian Zhao. "Exogenous marker-engineered mesenchymal stem cells detect cancer and metastases in a simple blood assay." *Stem cell research & therapy*, 6.1 (2015): 181.

Suarez, Sophia L., Aboli A. Rane, Adam Muñoz, Adam T. Wright, Shirley X. Zhang, Rebecca L. Braden, Adah Almutairi, Andrew D. McCulloch, and Karen L. Christman. "Intramyocardial injection of hydrogel with high interstitial spread does not impact action potential propagation." *Acta biomaterialia*, 26 (2015): 13-22.

Sonya Sonnenberg, Aboli A. Rane, Cassie J. Liu, Nikhil Rao, Gillie Agmon, Sophia Suarez, Raymond Wang, Adam Munoz, Vaibhav Bajaj, Shirley Zhang, Rebecca Braden, Pamela J. Schup-Magoffin, Oi Ling Kwan, Anthony N. DeMaria, Jennifer R. Cochran, and Karen L. Christman. “Delivery of an engineered HGF fragment in an extracellular matrix-derived hydrogel prevents negative LV remodeling post-myocardial infarction.” *Biomaterials*. 45 (2015): 56-63.

PRESENTATIONS

“A Cell-based Stiffness Sensor to Study and Treat Disease via Biophysical Cues” Biomedical Engineering Society Annual Meeting. Atlanta, GA. 9 Oct 2019.

“Mechano-Responsive Stem Cells to Target Cancer Metastasis Through Biophysical Cues.” MechBio Conference 2018. Irvine, CA. 26 Jul 2018. *Poster Award.*

“Mechano-Responsive Stem Cells to Target Cancer Metastasis Through Biophysical Cues.” SABPA Annual Biomedical Forum. Irvine, CA. 29 Apr 2017. *Poster Award.*

“Engineered Cells to Treat Tissue Fibrosis.” Biomedical Engineering Society Annual Meeting. Tampa, FL. 9 Oct 2015.

“A Stem Cell Approach for Cancer Blood Test.” Chao Family Cancer Center Retreat 2015. Palm Springs, CA. 17 Sept 2015.

“A Stem Cell Approach for Cancer Blood Test.” Stem Cell Summit 2015. Boston, MA. 27 Apr 2015.

“Assessment of 3-D Extracellular Matrix Scaffold Mechanical Properties and Effects on Macrophage Polarization.” UC Irvine Summer Research Symposium. Irvine, CA. 15 Aug 2013.

“Assessment of Swelling and Degradation Time of PEG-based Polymers.” UCSD Summer Research Conference. La Jolla, CA. 11 Aug 2011.

PATENTS

Liu L., Zhao W., Eckert M.A., Liao W., Kang D.-K., Pone E.J., **Zhang S.X.** & Lu M. 2015. Systems for Detecting, Monitoring or Treating Diseases or Conditions Using Engineered Cells and Methods for Making and Using Them. UC Case No. 2015-660-1, filed April 2015. Provisional Patent.

DESIGN PROJECTS

Department of Bioengineering (Cabrales Lab)	UCSD
Senior Design Project	Sept 2012 – June 2013

- Design, fabrication, and presentation of a fluidics device to separate erythrocytes according to cell deformability
- LabVIEW programming

TEACHING

Department of Biomedical Engineering	UCI
Teaching Assistant	Mar 2017 – June 2017
Department of Biology	UCSD
Teaching Assistant	Sept 2011 – Dec 2011

AWARDS/FELLOWSHIPS

Edwards Lifesciences CARE Fellowship, 2014-2016
UCSD Amgen Scholar, 2011
UCSD Regents Scholar, 2009-2013
Robert C. Byrd Honors Scholarship, 2009-2011

ABSTRACT OF THE DISSERTATION

A Novel Biomarker for Disease: Using Biophysical Cues to Detect, Treat, and Study Cancer

By

Shirley Xian Zhang

Doctor of Philosophy in Biomedical Engineering

University of California, Irvine, 2018

Professor Weian Zhao, Chair

In recent years, cancer research has increasingly focused on the mechanobiology of the tumor microenvironment (TME). Biophysical cues, such as mechanical properties or forces within a tumor, have proven to be just as important in influencing cell behavior as biochemical or molecular cues. The TME, often characterized by increased fibrillary collagen deposition and crosslinking and increased elastic modulus, has distinct biophysical cues which can act as a biomarker for cancer. Cells, with their innate ability to respond to differences in their mechanical environment, can thus be engineered to utilize biophysical cues to specifically target tumors. Using this ideology, we have created a mechano-

responsive cell system (MRCS) to specifically home to and target cancer metastases and deliver therapeutics. MRCS engineered to selectively activate and express cytosine deaminase when in contact with increased substrate stiffness were able to locally convert an inactive prodrug to an active chemotherapeutic drug on tumor regions of metastatic lungs, with minimal off-target side effects on less stiff, healthy tissues. In addition to therapeutic applications, engineered cell sensors can be used as tools to study cancer mechanobiology. There remain many unanswered questions surrounding how the TME and resident cells affect each other. Currently available tools to measure mechanical properties of tissues at a cellular level are insufficient to answer these questions. Cell-based stiffness sensors which can report their response to their microenvironment are a potential new tool which can be used to address unknowns, such as how the TME evolves during cancer progression, how biophysical cues influence malignancy and metastasis, and if the different mechanical properties within a tumor contribute to tumor heterogeneity and drug resistance. This platform technology can also be applied to other diseases characterized by increased tissue stiffness, such as fibrosis. With the advancement of imaging and gene-editing technologies, as well as increasing awareness and interest in mechanomedicine, the potential applications of mechano-responsive cells are endless.

CHAPTER 1:
INTRODUCTION

Authors: <u>Shirley X. Zhang</u>[1-3], Linan Liu[3,4], Jan Zimak[3,4], Weian Zhao[1-6]

Affiliations:

[1]Department of Biomedical Engineering, University of California-Irvine, Irvine, California, 92697, USA.

[2]Edwards Life Sciences Center for Advanced Cardiovascular Technology, University of California-Irvine, Irvine, California, 92697, USA.

[3]Sue and Bill Gross Stem Cell Research Center, 845 Health Sciences Road, University of California-Irvine, Irvine, California, 92697, USA.

[4]Department of Pharmaceutical Sciences, University of California-Irvine, Irvine, California, 92697, USA.

[5]Chao Family Comprehensive Cancer Center, University of California-Irvine, Irvine, California, 92697, USA.

[6]Department of Biological Chemistry, University of California-Irvine, Irvine, California, 92697, USA.

1.1 Biophysical Cues in Cancer

Previously, research on cancer onset and disease progression has focused on the roles of various biochemical and molecular factors (e.g., oncogenes and their pathways) in tumors. However, it is now acknowledged that tumor cells, rather than acting alone, are surrounded by a complex tumor microenvironment (TME) of extracellular matrix (ECM) and subjected to a variety of biophysical cues, including direct mechanical forces such as shear or compression, and physical material properties of the ECM such as topography, porosity, and stiffness, all of which can be just as important as soluble factors in influencing cancer behavior.

Physicians have long used physical palpation to detect cancer nodules, as many cancers have tumor stroma significantly stiffer than healthy tissues [1], but we now know that this stiffness difference is primarily due to collagen density, crosslinking, and fiber linearization within the tumor microenvironment (TME) [2-4]. Increased tissue stiffness facilitates tumor growth, invasion, and metastasis and can affect treatment efficacy and resistance [1, 5].

This chapter will focus on biophysical cues in the cancer microenvironment, particularly on how we can use them as novel targets to interrogate cancer mechanobiology *in vivo* to better study cancer biology and to develop next-generation cancer diagnostics and therapeutics for cancer and metastasis (Fig. 1.1).

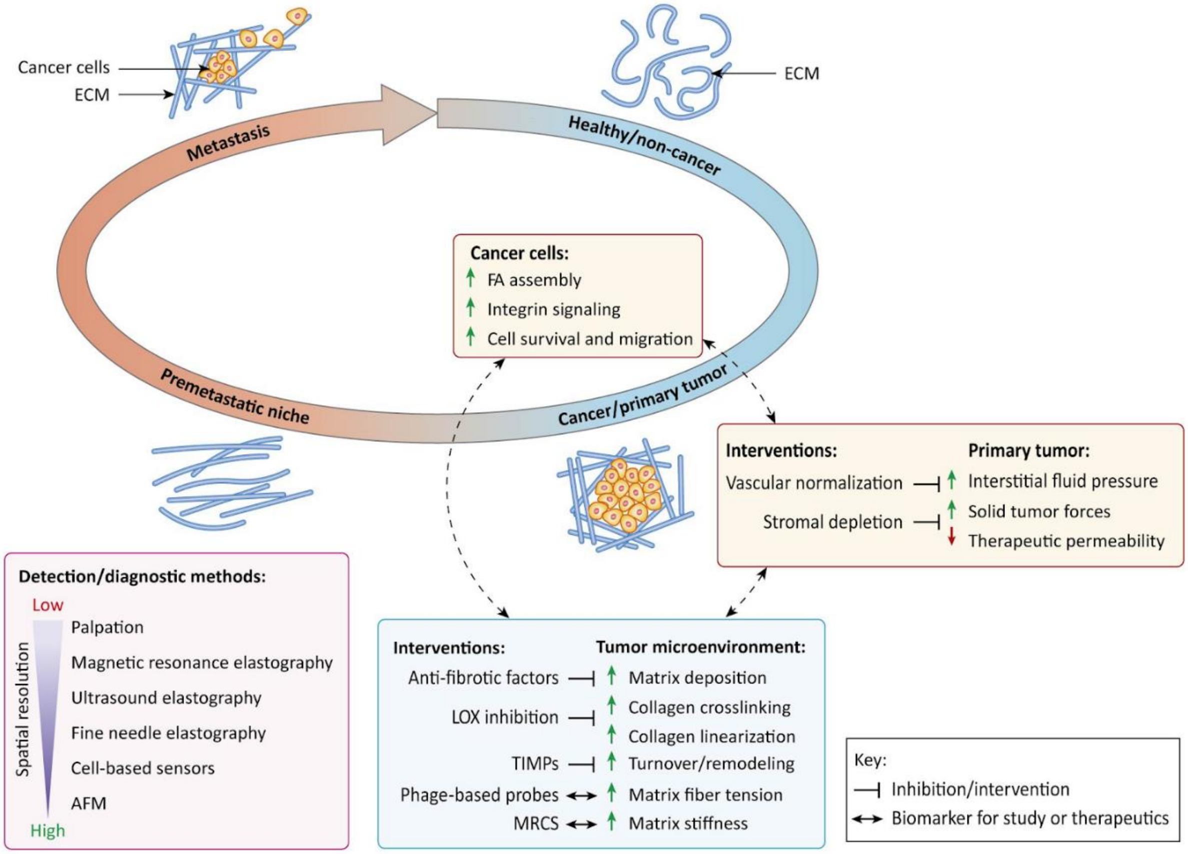

Figure 1.1. Biophysical cues as novel targets for interrogating, detecting and treating cancer and metastasis.

As cancer develops, the surrounding microenvironment undergoes biophysical changes which promote tumor proliferation and invasion, creating a feedback loop of cancer growth and metastasis. The unique biophysical properties of the tumor microenvironment present potential targets for the study, diagnosis, and treatment of cancer. Abbreviation: ECM, extracellular matrix; FA, focal adhesion; LOX, lysyl oxidase; TIMPs, tissue inhibitors of metalloproteinase; MRCS, mechano-responsive cell system; AFM, atomic force microscopy.

1.2 The Normal and Diseased Cell Microenvironment

Cells can experience different types of biophysical cues, including direct mechanical forces such as shear or compression, and physical material properties of the ECM such as topography, porosity, and stiffness. The process by which cells translate these mechanical signals in their environment to biological responses is called mechanotransduction.

Under normal conditions, the ECM maintains a homeostasis and cells experience typical biophysical cues whereas this homeostasis is perturbed in disease states like cancer [6]. The tumor stroma in breast cancers, for example, can be 10 times stiffer than normal breast tissue [7]. This difference between tumor and normal ECM is largely due to an increase in deposition of fibrillar ECM components such as collagen, as well as increased ECM crosslinking and linearization, driven in part by increased accumulation of proteins such as lysyl oxidase (LOX) [8, 9]. This increased matrix stiffness increases cytoskeletal tension, prompting the assembly of focal adhesions and integrin clustering. This leads to increased integrin-dependent mechanotransduction in cancer cells, promoting growth and migration and increasing malignancy and metastatic potential [9]. For instance, highly linearized collagen fibers on the boundaries of tumors can contribute to increased migration of cells away from the primary tumor, leading to more invasive metastases and poorer patient outcomes [8]. Dense and crosslinked ECM can locally create favorable sites for cancer cell colonization and survival, known as premetastatic niches. Finally, and abnormal ECM can also physically create barriers which limit the permeability of drugs or immune cells, hindering therapeutic success.

1.3 The Metastatic Niche

Cancer metastases account for over 90% of cancer deaths. However, there are currently no effective and selective treatments that directly target metastatic cancer. In particular, approximately 20-30% of women worldwide will develop invasive breast cancer during their lifetime, leading to over 500,000 deaths a year due to metastasis from the breast to other organs [10, 11], with a median survival of only 2 to 3 years [12, 13]. Surgical resection of widespread metastases is generally not feasible, whereas various classes of chemotherapeutic drugs are ineffective at treating disseminated cancer and often have severe side effects. Current therapy for metastatic breast cancer therefore focuses on prolonging survival and providing palliative care [10, 13-15]. In addition, tumors can develop resistance to many existing drugs through various mechanisms that are in part due to cancer heterogeneity, and this may account for cancer recurrence [10, 16].

Important roles for matrix stiffness in driving breast cancer metastasis have been elucidated [4, 6]. Specifically, increased matrix stiffness, which is primarily driven by increased collagen deposition and crosslinking by lysyl oxidase (LOX) proteins, promotes breast cancer migration, invasion, cell plasticity, and eventual metastasis, primarily through regulation of integrin signaling [9]. LOX accumulation spatially correlates with the presence of metastases in both mouse models of metastasis and human patients [4, 17]. In mouse models of breast cancer metastasis, secretion of LOX by the primary breast tumor stimulates collagen crosslinking in discrete areas of the lung that promote formation of metastases [17-21]. Deposition of LOX at the metastatic niche correlates with both collagen linearization and formation of collagen-collagen covalent bonds in the lung parenchyma, both of which dramatically increase matrix stiffness [9]. Therefore, we reasoned that the distinctive mechanical properties of the metastatic niche might offer a viable target for the development of diagnostics and therapeutics specifically targeting metastases.

1.4 Measuring Biophysical Cues

Since the physical properties of the tumor microenvironment differ from those of normal tissue, this difference can be used as a biomarker to study, detect, or treat cancer. Nevertheless, it remains difficult to study the mechanics of cancer *in vivo* at a cellular level since current measurement modalities either require invasive biopsies or lack spatial resolution.

Imaging modalities such as ultrasound and elastography are capable of noninvasive, longitudinal measurements *in vivo* but have limitations in spatial resolution and feature size [22]. Conversely, AFM, microrheology, and traction force microscopy have high spatial resolution but cannot be used *in vivo* and only provide surface measurements [23, 24]. Techniques such as FRET-based molecular sensors, magnetic tweezers and optical traps tend to interrogate particular molecular pathways but fail to characterize mechanobiology at a tissue level [25-28]. Recently, however, tools have been developed such as phage-based probes which can discriminate between relaxed or strained fibers of fibronectin, one of the predominant components of the tumor ECM [29], and the Fine Needle Elastography device which can locally determine the mechanical properties of tumor nodules with high precision and resolution [22]. Such technologies can then be applied for earlier detection of developing tumors and premetastatic niches, using high ECM strain and tumor stiffness as a biomarker which can be vital for therapeutic intervention, since highly fibrotic and stiff tumor environments have also been linked to poorer patient prognosis and higher rate of recurrence [9].

Despite technological advances, a critical barrier to further understanding tumor progression and the relationship with biophysical cues lies in the limitations of current technologies to characterize physical properties of tissues at a cellular resolution in their native environment.

1.5 Approaches to Targeting Biophysical Cues

Therapeutic strategies have mostly focused on altering the ECM of the tumor microenvironment. If increased ECM deposition and stiffness contribute to cancer growth, then inhibiting this process and restoring ECM homeostasis should potentially slow or prevent disease progression. Approaches including lysyl oxidase (LOX) inhibition to prevent collagen crosslinking [9], angiotension inhibition to reduce collagen and hyaluronan production [30], and stromal depletion through drugs like nab-paclitaxel [31] have shown promise in reducing tumor stiffness and improving drug penetration. However, the exact mechanisms of many of these pathways that affect ECM deposition are still unknown, with trials targeting other molecular targets such as tissue inhibitors of metalloproteinase (TIMPs) suffering from low specificity and unexpected toxicity [6], and ablating the tumor stroma completely by inhibiting fibroblast activation led to uncontrolled tumor growth [32].

A different approach, rather than targeting molecular factors which modulate ECM, is to directly target the biophysical cues of the ECM instead. Altered ECM states such as increased stiffness persist for long periods of time in the body and have lower heterogeneity compared to protein or genetic markers for cancer, making them more reliable biomarkers.

For example, increased breast density is associated with 30% of breast cancers, whereas well-known genetic mutations such as BRCA1 and BRCA2 only account for 5% of breast cancers [33].

To target increased tissue stiffness to treat tumors, a mechano-responsive cell system (MRCS) has been recently developed which can specifically respond to high stiffness to drive the expression of an enzyme, cytosine deaminase (CD) which converts an inactive chemotherapy drug (5-FC) to an active state (5-FU) (Fig. 1.2A) [34]. The system utilizes mesenchymal stem cells, which have previously been demonstrated to have the ability to respond to matrix elasticity to preferentially drive differentiation [35] and can be engineered to express different reporter or therapeutic proteins. MRCS uses the re-localization of the transcriptional regulators YAP (Yes-associated protein) and TAZ (transcriptional co-activator with PDZ-binding motif) [36] which occurs on stiff substrates to locally drive the expression of CD in the presence of high tissue stiffness found in tumor microenvironments.

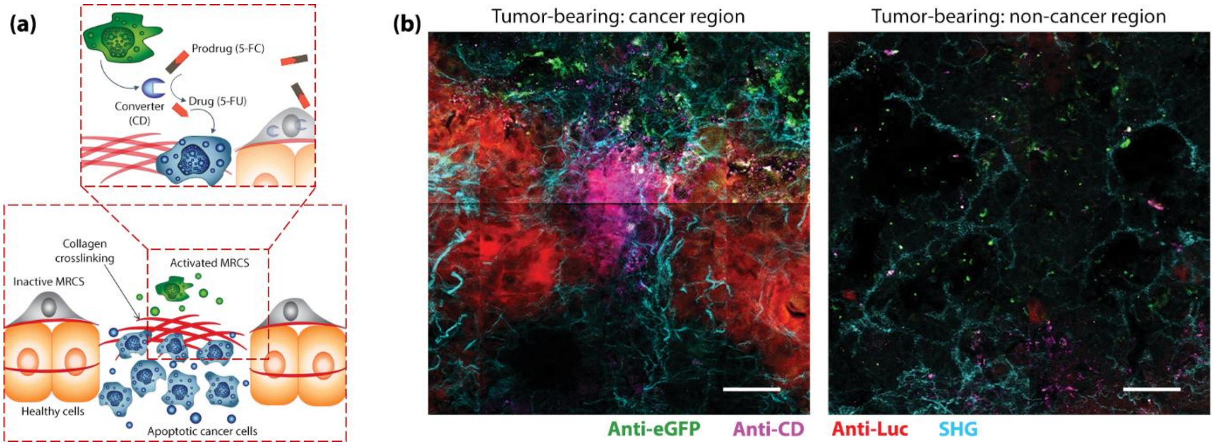

Figure 1.2. Mechano-responsive cell system (MRCS) targets biophysical cues to deliver cancer therapeutics.

(a) MRCS are selectively activated on stiff tissue to treat cancer by producing cytosine deaminase (CD) to convert prodrug 5-Fluorocytosine (5-FC) to active chemotherapy drug 5-Fluorouracil (5-FU). **(b)** Immunohistochemistry of frozen sections of tumor-bearing lungs from NOD *scid* gamma (NSG) mice 24 hours after infusion of MRCS, showing the selective release of CD (magenta) on cancer regions of the lung (left), but not on non-cancer regions (right). MDA-MB-231 cancer cells were labeled by firefly luciferase (red), while MRCS were labeled by eGFP (green). Second harmonic generation (SHG) imaging of collagen networks (cyan) was overlaid. Scale bar = 50 µm. Adapted with permission from [34].

In murine models of human breast cancer metastasis in the lungs, MRCS was able to attenuate the growth of tumors without off-target tissue damage by limiting the release of CD and subsequent apoptosis from locally converted 5-FU to stiff, crosslinked regions of ECM associated with the presence of cancer (Fig. 1.2B). Systems such as MRCS represent the beginning of a new paradigm in cancer therapy, by directly using biophysical cues of the tumor microenvironment as a biomarker. Using the distinct biophysical properties of tumors as a therapeutic target increases the specificity of cancer treatments and lowers systemic toxicity and side effects. In next-generation therapies, targeting stiffness could be an added layer in combinatorial approaches to improve the specificity of existing treatments.

1.6 Summary and Future Perspectives

Biophysical cues have emerged as critical regulators of cancer progression, as well as potential biomarkers for detection and therapeutics. It is important to interrogate not only how biophysical cues affect the cancer cells themselves but also how they affect cancer stromal cells such as cancer associated fibroblasts or immune cells like macrophages. Cell-based systems are emerging as promising tools to study cancer mechanobiology as well as for therapeutics. For instance, a cell-based stiffness sensor can reveal what cells actually "feel" in their native environment and dynamically interrogate the mechanobiology of primary tumors, metastases, and changes in biophysical properties during disease progression and response to therapies at a cellular resolution *in vivo*. Platforms such as MRCS can be modified to express diagnostic reporters like the HSV-1-tk gene coupled with positron emission tomography imaging to improve imaging and detection of micrometastases [37]. Existing immune cell therapies such as CAR-T could be further engineered to utilize the biophysical cues of tumors to improve targeting and specificity.

Further investigation into the dysregulation of tumor ECM and how changes to the ECM correlate to disease outcomes can help better focus the development of therapeutics aimed at altering the microenvironment in specific ways. Biomaterials which mimic the cancer microenvironment may provide an alternative platform to isolate and study the effects of a wide range of biophysical cues [38]. It may be possible to intervene early if premetastatic niches can be detected based on their distinct biophysical cues and treated to restore ECM homeostasis before cancer cells can engraft and successfully develop tumors. Studying whether biophysical properties of the tumor environment after successful cancer therapy differ from pre-cancer conditions could have implications for predicting recurrence. Investigating changes in biophysical properties of tumors in relation to other types of signals, such as correlating different oncogene expression with tissue stiffness, could lead to better combinatorial therapies. Finally, altered biophysical properties are also a hallmark of other disease states such as fibrosis, and the presence of fibrosis has been correlated with a higher incidence of cancer. If targeting biophysical cues can also treat fibrotic diseases, it could be an alternative way to mitigate the risk of developing cancer.

1.7 References

1. Nagelkerke, A., et al., *The mechanical microenvironment in cancer: How physics affects tumours.* Seminars in Cancer Biology, 2015. **35**: p. 62-70.
2. Fattet, L. and J. Yang, *Molecular and Cellular Mechanobiology of Cancer*, in *Molecular and Cellular Mechanobiology*, S. Chien, A.J. Engler, and P.Y. Wang, Editors. 2016, Springer New York: New York, NY. p. 277-290.
3. Maman, S. and I.P. Witz, *A history of exploring cancer in context.* Angiogenesis, 2018. **1501**: p. 1980s.
4. Cox, T.R., et al., *LOX-mediated collagen crosslinking is responsible for fibrosis-enhanced metastasis.* Cancer Res, 2013. **73**(6): p. 1721-32.
5. Cukierman, E. and D.E. Bassi, *Physico-mechanical aspects of extracellular matrix influences on tumorigenic behaviors.* Seminars in Cancer Biology, 2010. **20**(3): p. 139-145.
6. Cox, T.R. and J.T. Erler, *Remodeling and homeostasis of the extracellular matrix: implications for fibrotic diseases and cancer.* Dis Model Mech, 2011. **4**(2): p. 165-78.
7. Lu, P., V.M. Weaver, and Z. Werb, *The extracellular matrix: a dynamic niche in cancer progression.* J Cell Biol, 2012. **196**(4): p. 395-406.

8. Høye, A.M. and J.T. Erler, *Structural ECM components in the premetastatic and metastatic niche.* American Journal of Physiology-Cell Physiology, 2016. **310**(11): p. C955-C967.
9. Levental, K.R., et al., *Matrix crosslinking forces tumor progression by enhancing integrin signaling.* Cell, 2009. **139**(5): p. 891-906.
10. Hanahan, D. and R.A. Weinberg, *Hallmarks of cancer: the next generation.* Cell, 2011. **144**(5): p. 646-74.
11. Poste, G. and I.J. Fidler, *The pathogenesis of cancer metastasis.* Nature, 1980. **283**(5743): p. 139-46.
12. Ali, S.M., H.A. Harvey, and A. Lipton, *Metastatic breast cancer: overview of treatment.* Clin Orthop Relat Res, 2003(415 Suppl): p. S132-7.
13. Hedley, B.D. and A.F. Chambers, *Tumor dormancy and metastasis.* Adv Cancer Res, 2009. **102**: p. 67-101.
14. Jones, S.E., *Metastatic breast cancer: the treatment challenge.* Clin Breast Cancer, 2008. **8**(3): p. 224-33.
15. Irvin, W., Jr., H.B. Muss, and D.K. Mayer, *Symptom management in metastatic breast cancer.* Oncologist, 2011. **16**(9): p. 1203-14.
16. Singh, A. and J. Settleman, *EMT, cancer stem cells and drug resistance: an emerging axis of evil in the war on cancer.* Oncogene, 2010. **29**(34): p. 4741-51.
17. Wong, C.C., et al., *Hypoxia-inducible factor 1 is a master regulator of breast cancer metastatic niche formation.* Proc Natl Acad Sci U S A, 2011. **108**(39): p. 16369-74.
18. Erler, J.T., et al., *Lysyl oxidase is essential for hypoxia-induced metastasis.* Nature, 2006. **440**(7088): p. 1222-6.
19. Erler, J.T., et al., *Hypoxia-induced lysyl oxidase is a critical mediator of bone marrow cell recruitment to form the premetastatic niche.* Cancer Cell, 2009. **15**(1): p. 35-44.
20. Bondareva, A., et al., *The lysyl oxidase inhibitor, beta-aminopropionitrile, diminishes the metastatic colonization potential of circulating breast cancer cells.* PLoS One, 2009. **4**(5): p. e5620.
21. Wong, C.C., et al., *Inhibitors of hypoxia-inducible factor 1 block breast cancer metastatic niche formation and lung metastasis.* J Mol Med (Berl), 2012. **90**(7): p. 803-15.
22. Wickramaratne, D., et al., *Fine Needle Elastography (FNE) device for biomechanically determining local variations of tissue mechanical properties.* Journal of biomechanics, 2015. **48**(1): p. 81-88.
23. Keating, M., et al., *Spatial distributions of pericellular stiffness in natural extracellular matrices are dependent on cell-mediated proteolysis and contractility.* Acta Biomaterialia, 2017. **57**: p. 304-312.
24. Roca-Cusachs, P., V. Conte, and X. Trepat, *Quantifying forces in cell biology.* Nature Cell Biology, 2017. **19**: p. 742.
25. Kumar, A., et al., *Talin tension sensor reveals novel features of focal adhesion force transmission and mechanosensitivity.* The Journal of Cell Biology, 2016. **213**(3): p. 371-383.
26. Grashoff, C., et al., *Measuring mechanical tension across vinculin reveals regulation of focal adhesion dynamics.* Nature, 2010. **466**: p. 263.
27. Chang, C.-W. and S. Kumar, *Vinculin tension distributions of individual stress fibers within cell-matrix adhesions.* Journal of Cell Science, 2013.

28. Oldach, L. and J. Zhang, *Genetically Encoded Fluorescent Biosensors for Live-Cell Visualization of Protein Phosphorylation.* Chemistry & Biology, 2014. **21**(2): p. 186-197.
29. Cao, L., et al., *Phage-based molecular probes that discriminate force-induced structural states of fibronectin in vivo.* Proceedings of the National Academy of Sciences, 2012.
30. Jain, R.K., J.D. Martin, and T. Stylianopoulos, *The role of mechanical forces in tumor growth and therapy.* Annual review of biomedical engineering, 2014. **16**: p. 321-346.
31. Garber, K., *Stromal depletion goes on trial in pancreatic cancer*. 2010, Oxford University Press.
32. Cox, T.R. and J.T. Erler, *Fibrosis and cancer: partners in crime or opposing forces?* Trends in cancer, 2016. **2**(6): p. 279-282.
33. Sounni, N.E. and A. Noel, *Targeting the tumor microenvironment for cancer therapy.* Clinical chemistry, 2013. **59**(1): p. 85-93.
34. Liu, L., et al., *Mechanoresponsive stem cells to target cancer metastases through biophysical cues.* Science translational medicine, 2017. **9**(400): p. eaan2966.
35. Engler, A.J., et al., *Matrix Elasticity Directs Stem Cell Lineage Specification.* Cell, 2006. **126**(4): p. 677-689.
36. Dupont, S., et al., *Role of YAP/TAZ in mechanotransduction.* Nature, 2011. **474**: p. 179.
37. Brader, P., et al., *Imaging of lymph node micrometastases using an oncolytic herpes virus and [18F] FEAU PET.* PloS one, 2009. **4**(3): p. e4789.
38. Gu, L. and D.J. Mooney, *Biomaterials and emerging anticancer therapeutics: engineering the microenvironment.* Nature Reviews Cancer, 2016. **16**(1): p. 56.

CHAPTER 2:
CREATING A MECHANO-RESPONSIVE CELL SYSTEM (MRCS)

Authors: Linan Liu[1-6]† , **Shirley X. Zhang**[1-6]†, Wenbin Liao[1-6], Henry P. Farhoodi[1-6], Chi W. Wong[1-6], Claire C. Chen[1-6], Aude I. Ségaliny[1-6], Jenu V. Chacko[5], Lily P. Nguyen[1-6], Mengrou Lu[1-6], George Polovin[1-6], Egest J. Pone[1-6], Timothy L. Downing[1,5], Devon A. Lawson[1,3,7], Michelle A. Digman[5,8,9], Weian Zhao[1-6]

Affiliations:

[1]Sue and Bill Gross Stem Cell Research Center, 845 Health Sciences Road, University of California-Irvine, Irvine, California, 92697, USA.

[2]Department of Pharmaceutical Sciences, University of California-Irvine, Irvine, California, 92697, USA.

[3]Chao Family Comprehensive Cancer Center, University of California-Irvine, Irvine, California, 92697, USA.

[4]Edwards Life Sciences Center for Advanced Cardiovascular Technology, University of California-Irvine, Irvine, California, 92697, USA.

[5]Department of Biomedical Engineering, University of California-Irvine, Irvine, California, 92697, USA.

[6]Department of Biological Chemistry, University of California-Irvine, Irvine, California, 92697, USA.

[7]Department of Physiology & Biophysics, University of California-Irvine, Irvine, California, 92697, USA.

[8]Laboratory for Fluorescence Dynamics, University of California-Irvine, California 92697, USA.

[9]Centre for Bioactive Discovery in Health and Ageing, School of Science and Technology, University of New England, Armidale, New South Wales 2351, Australia.

† These authors contributed equally to this work.

2.1 Introduction

Despite decades of effort, little progress has been made to improve the treatment of the cancer metastases. Here, leveraging the central role of the mechanoenvironment in cancer metastasis, we present a mechanoresponsive cell system (MRCS) to selectively identify and treat cancer metastases by targeting the specific biophysical cues in the tumor niche *in vivo*. Our MRCS uses mechanosensitive-promoter-driven, mesenchymal stem cell (MSC)-based vectors, which selectively home to and target cancer metastases in response to specific mechanical cues such as matrix stiffness. We will first engineer the MRCS, and verify the activation and functionality *in vitro*.

2.2 Mesenchymal Stem Cells

We hypothesized that a cell-based system, specifically, mesenchymal stem cells (MSCs) can be used for such an approach to generate a mechano-responsive cell system (MRCS) that responds specifically to mechanoenvironmental cues to target breast cancer metastases (fig. 2.S1). MSCs are multipotent cells that can be derived from multiple adult tissues, including bone marrow and fat [1, 2]. MSCs are the basis for the first approved stem cell treatment in humans outside of bone marrow transplant (Prochymal, Osiris Therapeutics) and for over 400 ongoing trials listed on clinicaltrials.gov with widely demonstrated safety [3, 4]. Systemically infused MSCs preferentially home to and integrate with tumors in vivo, including both primary breast tumors and lung metastases [5, 6]. Mounting evidence now suggests that MSCs possess leukocyte-like, active homing mechanisms for tumor tropism involving a variety of adhesion molecules and tumor-derived cytokines, chemokines, and growth factors [7]. This selective and active homing ability makes MSCs an appealing vector for localized delivery of therapeutics in cancer treatment [5, 6].

Tissue mechanical properties regulate MSC fate: tissue and matrix stiffness is sufficient to drive expression of genes involved in MSC differentiation [8-10]. Specifically, soft matrices, similar to the brain (Young's modulus of less than 1 kPa), direct MSCs into a neurogenic lineage, whereas stiffer matrices (5 to 75 kPa), similar to muscle and bone, direct them into myogenic and osteogenic lineages, through integrin and focal adhesion-dependent mechanisms [8]. The range of stiffness to which MSCs respond encompasses those found in normal breast and lung tissues (less than 1 kPa), as well as invasive cancers and metastases (10-15 fold higher stiffness) [11]. MSC differentiation is inherently a transcriptional program, which allows us to use promoters regulating genes involved in MSC mechanotransduction/differentiation cascades to drive expression of downstream reporters or therapeutics [8].

2.3 Transcriptional Regulators

The transcriptional factor YAP(Yes-associated protein)/TAZ(transcriptional co-activator with PDZ-binding motif) preferentially translocates to the nucleus to trigger downstream gene expression in a stiffness-dependent manner. In particular, Yes-associated protein (YAP) / transcriptional coactivator with PDZ-binding motif (TAZ) have previously been reported as sensors and mediators of mechanical cues via, for instance, the cytoskeleton and Rho GTPase [12, 13]. On soft substrates in vitro (< 1 kPa), YAP remains inactivated in the cytoplasm, but on stiff substrates in vitro (> 10 kPa), YAP localizes to the nucleus and becomes activated as a transcriptional factor [12-14]. YAP/TAZ have greater nuclear accumulation in samples from breast cancer patients associated with enhanced desmoplasia [15]. YAP/TAZ have also been reported to be key upstream factors that regulate lineage-specific transcription factors (including *RUNX2*, an osteogenic marker) and drive MSC differentiation, including osteogenesis [16]. By engineering cells to repurpose known mechano-sensitive transcriptional regulators such as YAP/TAZ, we can selectively drive downstream expression of fluorescent reporters or therapeutic proteins by using the biophysical cues of the cell microenvironment.

2.4 Engineering MRCS

To create a MRCS, we take advantage of the endogenous ability of MSCs to respond to matrix stiffness to drive expression of reporters or therapeutics with stiffness-responsive promoters. In light of the tight correlation between tissue stiffness, breast cancer metastasis, and mechanotransduction-mediated MSC differentiation, we have developed a MRCS to directly target the mechanoenvironmental cues of breast cancer metastases for specific delivery of an anti-tumor agent, cytosine deaminase (CD), which locally activates prodrug 5-fluorocytosine (5-FC) to kill cancer (fig. 2.S1). Our study demonstrates that the MRCS, which is engineered to be inducible by biophysical and mechanical cues, specifically responds to matrix stiffness in vitro and can selectively target and kill cancer.

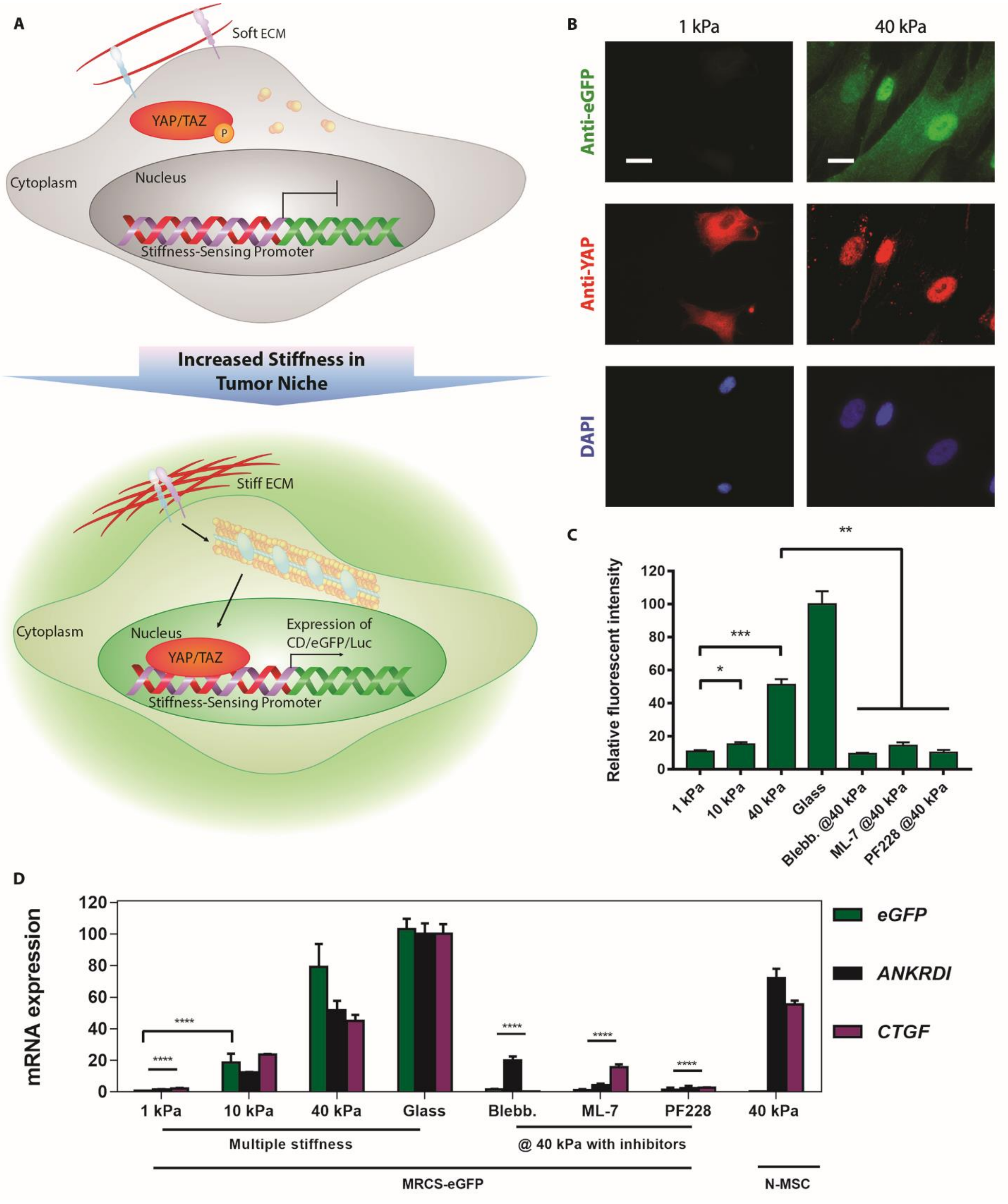

Fig. 2.1. MRCS in vitro validation

(**A**) The schematic of a proposed mechanism of how MRCS works. When the stiffness of extracellular matrix (ECM) increases, YAP/TAZ are activated and localize to the nucleus. Then YAP/TAZ will bind to the synthetic stiffness-sensing promoter in MRCS and drive the expression of downstream reporters such as eGFP and Luc) and/or therapeutics. Note: This schematic is simplified to clarify the major components in MRCS mechanism. (**B**) Representative images of MRCS-eGFP plated on soft (~ 1 kPa) and firm (~ 40 kPa) polyacrylamide gels. eGFP (stained with anti-eGFP, green) was turned on in response to higher stiffness. YAP (stained with anti-YAP, red) localization is also regulated by stiffness, such that it concentrates in nuclei on stiffer substrates. DAPI (blue, nuclear counterstain) is displayed. Scale bar = 25 μm. (**C**) Quantification of fluorescent intensity of eGFP (stained with antibody) from MRCS-eGFP seeded on substrates with different stiffness or on firm (~ 40 kPa) substrates treated with 10 μM ML-7 (myosin light-chain kinase inhibitor) or 20 μM PF228 (focal adhesion kinase inhibitor). (**D**) Quantitative reverse-transcriptase-PCR (RT qPCR) analysis of MRCS-eGFP on hydrogels. Expression of *eGFP* (green) and YAP/TAZ downstream factors (*CTGF*, purple, and *ANKRDI*, black) was increased on stiff substrate and was downregulated on soft substrate or with mechanosensing inhibitors, showing that MRCS is stiffness-specific. Quadruplicate samples were used for the analysis. Data shown as mean ± SD. $^{*}P < 0.05$, $^{**}P < 0.01$, and $^{***}P < 0.001$. Data shown as mean ± SEM.

We have established a MRCS using a YAP/TAZ stiffness-sensing promoter. When activated, YAP/TAZ can drive the expression of downstream reporters such as enhanced green fluorescent protein (eGFP) (MRCS-eGFP) for in vitro imaging, firefly luciferase (MRCS-Luc) for later *in vivo* imaging, or anti-tumor agents (MRCS-CD) as cancer treatment (Fig. 2.1A and fig. 2.S2). In effect, YAP/TAZ serves as an on/off switch for the MRCS gene expression triggered by the substrate stiffness in our study. For this text, cells that constitutively express a gene, such as CD-MSC or Luc-MSC, will have the gene being expressed first in the nomenclature. For MRCS cells such as MRCS-CD or MRCS-eGFP, MRCS will come first in the name to indicate that it is the engineered stiffness-sensing promoter system that is driving the expression of the downstream gene.

To validate the selective activation of our MRCS in response to stiffness, MRCS-eGFP were seeded on tunable polyacrylamide hydrogels with various stiffness (~ 1 kPa, ~ 10 kPa, and ~ 40 kPa) [8, 12]. As expected, on soft hydrogel (~ 1 kPa), YAP remained in the cytoplasm, and no eGFP signal could be detected (Fig. 2.1B and fig. 2.S3A), whereas on stiffer hydrogels (> 10 kPa), YAP localized to the nuclei and eGFP was expressed, typically within 24-48 hours after cell seeding (Fig. 2.1B, fig. 2.S3, B and C). As a control, MRCS-eGFP plated on glass (the highest stiffness used) showed strong activation of YAP/TAZ and eGFP expression (fig. 2.S3D). MRCS-eGFP treated with blebbistatin, an inhibitor of mechanotransduction which impedes signaling downstream of matrix stiffness and integrin activation [8, 12], showed no eGFP expression, and YAP remained in the cytoplasm, even on stiff substrates (fig. 2.S3E). Two other mechanotransduction inhibitors, PF228 and ML-7, a focal adhesion kinase (FAK) inhibitor and a myosin light-chain kinase (MLCK) inhibitor, respectively, similarly deactivated YAP and downstream eGFP expression (fig. 2.S3, F and G).

A more comprehensive view of the cells in Fig. 2.1B can be found in fig. 2.S4. Quantification of the stiffness-mediated eGFP expression of MRCS confirms that the intensity of reporter expression correlates positively with the substrate stiffness, such that stiffer hydrogel resulted in stronger eGFP signal, with attenuated expression in the presence of mechanotransduction inhibitors (Fig. 2.1C). This set of data demonstrates that YAP activation in response to altered stiffness is MLCK/FAK-dependent. We used quantitative reverse-transcriptase PCR (RT qPCR) to further characterize the expression of *eGFP* mRNA and two additional genes (*CTGF* and *ANKRDI*) that are transcriptionally regulated by YAP/TAZ. Consistent with the imaging data, expression of *eGFP*, *CTGF,* and *ANKRDI* was specifically activated on stiffer hydrogels (Fig. 2.1D). It is interesting to note the differences in expression of *eGFP* vs. the other YAP-induced markers, which are likely due to different sensitivities of YAP binding to exogenous and endogenous promoters, since we are using a synthetic promoter for *eGFP*. We similarly prepared and characterized MRCS engineered to produce firefly luciferase (MRCS-Luc) (fig. 2.S5). Collectively, these data indicate that our MRCS is stiffness-specific and can respond to a range of matrix stiffness to drive downstream gene expression.

2.5 MRCS validation *in vitro*

To use MRCS to locally treat breast cancer metastasis in the lung, we engineered the cells to express CD instead of a reporter gene (fig. 2.S2). CD is a prodrug convertase that converts the inactive prodrug 5-fluorocytosine (5-FC) to the active drug 5-fluorouracil (5-FU) [17]. This leads to localized tumor killing via the bystander effect in which the apoptotic MRCS locally releases CD [18] (fig. 2.S1). This promising technique is currently being used in clinical trials, for example with 5-FU delivery by neural stem cells (NSCs) for treatment of glioblastoma [18]. To validate the effectiveness of this prodrug system, we first confirmed that MSCs engineered to constitutively express CD (abbreviated as CD-MSC) are able to sufficiently convert 5-FC to kill MDA-MB-231 breast cancer cells in vitro (fig. 2.S6). We next constructed MRCS-CD with the YAP/TAZ promoter to drive the expression of CD in response to matrix stiffness. To validate the stiffness-specific regulation of CD expression and conversion of 5-FC, MRCS-CD were seeded on polyacrylamide hydrogels with different stiffness. On soft hydrogel (~ 1 kPa), a minimal amount of CD was expressed (fig. 2.S7A), but on stiffer hydrogels and glass (> 10 kPa), CD expression was turned on (fig. 2.S7, B to D). This expression pattern also correlated well with the localization of YAP. In the presence of mechanotransduction inhibitors, CD expression was turned off even on stiff hydrogel (~ 40 kPa) (fig. 2.S7, E to G). Quantification of stiffness-dependent CD expression was also performed and showed increased CD expressed from MRCS on stiffer substrates (Fig. 2.2A). Additionally, we calculated the proportion of MRCS activated by substrates of varied stiffness from fluorescent signals. On soft substrate (~ 1 kPa), only approximately 2% of MRCS was activated, compared to 13% on ~ 10 kPa, 56% on ~ 40 kPa substrate, and 100% on glass.

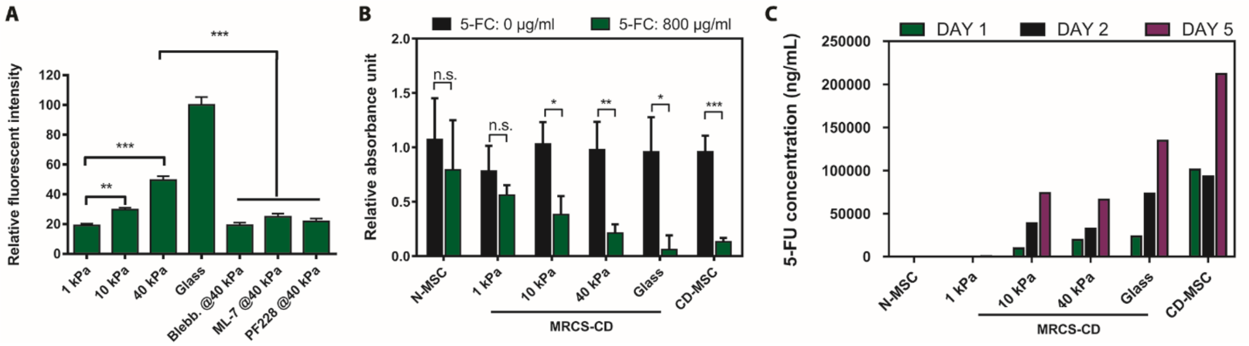

Fig. 2.2. MRCS-CD activation dependent on substrate stiffness in vitro

(**A**) Quantification of fluorescent signals of CD shows MRCS-CD responding to matrix stiffness in vitro*.* MRCS-CD were stained with antibody after plating on tunable polyacrylamide gels or glass as indicated, or treated with 50 μM blebbistatin, 10 μM ML-7 (myosin light-chain kinase inhibitors), or 20 μM PF228 (focal adhesion kinase inhibitor). The fluorescent signal of CD was analyzed, and the relative fluorescent intensity is shown. Data shown as mean ± SEM. Triplicate samples were used for the analysis. (**B**) MRCS-CD kill cancer cells in response to matrix stiffness and 5-FC in vitro*.* MRCS-CD were co-cultured with MDA-MB-231 breast cancer cells (231: MRCS = 2:1) with (800 μg/ml, green) or without (black) 5-FC on substrates with different stiffness. Total cell proliferation (XTT assay) is displayed. The data were normalized to breast cancer only (231: MRCS = 1:0) with or without 5-FC on each stiffness. Triplicate samples were used for the analysis. Data shown as mean ± SD., n.s., not significant, $^{*}P < 0.05$, $^{**}P < 0.01$, $^{***}P < 0.001$, and $^{****}P < 0.0001$. (**C**) Conversion of 5-FC to 5-FU by MRCS-CD in response to matrix stiffness in vitro*.* MRCS-CD were seeded on substrates with different stiffness, with 800 μg/ml 5-FC in growth medium for 1, 2, or 5 days. The concentration of 5-FU in the conditioned medium was detected by LC-MS/MS.

To test whether MRCS-CD could kill cancer specifically on high-stiffness substrates, MRCS-CD were co-cultured with MDA-MB-231 breast cancer cells on polyacrylamide hydrogels with or without 5-FC, and XTT assay was performed to quantify total cell proliferation (Fig. 2.2B). On soft hydrogel (~ 1 kPa), there was no significant difference in cancer cell proliferation with or without the addition of 5-FC, consistent with the low expression of CD under these soft matrix conditions. When seeded on hydrogels with increased stiffness (~ 10 and ~ 40 kPa) or on glass, cell proliferation was significantly decreased in the presence of 5-FC in proportion to stiffness ($P < 0.05$), suggesting that CD was expressed and converted the prodrug to its active form to kill the cancer cells. CD-MSC without a stiffness-sensing promoter showed significantly reduced cell proliferation in the presence of 5-FC due to constitutive expression of CD ($P < 0.001$), whereas native MSCs (N-MSC) showed no difference in total cell proliferation, as expected because they do not produce CD. These data demonstrate that MRCS-CD can selectively activate CD expression in response to matrix stiffness and convert 5-FC to kill adjacent cancer cells in vitro. To quantify the conversion of 5-FC to 5-FU, MRCS-CD were seeded on substrates with different stiffness with 5-FC in the growth medium for 1, 2, or 5 days, at which point the amount of 5-FU in the growth medium was detected by LC-MS/MS [17] (Fig. 2.2C). The data show that the conversion to 5-FU is stiffness-dependent, with no detectable conversion on soft substrate (~ 1 kPa) and increased conversion with increased stiffness (~ 10 and ~ 40 kPa). This also demonstrates that MRCS-CD can continue to express CD and convert 5-FC to 5-FU over a period of at least several days in vitro.

To further characterize the timing of cancer killing, MRCS-CD were co-cultured with MDA-MB-231 using transwell in the presence of 5-FC (fig. 2.S8). XTT assay was performed to quantify cell proliferation for both cell types. The decrease in Luc-RFP-231 proliferation indicates that MRCS-CD began to kill cancer cells (or attenuate cancer growth) within 2 days, with the MRCS-CD themselves dying after. The bystander effect of MRCS-CD also lasted after they were removed from the cancer cells, with a significant decrease in cancer proliferation measured on Day 9 ($P < 0.01$) even when the MRCS-CD were removed as early as Day 2 (fig. 2.S9). This suggests that, even if MRCS only transiently interacts with tumor microenvironments and gets cleared after two days, cancer growth can be attenuated over a longer period of time.

2.6 Discussion

Our data show that MRCS was successfully engineered to trigger gene expression downstream of the YAP/TAZ promoter selectively on stiffer substrates. It is important to note that this activation does not adhere to a strict stiffness threshold but rather gene expression increases proportionally with increasing substrate stiffness. This expression was attenuated in the presence of mechanotransduction inhibitors such as blebbistatin, but further studies on this could be performed using tunable hydrogel platforms to test the true dynamics and reversibility of MRCS. This stiffness-specific activation translates to prodrug conversion and efficacy in cancer killing, with MRCS as effective therapeutically as CD-MSC on stiff substrates.

We have also directly quantified this by measuring the conversion of 5-FC to 5-FU using LC/MS-MS. Our data show that MRCS can continue to functionally convert 5-FC to 5-FU for at least 5 days while in contact with stiff substrate, though the process of cancer killing could begin as early as 2 days after treatment, with the MRCS-CD themselves dying shortly after. Interestingly, cancer cell proliferation remains significantly decreased (up to day 9 in our *in vitro* study) even when MRCS-CD were removed on day 2. This suggests that, even if MRCS only transiently interact with tumor microenvironment and get cleared after two days *in vivo*, cancer growth can be attenuated over a longer period of time. In therapeutic settings *in vivo*, where cell transplants may be cleared out in this timeframe by the immune system, this suggests that MRCS can be a transient yet efficient drug delivery system for treating cancer with lasting benefits.

However, while *in vitro* data suggests that MRCS would be effective at killing cancer in stiff environments, there are many factors *in vivo* to account for in future studies. The true 3D environment of an *in vivo* tumor model will present variables we did not test for *in vitro*, such as homing, immune response, off-target activation and cancer tissue stiffness.

2.7 Materials and Methods

Cell lines and cell culture

Human bone marrow MSCs were obtained from the Texas A&M Health Science Center and were expanded to passages 3-6 for further use. The cells were routinely maintained in Minimum Essential Medium α (MEM α, Life Technologies) supplemented with 15% fetal bovine serum (FBS, Atlanta Biologicals) and 1% penicillin-streptomycin (PenStrep, 100 U/ml, Life Technologies) at 37°C in a humidified incubator containing 5% CO_2. The human breast cancer cell line MDA-MB-231 was obtained from American Type Culture Collection (ATCC). These cells were grown in Leibovitz's L-15 medium containing L-glutamine (Corning), and supplemented with 10% FBS and 1 U/ml PenStrep at 37°C in a humidified incubator without CO_2. The 293T-LV cell line (Gen Target) was cultured in Dulbecco's

Modified Eagle Medium (DMEM, Life Technologies) supplemented with 10% FBS, non-essential amino acids (NEAA, 1X, 100 U/ml, Life Technologies) and 1 U/ml PenStrep at 37°C in a humidified incubator containing 5% CO_2.

Generation of lentiviral vectors and lentiviral transduction

The following lentiviral vectors were used in this study: LV-*CMV*::eGFP, LV-*CMV*::Luc-RFP, LV-*CMV*::CD, LV-MRCS-eGFP, LV-MRCS-Luc, and LV-MRCS-CD. The sequences of interest from pUCBB-eGFP (a gift from Claudia Schmidt-Dannert [19], Addgene #32548), pcDNA3.1(+)/Luc2=tdT (a gift from Christopher Contag [20], Addgene #32904), pSelect-zeo-*Fcy*::*Fur* (InvivoGen) and 8xGTIIC-luciferase (a gift from Stefano Piccolo [12], Addgene #34615) were cloned into the promoterless lentiviral transfer vector LV-PL4 (GenTarget). All MSCs and breast cancer cells were transduced as previously described [21]. Briefly, all lentiviral constructs were packaged (gifts from Didier Trono, pMD2.G, Addgene #12259; pRSV-Rev, Addgene #12253; pMDLg/pRRE, Addgene #12251) as lentiviral (LV) vectors in 293T-LV cells using Lipofectamine LTX and PLUS Reagents (Life Technologies) [21]. Cells were transduced with LVs by incubating virions in a culture medium containing 100 µg/ml protamine sulfate (Sigma). Cells transduced with LVs containing empty vectors (EV) were used as a control. After selection with medium containing 10 µg/ml puromycin (MP Biomedicals), fluorescent protein-expressing cells were visualized for protein expression using fluorescence microscopy (Eclipse Ti, Nikon).

Hydrogel synthesis and immunocytochemistry (in vitro)

Polyacrylamide tunable hydrogels coated with collagen were synthesized as previously described [22]. The stiffness of hydrogels was attuned by adjusting the ratio of acrylamide and bis-acrylamide [22]. Cells were seeded in droplets to evenly spread onto the hydrogels and harvested for further assays 24-48 hours later, according to previous literature [12]. To test if the MRCS was stiffness-dependent, in some experiments, 50 μM (−) blebbistatin (Sigma), 10 μM ML-7 (Sigma), or 20 μM PF 573228 (PF228, Sigma) were added to the MRCS after attachment. Cells were briefly fixed in 4% paraformaldehyde (PFA, Amresco) and permeabilized in 0.1% IGEPAL CA-630 (Sigma). Primary antibodies (mouse anti-YAP 1: 100; sheep anti-CD 1: 200; chicken anti-eGFP 1: 500) were incubated overnight in phosphate buffered saline (PBS, Lonza) with 0.1% Triton X-100 (Sigma) and 2% goat (Thermo Fisher Scientific) or donkey serum (Sigma) for double-staining. Secondary antibodies were diluted 1: 500 and were applied for 30 minutes at room temperature. Slides were washed in PBS and mounted with Fluoromount-G (Southern Biotech). DAPI (50 μg/ml, Life Technologies) in PBS was added onto samples before mounting. All the antibodies used in this experiment are listed in Table 1 (primary antibodies) and Table 2 (secondary antibodies). Protein expression was quantified by normalizing the average of fluorescence intensity within the cells to the glass control using the NIS-Elements AR software (Nikon) after background subtraction. Triplicate samples were used for the analysis.

For calculating the ratio of MRCS which was activated with the stiffness-sensing promoter, a threshold was set using mean + 2 x SD of fluorescent signals of MRCS seeded on ∼ 1 kPa hydrogels. The same threshold was applied to all cells seeded on hydrogels with different stiffness, and all cells with fluorescent signal higher than this threshold were defined as activated.

Quantitative reverse transcriptase PCR (RT qPCR)

Hydrogels were synthesized and cells were seeded as above. To test the expression of mRNAs regulated by mechano-cues in vitro, cells were harvested from hydrogels, glass coverslips, or tissue culture plates in TRIzol (Invitrogen) for total RNA extraction with DNase I (Thermo Fisher Scientific) treatment to remove DNA contamination according to the manufacturer's protocol. cDNA synthesis was performed with Oligo(dT) (Invitrogen) primed SuperScript III RNase H Reverse Transcriptase (Invitrogen) and Power SYBR Master Mix (Life Technologies). RT qPCR was performed in quadruplicates on an Applied Biosystems ViiA 7 Real-Time PCR System, and data were analyzed with ViiA^{M} 7 Software v1.2. Relative gene expression was normalized to the endogenous gene *GAPDH.* Sequences of primers [12, 23, 24] used in this study [Integrated DNA Technologies (IDT)] are provided in Table 3.

In vitro bioluminescence assays and XTT cell viability assays

LV-*CMV*::Luc MSCs (Luc-MSC) expressing firefly luciferase (Luc) and LV-MRCS-Luc MSCs (MRCS-Luc) were seeded onto collagen-coated hydrogels with different stiffness as described [12]. After the cells were washed with PBS, D-luciferin (150 μg/ml in PBS, Perkin Elmer) was added, and the activity of Luc was then measured. MSCs [LV-MRCS-CD MSCs (MRCS-CD), LV-*CMV*::CD MSCs (CD-MSC) or native MSCs (N-MSC)] were seeded onto hydrogels with MDA-MB-231 breast cancer cells with a ratio of 2: 1 (231: MSCs). Prodrug 5-fluorocytosine (5-FC, 800 μg/ml in MSC growth medium, Sigma) was added after attachment.

Reagents from XTT kit (2,3-Bis-(2-Methoxy-4-Nitro-5-Sulfophenyl)-2*H*-Tetrazolium-5 Carboxanilide, ATCC) were mixed and added to cells after 5 days of co-culture. The color absorbance was measured after 2 hours of incubation at 37°C in a humidified incubator. Bioluminescent signals and color absorbance were measured with a plate reader (BioTek). All samples above were measured at least in triplicate.

Sample preparation and ultra high performance liquid chromatography-electrospray ionization tandem quadrupole mass spectrometry (UPLC-MS/MS)

MSCs (MRCS-CD, CD-MSC, or N-MSC) were seeded at a density of $10^4/cm^2$ on the hydrogels with varying stiffness or cover slides. Cells were allowed to grow for 24 hours in MSC growth medium and were then treated with 800 µg/ml 5-FC (Day 0). On Days 1, 2, and 5, conditioned medium was collected for extraction. 200 µl of the conditioned medium from each condition was extracted using 1000 µl of ethyl acetate: isopropanol = 1: 1 (v:v) (Sigma). For in vivo experiments, whole lungs were collected from NSG mice 1 day after treatment with 5-FC (500 mg/kg in DPBS). The tissue was homogenized using Bel-Art Micro-Tube Homogenizer (Bel-Art) and extracted using 500 µl of ethyl acetate: isopropanol: acetic acid = 84: 15: 1 (v:v:v) (Sigma). Organic phase was collected after centrifugation at 3,000 *g* for 10 minutes. Additional protein precipitation was done by adding 80 µl of saturated ammonium sulfate solution. After centrifuging at 3,000 *g* for 10 minutes, the organic layer was transferred into a new microcentrifuge tube and dried using a centrifugal vacuum concentrator (Speedvac, Thermo Fisher Scientific). The extracted compounds were reconstituted in 250 µl water containing 20% acetonitrile, and 100 µl was used for the UPLC-MS/MS.

Culture medium spiked with 400 µg/ml 5-FC and 5-FU was used to determine the extraction yield. A 6-point 5-FU standard curve (⅓ dilution starting from 10 µg/ml) with a $R^2 > 0.98$ was used to quantify the 5-FU in the samples. 5-FU standard solutions were prepared in water with 20% acetonitrile. 10 µl was injected into the UPLC system for analysis, and then eluted on an Acquity UPLC BEH C18 1.7 µm column (Waters). UPLC was performed using the Acquity UPLC system (Waters) with a mobile phase gradient starting with 98% of a mobile phase composed of 98% water, 2% acetonitrile, and 0.2% acetic acid, which progressively went up to 95% of the second mobile phase (100% acetonitrile and 0.2% acetic acid) for the elution of the samples. Then, the samples were injected into the triple quad mass spectrometer (Waters Micromass Quattro Premier XE Tandem Quadrupole Mass Spectrometer, Waters) for the mass analysis. The electrospray ionization was performed using the negative ion mode, which generates a precursor to product ion transition of m/z 129 > 42 for the 5-FU. After training, the cone voltage (CV) and the collision cell energy (CE) were optimized at 20V and 30V, respectively. Dwelling time was 0.285 seconds, and total run time per sample was 3 minutes. MassLynx software was used for data acquisition, and QuantLynx software for the data analysis and quantification.

Transwell co-culture assays

MSCs (MRCS-CD or N-MSC) were plated on type I collagen (BD Biosciences)-coated 6.5 mm transwell culture inserts with pore size of 0.45 µm (Corning Life Sciences), while Luc-RFP-231 cancer cells were plated on the lower chamber. After cell seeding, both of them were allowed to grow for 24 hours in MSC growth medium separately before the transwell got assembled. Then the MSCs and cancer cells started to be co-cultured with 800 µg/ml of 5-FC in MSC growth medium (Day 0). On Days 0, 1, 2, 5, 7, and 9, XTT assays were performed to measure the cell viability. Procedures were similar to the above XTT section, except XTT reagents were collected after the incubation of the reagents, and redistributed to a new 96-well plate for measurement. XTT reagent was washed off with sterile PBS and MSC growth medium after each measurement. Cells were then re-incubated in growth medium until the next time point of measurement. All values were normalized to that of cancer cells alone without co-culture at each time point. In an independent experiment, inserts with MSCs were removed on Days 1, 2, 7, and 9, and an in vitro proliferation luciferase assay was performed on Day 9 to quantify the living Luc-RFP-231 cells. All values were normalized to that of cancer cells co-cultured with N-MSC.

Study Design

This study was designed to investigate the hypothesis that a cell-based system can be engineered to respond specifically to mechanoenvironmental cues (MRCS) to target cancer metastases. In vitro experiments including tunable hydrogels, qPCR, co-cultures, and mass spectrometry, and in vivo and ex vivo experiments using nude and NSG mice, including luciferase imaging, antibody staining, SHG, and AFM, were performed to demonstrate that MRCS can sense and kill cancer cells in response to biophysical cues. For all in vitro studies except for mass spectrometry, three independent experiments with at least three samples per condition were performed. $n = 9$ for the in vivo cancer killing and survival assays. $n \geq 3$ for ex vivo characterization of the biophysical cues in the metastatic niche and the validation of MRCS. For the survival experiment, the endpoint for mice was defined as “found dead” or euthanasia criteria stated in UCI IACUC protocol 2012-3062 described in Supplementary

Materials and Methods. Groups for animal experiments were randomized, except for the cancer killing study where manual group adjustments were performed to keep the differences in initial cancer burden between all “week 0” group animals not statistically significant. In vitro experiments were not blinded. In vivo and ex vivo experiments were blinded.

Statistical analysis

Data were analyzed by Student's *t* test when comparing 2 groups and by ANOVA when comparing more than 2 groups. Log-rank (Mantel-Cox) test was performed for animal survival data analysis by two-way ANOVA and Mann Whitney test was used for AFM data. Outliers in AFM data were removed by Grubb’s test ($P < 0.05$). Data were expressed as mean ± SD or mean ± SEM. Two-sided testing with normal-based 95% confidence interval was performed for each analysis, and differences were considered significant at $P < 0.05$.

2.8 Supplemental Figures and Tables

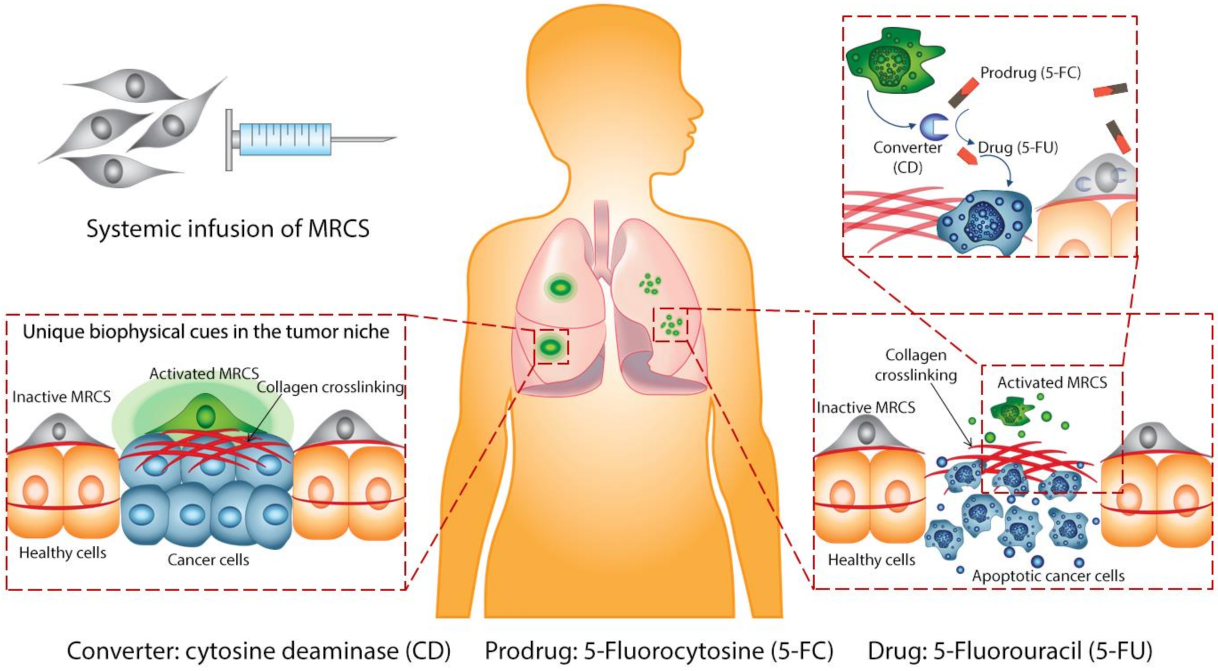

Fig. 2.S1. The concept of mechano-responsive cell system (MRCS) for targeting breast cancer metastases in the lung

The tumor-homing MRCS are locally activated by specific ranges of stiffness linked to collagen crosslinking found at the metastatic niche (red crosshatching), thereby expressing or secreting reporters and therapeutics (left side) and selectively treating cancer metastases using converter enzyme CD and prodrug 5-FC (right side).

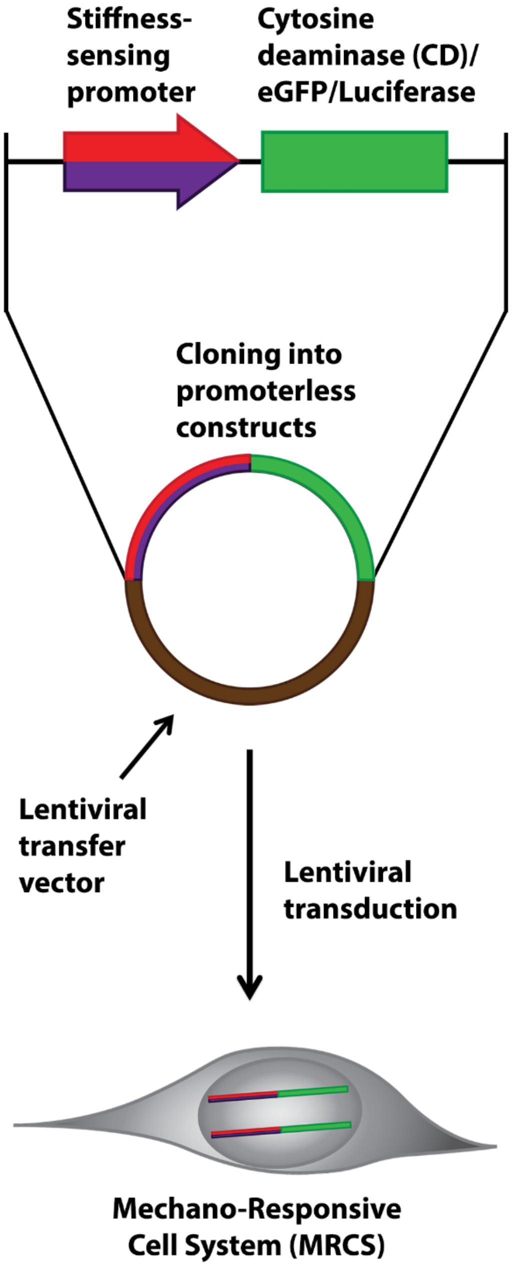

Fig. 2.S2. **Construction of MRCS**

The scheme of cell engineering. Promoters of genes responsive to specific ranges of stiffness are cloned into promoterless vectors to drive expression of eGFP, luciferase, and/or CD. Then the constructs are transduced into mesenchymal stem cells (MSCs) to produce stable engineered MSCs (MRCS).

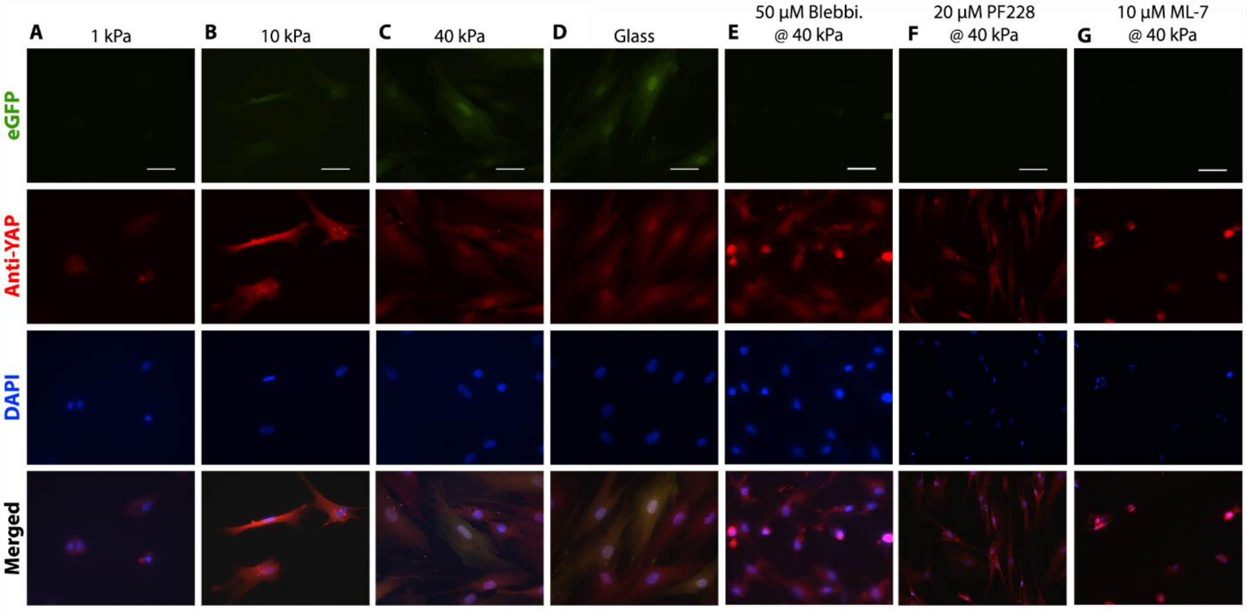

Fig. 2.S3. MRCS-eGFP activation in response to substrate stiffness in vitro

MRCS-eGFP were plated on (**A**) soft (~ 1 kPa), (**B**) medium (~ 10 kPa), or (**C**) firm (~ 40 kPa) polyacrylamide gel or (**D**) glass. eGFP (green, no staining) was turned on in response to higher stiffness (≥ 10 kPa). YAP (red, stained with anti-YAP) relocalization is also regulated by stiffness, and concentrated in nuclei on stiffer substrates (≥ 10 kPa). When MRCS-eGFP on firm (~ 40 kPa) substrates were treated with (**E**) 50 µM blebbistatin, (**F**) 10 µM ML-7, or (**G**) 20 µM PF228, eGFP (green, no staining) was turned off and YAP (red, stained with anti-YAP) was localized in the cytoplasm. DAPI (blue, nuclear counterstain) is also displayed. Scale bar = 100 µm.

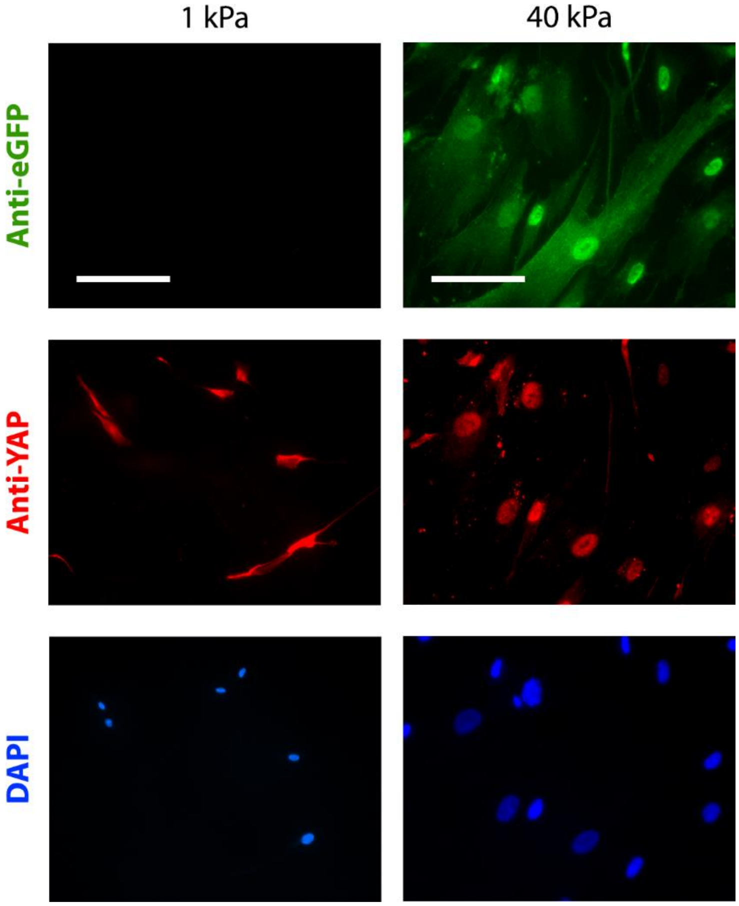

Fig. 2.S4. MRCS-eGFP in vitro validation with immunostaining

Representative images of MRCS-eGFP plated on soft (~ 1 kPa) and firm (~ 40 kPa) polyacrylamide gels. eGFP (green, stained with anti-eGFP) was turned on responding to higher stiffness. YAP (red, stained with anti-YAP) was concentrated in nuclei on stiffer substrates. DAPI (blue, nuclear counterstain) is displayed. Scale bar = 100 µm.

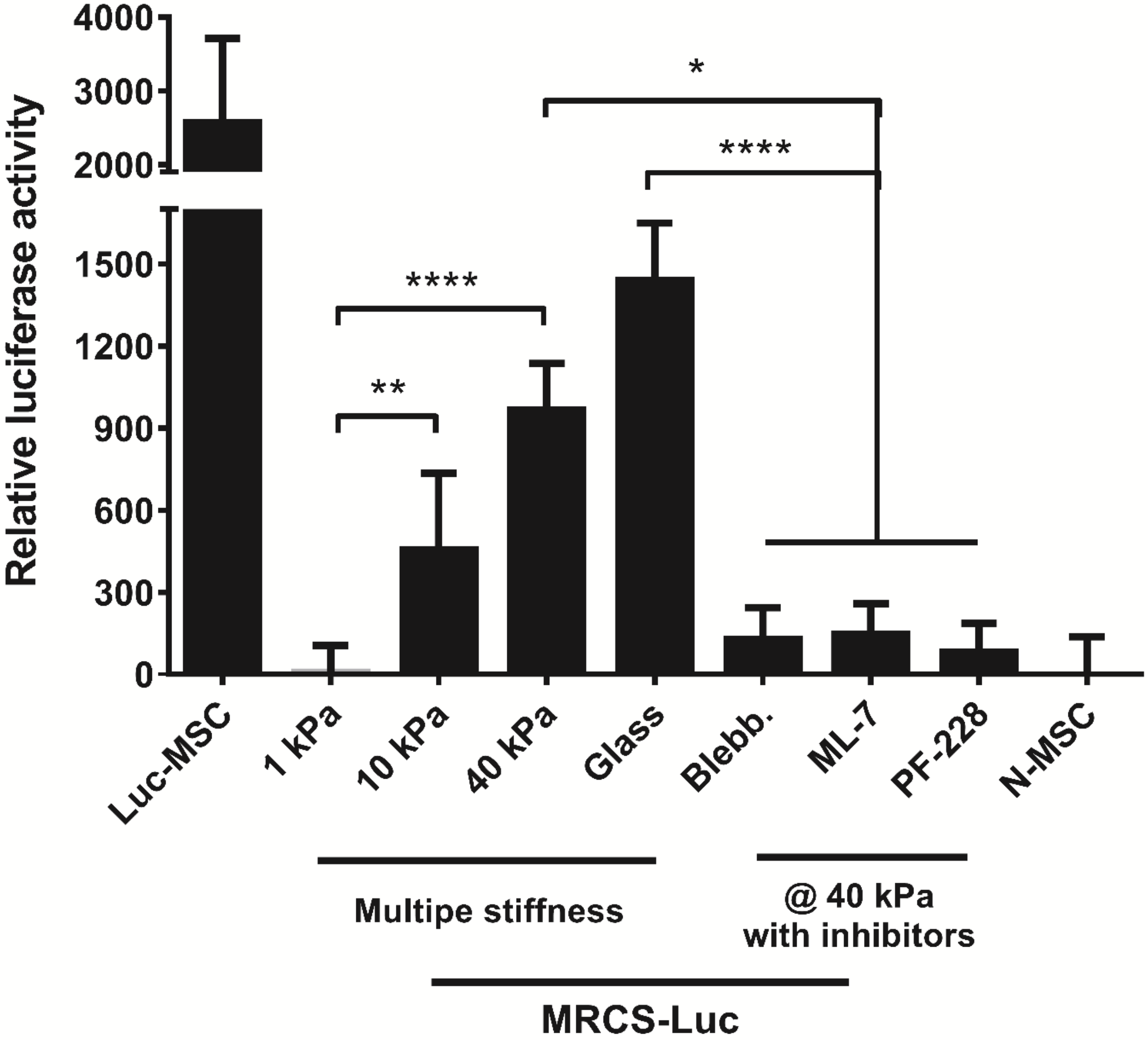

Fig. 2.S5. Further MRCS-Luc in vitro validation

MRCS-Luc were seeded on substrates with different stiffness or on firm (~ 40 kPa) substrates treated with inhibitors as above in fig. 2.S3. Luciferase activity was upregulated on stiff substrate and downregulated on soft substrate or with mechanosensing inhibitors. *$P < 0.05$, **$P < 0.01$, and ****$P < 0.0001$. Triplicate samples were used for the analysis. Data shown as mean ± SD.

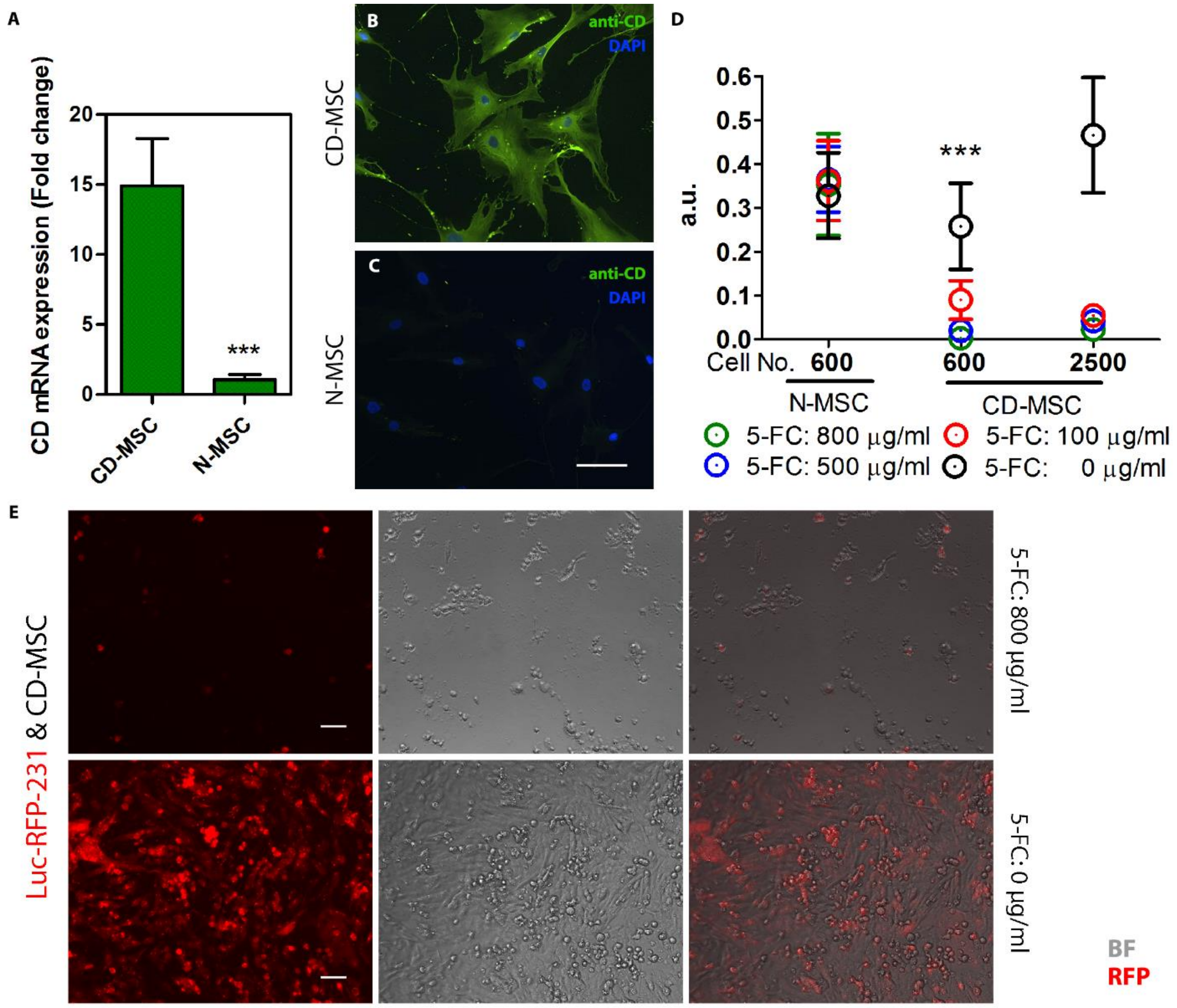

Fig. 2.S6. CD-MSC able to kill cancer cells in the presence of 5-FC in vitro

The expression of CD was validated by (**A**) RT qPCR and (**B**) immunofluorescent staining. CD (green); DAPI (blue, nuclear counterstain). N-MSC were included as control in (**A**) and (**C**). In (**A**), CD mRNA expression of N-MSC was normalized to 1. N-MSC do not express CD. (**D**) XTT assay was performed to show that CD-expressing MSCs are suicide agents in the presence of 5-FC at various concentrations. MSC proliferation was highly decreased only with both CD-expressing MSCs and prodrug 5-FC. (**E**) Co-culture experiment was conducted with CD-MSC and RFP-expressing MDA-MB-231 breast cancer cells (231: MSC=2:1) with or without 800 µg/ml 5-FC.

About 95% of breast cancer cells were killed and rest were undergoing apoptosis, whereas control without 5-FC had a high confluency. RFP (red) and bright field (BF) images are displayed. Triplicate samples were used for the analysis. Scale bar = 100 μm. Data shown as mean ± SD. ****P* < 0.001.

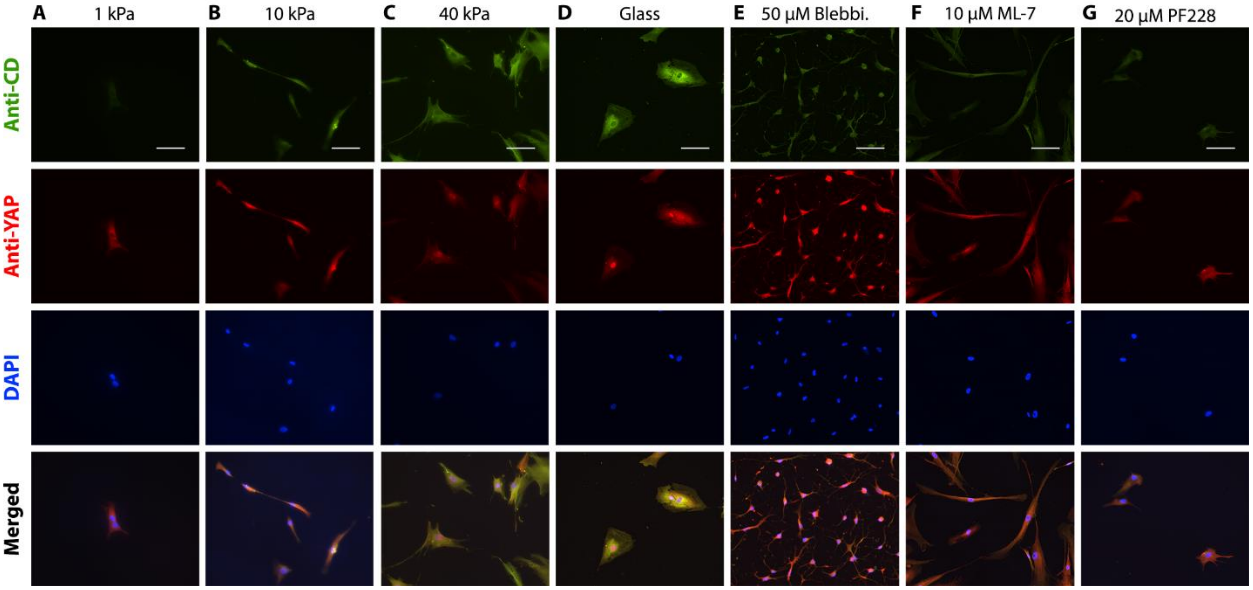

Fig. 2.S7. MRCS-CD responding to matrix stiffness in vitro

MRCS-CD were plated on (**A**) soft (~ 1 kPa), (**B**) medium (~ 10 kPa), or (**C**) firm (~ 40 kPa) polyacrylamide gel or (**D**) glass. CD (green) was turned on responding to high stiffness (≥ 10 kPa). YAP (red) relocalization was also regulated by stiffness. When MRCS-CD plated on firm (~ 40 kPa) polyacrylamide gel were treated with (**E**) 50 μM blebbistatin, (**F**) 10 μM ML-7, or (**G**) 20 μM PF228, CD (green) was turned off and YAP (red) was localized in cytoplasm. DAPI (blue, nuclear counterstain) is displayed. Scale bar = 100 μm.

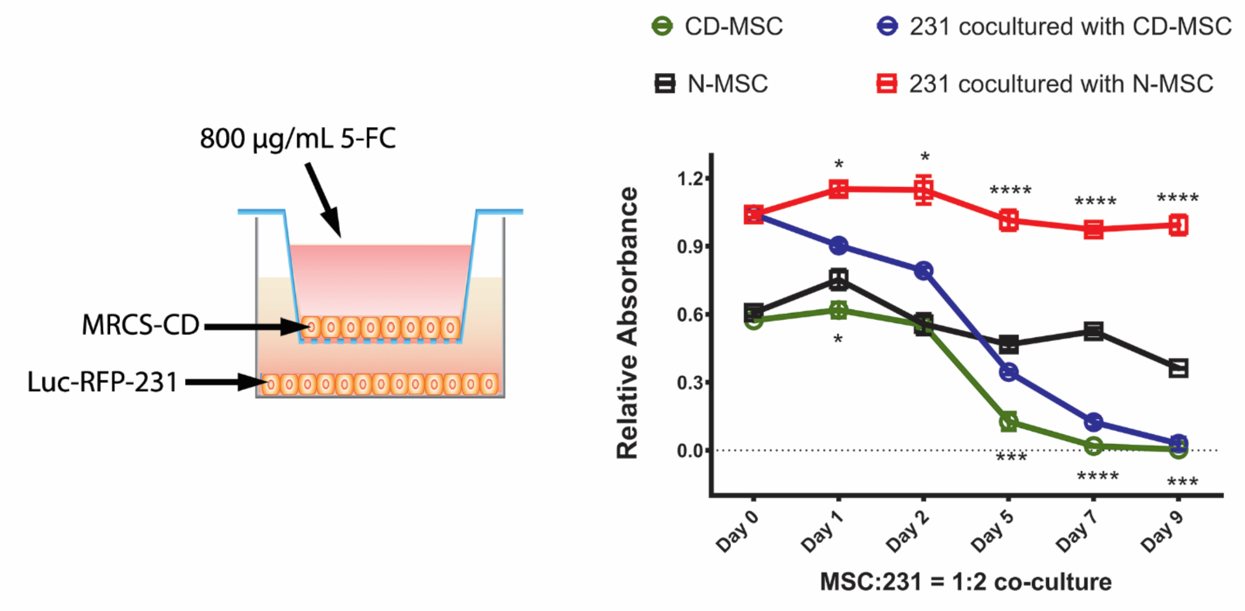

Fig. 2.S8. Bystander effect from MRCS-CD starting at 24 hours in vitro on stiff substrate

Co-culture of MRCS-CD (upper chamber) and Luc-RFP-231 (bottom chamber) was performed using transwell (MSC: 231=1:2) in the presence of 800 μg/ml 5-FC. On day 0 (cell seeding), day 1, day 2, day 5, day 7, and day 9, XTT assay was performed to measure the proliferation of cells. Triplicate samples were used for the analysis. Data shown as mean ± SD. *$P < 0.05$, ***$P < 0.001$, and ****$P < 0.0001$.

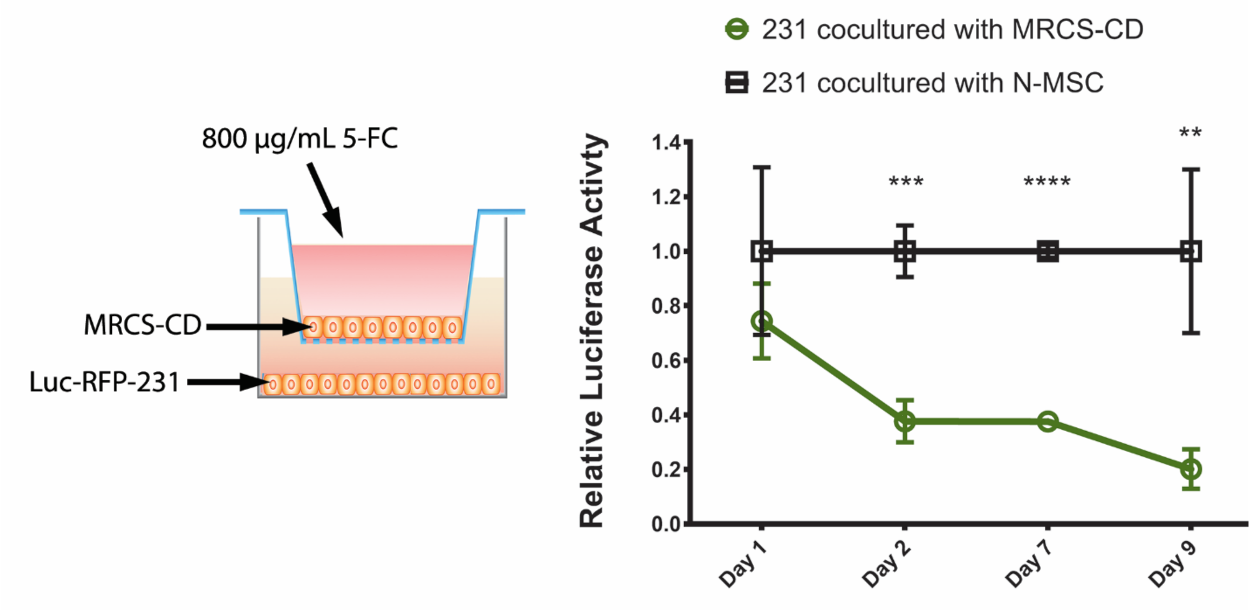

Fig. 2.S9. Bystander effect from MRCS-CD lasts after MSC removal in vitro on stiff substrate

Co-culture of MRCS-CD (upper chamber) and Luc-RFP-231 (bottom chamber) was performed using transwell (MSC: 231=1:2) in the presence of 800 µg/ml 5-FC. MSCs were removed on day 1, day 2, day 7, or day 9, and in vitro luciferase proliferation assay was performed on day 9 to measure the signals from Luc-RFP-231. n.s., not significant, $^{**}P < 0.01$, $^{***}P < 0.001$, and $^{****}P < 0.0001$. Triplicate samples were used for the analysis. Data shown as mean ± SD.

Table 1. Primary antibodies

Antigen	**Company**	**Catalog #**	**Dilution**	**Notes**
Annexin V	Bioss Antibodies	bs-0398R	1: 100	
Cytosine deaminase	Bioss Antibodies	bs-2950R	1: 100	Fig.4.1 & 3.S2
Cytosine deaminase	Thermo Fisher	PA185365	1: 200	Fig.2.S6 & 2.S7
eGFP	Abcam	ab111258	1: 100	Fig.3.S3
eGFP	Abcam	ab13970	1: 500	Fig.2.1 & 2.S4
eGFP	Thermo Fisher	OSE00001G	1: 100	Fig.4.1
Firefly luciferase	Abcam	ab21176	1: 100	Fig.3.S3
Firefly luciferase	Abcam	ab181640	1: 100	Fig.4.1 & 3.S2
Lysyl oxidase (LOX)	Abcam	ab31238	1: 100	
PARP p85 fragment	Promega	G7341	1: 100	
YAP	Santa Cruz Biotechnology	sc-101199	1: 100	Ref. 12
CD45R/B220	BioLegend	103212	N/A	APC
CD11b	BioLegend	101206	N/A	FITC
Ly-6G (Gr-1)	TONBO Biosciences	60-5931	N/A	PE-Cy7

Table 2. Secondary antibodies

Tag	**Species**	**Catalog #**	**Dilution**
Alexa Fluor 488	Donkey α chicken	ab63507 (Abcam)	1: 1000
Alexa Fluor 488	Donkey α goat	705-545-147	1: 500
Alexa Fluor 488	Donkey α rabbit	711-545-152	1: 500
Alexa Fluor 488	Donkey α sheep	713-545-003	1: 500
Rhodamine (TRITC)	Donkey α goat	705-025-147	1: 500
Rhodamine (TRITC)	Donkey α rabbit	711-025-152	1: 500
Alexa Fluor 594	Goat α mouse	115-585-062	1: 500
Alexa Fluor 647	Donkey α rabbit	711-605-152	1: 500

All secondary antibodies were purchased from Jackson ImmunoResearch Laboratories except for ab63507.

Table 3. Primers used in qPCR

Name	**Sequence**	**Notes**
GAPDH-C-F1	5’ – CTC CTG CAC CAC CAA CTG CT – 3’	Ref. 12
GAPDH-C-R2	5’ – GGG CCA TCC ACA GTC TTC TG – 3’	
ANKRDI-C-F	5’ – AGT AGA GGA ACT GGT CAC TGG – 3’	
ANKRDI-C-R	5’ – TGG GCT AGA AT GTC TTC AGA T – 3’	
CTGF-C-F	5’ – AGG AGT GGG TGT GTG ACG A – 3’	
CTGF-C-R	5’ – CCA GGC AGT TGG CTC TAA TC – 3’	
GFP-F	5’ – CTG CTG CCC GAC AAC CAC – 3’	Ref. 23
GFP-R	5’ – ACC ATG TGA TCG CGC TTC TC – 3’	
CDy-F	5’ – ACC ATG GTC ACA GGA GGC AT – 3’	Ref. 24
CDy-R	5’ – TTC TCC AGG GTG CTG ATC TC – 3’	

All primers were purchased from Integrated DNA Technologies (IDT).

2.9 References

1. Ankrum, J. and J.M. Karp, *Mesenchymal stem cell therapy: Two steps forward, one step back.* Trends Mol Med, 2010. **16**(5): p. 203-9.
2. Karp, J.M. and G.S. Leng Teo, *Mesenchymal stem cell homing: the devil is in the details.* Cell Stem Cell, 2009. **4**(3): p. 206-16.
3. Trounson, A., et al., *Clinical trials for stem cell therapies.* BMC Med, 2011. **9**: p. 52.
4. Liu, L., et al., *From blood to the brain: can systemically transplanted mesenchymal stem cells cross the blood-brain barrier?* Stem Cells Int, 2013. **2013**: p. 435093.
5. Wang, H., et al., *Trafficking mesenchymal stem cell engraftment and differentiation in tumor-bearing mice by bioluminescence imaging.* Stem Cells, 2009. **27**(7): p. 1548-58.
6. Reagan, M.R. and D.L. Kaplan, *Concise review: Mesenchymal stem cell tumor-homing: detection methods in disease model systems.* Stem Cells, 2011. **29**(6): p. 920-7.
7. Zlotnik, A., A.M. Burkhardt, and B. Homey, *Homeostatic chemokine receptors and organ-specific metastasis.* Nat Rev Immunol, 2011. **11**(9): p. 597-606.
8. Engler, A.J., et al., *Matrix elasticity directs stem cell lineage specification.* Cell, 2006. **126**(4): p. 677-89.
9. Park, J.S., et al., *The effect of matrix stiffness on the differentiation of mesenchymal stem cells in response to TGF-beta.* Biomaterials, 2011. **32**(16): p. 3921-30.
10. Tse, J.R. and A.J. Engler, *Stiffness gradients mimicking in vivo tissue variation regulate mesenchymal stem cell fate.* PLoS One, 2011. **6**(1): p. e15978.
11. Samani, A., J. Zubovits, and D. Plewes, *Elastic moduli of normal and pathological human breast tissues: an inversion-technique-based investigation of 169 samples.* Phys Med Biol, 2007. **52**(6): p. 1565-76.
12. Dupont, S., et al., *Role of YAP/TAZ in mechanotransduction.* Nature, 2011. **474**(7350): p. 179-83.
13. Halder, G., S. Dupont, and S. Piccolo, *Transduction of mechanical and cytoskeletal cues by YAP and TAZ.* Nat Rev Mol Cell Biol, 2012. **13**(9): p. 591-600.
14. Swift, J., et al., *Nuclear lamin-A scales with tissue stiffness and enhances matrix-directed differentiation.* Science, 2013. **341**(6149): p. 1240104.
15. Seo, B.R., et al., *Obesity-dependent changes in interstitial ECM mechanics promote breast tumorigenesis.* Sci Transl Med, 2015. **7**(301): p. 301ra130.
16. Hong, J.H., et al., *TAZ, a transcriptional modulator of mesenchymal stem cell differentiation.* Science, 2005. **309**(5737): p. 1074-8.
17. Aboody, K.S., et al., *Neural stem cell-mediated enzyme/prodrug therapy for glioma: preclinical studies.* Sci Transl Med, 2013. **5**(184): p. 184ra59.
18. Aboody, K.S., et al., *Targeting of melanoma brain metastases using engineered neural stem/progenitor cells.* Neuro Oncol, 2006. **8**(2): p. 119-26.
19. Vick, J.E., et al., *Optimized compatible set of BioBrick vectors for metabolic pathway engineering.* Appl Microbiol Biotechnol, 2011. **92**(6): p. 1275-86.
20. Patel, M.R., et al., *Longitudinal, noninvasive imaging of T-cell effector function and proliferation in living subjects.* Cancer Res, 2010. **70**(24): p. 10141-9.
21. Liu, L., et al., *Exogenous marker-engineered mesenchymal stem cells detect cancer and metastases in a simple blood assay.* Stem Cell Res Ther, 2015. **6**(1): p. 181.
22. Tse, J.R. and A.J. Engler, *Preparation of hydrogel substrates with tunable mechanical properties.* Curr Protoc Cell Biol, 2010. **Chapter 10**: p. Unit 10 16.

23. Mangeat, B., et al., *Broad antiretroviral defence by human APOBEC3G through lethal editing of nascent reverse transcripts.* Nature, 2003. **424**(6944): p. 99-103.
24. Kucerova, L., et al., *Cytosine deaminase expressing human mesenchymal stem cells mediated tumour regression in melanoma bearing mice.* J Gene Med, 2008. **10**(10): p. 1071-82.

CHAPTER 3:
MRCS AS A CANCER THERAPEUTIC IN VIVO

Authors: Linan Liu[1-6]† , **Shirley X. Zhang**[1-6]†, Wenbin Liao[1-6], Henry P. Farhoodi[1-6], Chi W. Wong[1-6], Claire C. Chen[1-6], Aude I. Ségaliny[1-6], Jenu V. Chacko[5], Lily P. Nguyen[1-6], Mengrou Lu[1-6], George Polovin[1-6], Egest J. Pone[1-6], Timothy L. Downing[1,5], Devon A. Lawson[1,3,7], Michelle A. Digman[5,8,9], Weian Zhao[1-6]

Affiliations:

[1]Sue and Bill Gross Stem Cell Research Center, 845 Health Sciences Road, University of California-Irvine, Irvine, California, 92697, USA.

[2]Department of Pharmaceutical Sciences, University of California-Irvine, Irvine, California, 92697, USA.

[3]Chao Family Comprehensive Cancer Center, University of California-Irvine, Irvine, California, 92697, USA.

[4]Edwards Life Sciences Center for Advanced Cardiovascular Technology, University of California-Irvine, Irvine, California, 92697, USA.

[5]Department of Biomedical Engineering, University of California-Irvine, Irvine, California, 92697, USA.

[6]Department of Biological Chemistry, University of California-Irvine, Irvine, California, 92697, USA.

[7]Department of Physiology & Biophysics, University of California-Irvine, Irvine, California, 92697, USA.

[8]Laboratory for Fluorescence Dynamics, University of California-Irvine, California 92697, USA.

[9]Centre for Bioactive Discovery in Health and Ageing, School of Science and Technology, University of New England, Armidale, New South Wales 2351, Australia.

† These authors contributed equally to this work.

3.1 Introduction

Here, after characterizing the mechanisms and functionality of MRCS *in vitro* we will then demonstrate the capability of MRCS to deliver therapeutics to effectively kill cancer cells *in vivo*, as demonstrated in a metastatic breast cancer mouse model. An advantage of using MRCS is the active homing of MSCs to metastatic sites. This tumor tropism allows for localized delivery of cancer therapeutics while not affecting surrounding healthy tissues. Due to this, MRCS also has markedly reduced deleterious effects compared to MSCs constitutively expressing therapeutics while maintaining significant therapeutic efficacy over control groups.

3.2 Establishing Murine Models of Metastasis

As a model of breast cancer metastasis to the lung, we used an MDA-MB-231 xenotransplantation model in mice. We chose MDA-MB-231 cells because they secrete large amounts of LOX, which increases the crosslinking of collagen fibrils in the lung that is essential for metastasis [1]. MDA-MB-231 cells were engineered to express reporters including eGFP (eGFP-231) or firefly luciferase plus RFP (Luc-RFP-231) and seeded via tail vein injection in immunocompromised mice to establish tumor foci in the lung (4-6 weeks after cancer infusion) (Fig. 3.1, A and B, animals on Day 0) before MSC infusion. In this study, we used two sets of immunocompromised mice: *Foxn1^{nu}* (nude) and nonobese diabetic/severe combined immunodeficiency gamma (NSG). We primarily focused on the nude mouse system because it is partially immunocompromised and therefore more likely recapitulates the clinical setting than NSG. They also have better health condition than NSG mice after cancer seeding, allowing us to monitor the course of treatment for a longer period

[2]. On the other hand, NSG mice establish tumors more robustly and rapidly, and therefore were also used when we examined MRCS tumor-homing and correlation between collagen crosslinking, tumor cells, and MRCS activation in ex vivo immunofluorescence and second harmonic generation (SHG) experiments [2, 3].

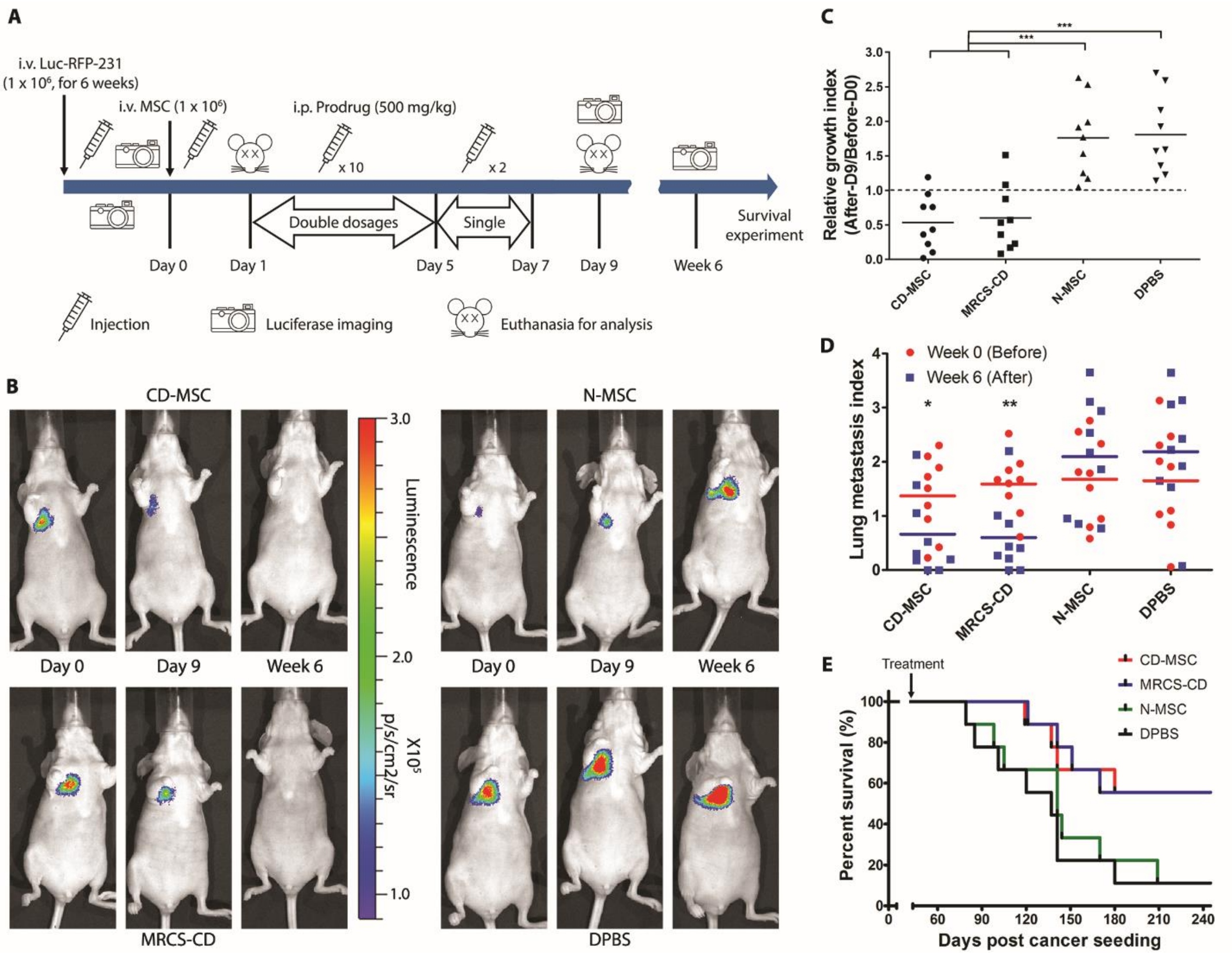

Fig. 3.1. MRCS-CD killing cancer cells in vivo

(**A**) Design and timeline of animal experiment to test MRCS-CD with 5-FC in vivo. (**B**) Representative pictures of nude mice that received MRCS-CD treatments show that MRCS-CD decreased lung metastasis signals in vivo. Luciferase imaging was taken before (D0, left panels) and on 5-FC treatment short-term (D9, middle panels), as well as long-term (6 weeks, right panels). Quantification of luciferase signals in the lungs in vivo after (**C**) short-term and (**D**) long-term treatment. (**E**) Mouse survival after MRCS-CD treatment. In panel **C**, Relative Growth Index (RGI) = luciferase read on D9 (after) / luciferase read on D0 (before). In panel **D**, Lung Metastasis Index (LMI) = Log_{10} [(luciferase read of the tested mouse) / (luciferase read of average for tumor-free mice)]; the LMI of tumor-free mice = 0. The differences between "week 0" groups are not statistically significant. $n = 9$ for each group. *$P < 0.05$, **$P < 0.01$, and ***$P < 0.001$. Data shown as mean ± SD. In panel **E**, P value: *CD-MSC vs. DPBS = 0.0382; *MRCS-CD vs. N-MSC = 0.0429; *MRCS-CD vs. DPBS = 0.0211. Median survival (days): CD-MSC: 260; MRCS-CD: 260; N-MSC: 141; DPBS: 137.

3.3 MRCS Homing to the Metastatic Niche

MSCs home to both primary tumor and metastatic sites including breast cancers [4-6]. In this study, we first examined whether MSCs engineered to constitutively express firefly luciferase (Luc-MSC) are able to home to the lungs. We systemically infused Luc-MSC into mice hosting human eGFP-231 breast cancer cells in the lung and tumor-free controls. We found that Luc-MSC homed to and persisted in the lungs (fig. 3.S1). Next, we investigated whether MRCS can home to and be specifically activated at the tumor sites using MRCS-Luc, which served as a surrogate for MRCS-CD and allowed us to readily track transplanted MRCS and monitor their activation using induced luciferase in vivo. We demonstrated that systemically infused MRCS-Luc homed to and were induced to express luciferase only in the tumor sites in the lung of eGFP-231 tumor-bearing mice (fig. 3.S2, A and B). The observed luciferase signal, which reflects the collective functional outcome of MRCS homing and activation at tumor sites, persisted in tumor-bearing mice for up to 1-2 days (fig. 3.S2B). Given that previous studies, including our own, have consistently demonstrated that systemically transplanted MSCs can persist in tumor sites for up to a week, we suspect that some residual MRCS might exist in tumors after 2 days following transplantation but become undetectable due to the limited sensitivity of in vivo luciferase imaging [6]. Finally, we confirmed the in vivo homing and activation of MRCS-CD in Luc-RFP-231 tumor-bearing mice using ex vivo immunohistochemistry (IHC). We demonstrated that MRCS-CD co-localized with and were locally activated to express CD at cancer sites in lung sections of tumor-bearing (but not tumor-free) mice (fig. 3.S2, C and D). Similar results were observed with the infusion of MRCS-eGFP (fig. 3.S3). Collectively, these data suggest that MRCS selectively home to and are specifically activated at the metastatic niche in vivo. This set of experiments also allowed us to identify time points at which MRCS persisted and were activated in tumors in vivo to guide the schedule of treatment (5-FC).

3.4 MRCS Kills Cancer *in vivo*

To evaluate the efficacy of MRCS-CD for treating breast cancer lung metastasis, mice seeded with Luc-RFP-231 cancer cells for 6 weeks were given MRCS-CD (on Day 0) followed by prodrug 5-FC and were monitored for therapeutic outcomes (Fig. 3.1A). MRCS-CD were administered 1 day before the start of prodrug treatment to allow time for co-localization with tumors in the lungs. 5-FC was given in multiple doses for 7 days, which is consistent with the typical MSC persistence period in the tumor [4, 6]. The amount of cancer within the lungs was quantified by measuring the cancer luciferase signal using in vivo imaging (Fig.

3.1B). Compared to initial values before prodrug treatment, luciferase signals were decreased in mice treated with MRCS-CD and MSCs engineered to constitutively express CD (CD-MSC), both shortly after treatment (Day 9) and at 6 weeks after treatment (Fig. 3.1, C and D). N-MSC and Dulbecco's Phosphate-Buffered Saline (DPBS) control groups failed to decrease lung metastasis signals, and in fact showed increase of cancer mass over time as cancer continued to grow, as expected. Cancer signals after prodrug treatment (Day 9) were normalized to cancer signals before treatment (Day 0) for each mouse, which quantitatively demonstrated that CD-MSC and MRCS-CD significantly decreased the amount of cancer compared to N-MSC and DPBS groups ($P < 0.001$, Fig. 3.1C). Long-term (6 weeks after treatment), CD-MSC and MRCS-CD treated groups maintained a lower amount of lung metastasis compared to the Day 0 baseline values ($P < 0.05$), whereas N-MSC and DPBS groups saw an overall increase in cancer signals over time (Fig. 3.1D). Survival outcomes were also significantly improved by CD-MSC and MRCS-CD treatment compared to N-MSC and DPBS groups ($P < 0.05$, Fig. 3.1E). It should be noted that without 5-FC injection, MRCS-CD could not attenuate cancer growth in vivo (fig. 3.S4). Note that, starting from Day 120 (Week 18), the survival rate of the MRCS treated group started to decline (Fig. 3.1E), suggesting that in some animals, lung tumors were decreased rather than totally cleared out by a single MRCS treatment. This demonstrates the potential need for repeated cell infusion together with prodrug administration [7].

3.5 Evaluating Side Effects of MRCS

Because intravenous delivery of MSCs, used in most clinical trials, results in initial entrapment of large numbers of MSCs in the pulmonary vasculature [8], localized activation of a prodrug, rather than constitutively expressing a drug, at only the metastatic niche is desirable to reduce off-target toxicity in the pulmonary and other organ systems. Though CD-MSC and MRCS-CD had similar treatment outcomes in terms of efficacy, constitutively expressing CD would convert systemically infused 5-FC indiscriminately in tumor-bearing and tumor-free tissue alike. MRCS-CD, however, would only express CD to activate 5-FC conversion at sites of increased stiffness, as found in tumor sites, and therefore have less damaging systemic side effects. To examine the side effects of MRCS-CD and compare it to CD-MSC, we used immunostaining of Annexin V and Terminal deoxynucleotidyl transferase dUTP Nick End Labeling (TUNEL) assay (Fig. 3.2A). Staining for Annexin V to measure apoptosis showed the specific activation of MRCS-CD at tumor sites, whereas no comparable Annexin V signal could be seen on tumor-free tissue. CD-MSC treated group stained positive for Annexin V non-specifically, indicating extensive tissue damage. Mice treated with N-MSC or DPBS stained positive for tumor but not for Annexin V, indicating that native MSC or DPBS infusion does not cause cytotoxicity. TUNEL analysis for damaged DNA further confirmed higher lung tissue damage in CD-MSC group than for any other group after treatment, including MRCS-CD (Fig. 3.2B). Specifically, MRCS-CD caused localized cell apoptosis only at the tumor sites with minimal lung tissue damage compared to constitutively CD-expressing control. In tumor-free mice, there was no significant increase in tissue damage after treatment with MRCS-CD, demonstrating specificity of activation only at tumor sites. Collectively, our data suggest that MRCS-CD kill cancer specifically with minimized side effects in vivo compared to MSC constitutively expressing therapeutics.

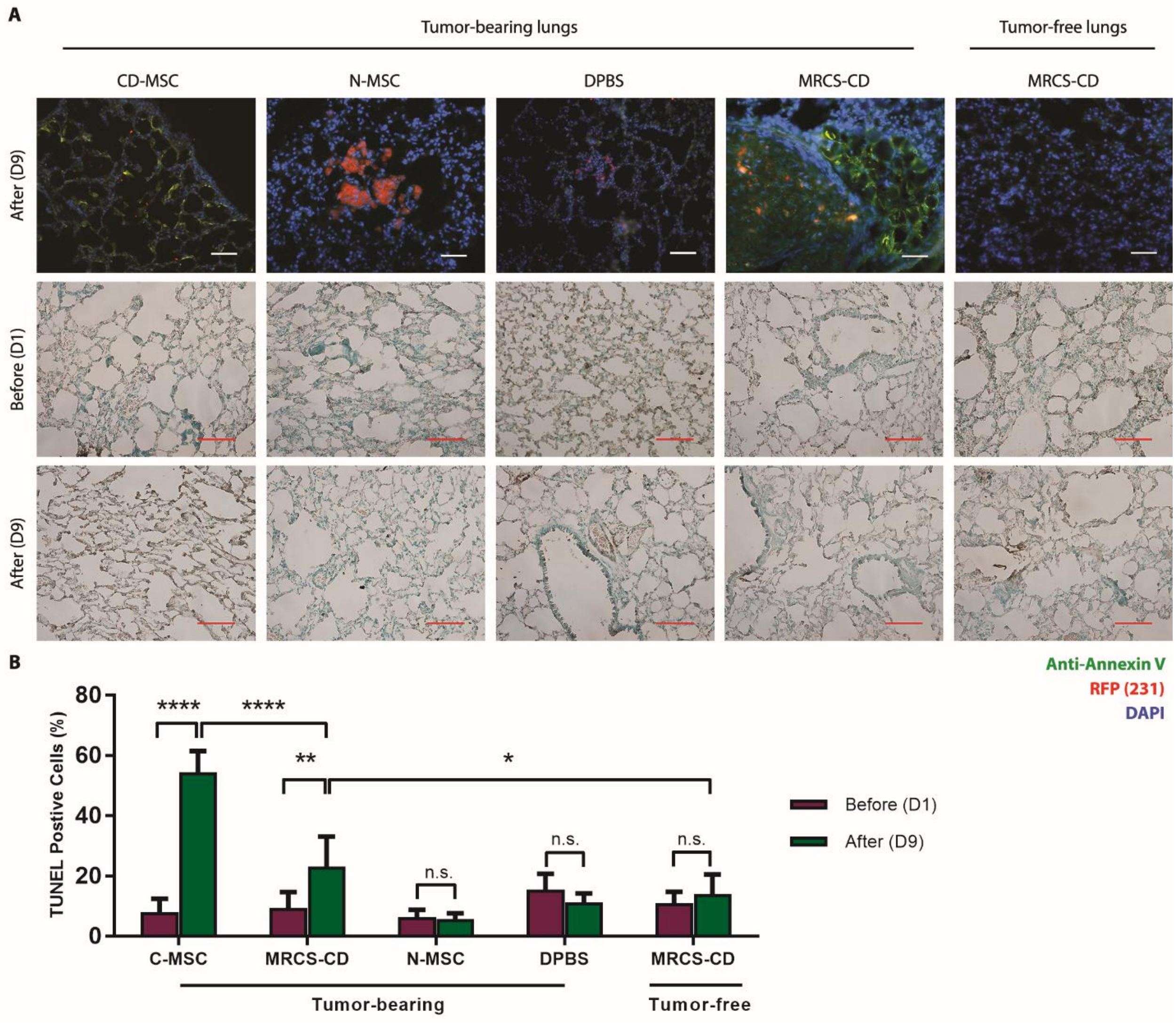

Fig. 3.2. MRCS-CD killing cancer cells in vivo with minimal side effects

(**A**) Frozen sections of lungs of Luc-RFP-231 tumor-bearing and tumor-free nude mice sacrificed 24 hours after CD-MSC, N-MSC, DPBS, or MRCS-CD infusion were stained with anti-Annexin V (green) and DAPI (blue). RFP signal (red) indicates the presence of lung metastasis. Scale bar = 100 μm. (Representative images of frozen section samples of tumor-bearing lungs and tumor-free lungs from nude mice treated with CD-MSC, MRCS-CD, N-MSC, or DPBS before and after 5-FC injections by TUNEL assays. Horseradish peroxidase (HRP) signals (brown) indicate damaged nuclei, and green signals are methyl green counterstain of normal nuclei. Scale bar = 100 μm. (**B**) Quantification of TUNEL assay data measuring lung tissue damage in vivo. 10 representative images were used per group for quantification. n.s., not significant, **P* < 0.05, ***P* < 0.01, and *****P* < 0.0001. Data shown as mean ± SD.

Potential side effects to other tissues besides the lungs were also evaluated. In particular, we focused on damage to bone marrow, liver, and brain, because these are other sites to which MSCs may home [9]. Flow cytometry for bone marrow cells showed no significant increase in apoptosis or necrosis after treatment with MRCS-CD in nude mice (fig. 3.S5A). There was also no significant change in the bone marrow cell population after treatment (fig. 3.S5B), showing that the bone marrow was not depleted by the MRCS-CD treatment, unlike in conventional chemotherapy [10]. There was also no observable damage in bone marrow (fig. 3.S6), liver (fig. 3.S7), or brain tissue (fig. 3.S8) sections stained by hematoxylin and eosin (H&E). The data suggest that MRCS-CD do not induce non-specific damage to other tissues.

3.6 Discussion

The primary concern of using MRCS for treating cancer is potential off-target activation and unwanted tissue damage. Although several organs, including muscle (12 kPa) and bone (25-60 kPa) [11, 12], approach or exceed the tissue stiffness of invasive breast cancer and may promote activation of our MRCS, we anticipate this will not be a major issue due to the inherent homing ability of MSCs to cancer and metastases and their rapid clearance from non-inflamed or non-injured tissues [9, 13]. Indeed, our data showed no significant damage to bone, bone marrow, liver, or brain tissues as a result of systemic treatment with MRCS (although we emphasize that MSC type and administration route may affect their homing profile). Although in transit to the metastatic niche MSCs will encounter blood vessel endothelial cells, basement membrane, and ECM components, each with their own characteristic stiffness, we do not expect this to irreversibly influence MRCS activity [11]. In particular, many of these mechanical interactions involve shear stress, which does not regulate MSC differentiation. Previous studies have also established that expression of mechano-responsive genes is rapidly reversible [11, 14]. The specificity of MRCS co-localization and activation on tumors was also demonstrated in our study, with targeted release of CD only in regions with cancer cells and high collagen crosslinking, resulting in localized tissue damage in these tumor regions but not in other, non-tumor regions. This, combined with data which show that MRCS will not release CD to convert 5-FC while on soft substrates, demonstrates that MRCS should not result in off-target damage in healthy tissues.

In contrast, treatment with CD-MSC did result in increased tissue damage in the lungs, which was not restricted to tumor regions but was also observed in healthy tissues. This could be at least partially attributed to initial entrapment of MSCs in the pulmonary vasculature [8], where CD-MSC could still express CD to cause non-specific damage, whereas MRCS-CD would be inactive. Although CD-MSC and MRCS-CD displayed similar in vivo treatment efficacy and similar survival curves, this phenomenon may be attributed to the cell therapies reaching a threshold level of cancer killing, beyond which survival curves and whole body imaging may not be sensitive enough to distinguish the two treatment groups. Further optimization of treatment parameters such as initial tumor burden, timing, and dosage of treatment and using more sensitive imaging modalities may elucidate these differences in future studies. Future studies will also need to further investigate the activation of MRCS in vivo to fully characterize the conditions in the tumor microenvironment which trigger the conversion of 5-FC. However, it should be emphasized that MRCS-CD attenuated tumor growth. Taken together, the data suggest that MRCS is effective as a cancer therapeutic and has advantages over CD-MSC with respect to reducing side effects.

3.6 Materials and Methods

Breast cancer lung metastasis animal models

0.5 x 10^6 (2.5 x 10^6/ml in Dulbecco's Phosphate-Buffered Saline (DPBS, Lonza)) LV-*CMV*::Luc-RFP MDA-MB-231 (Luc-RFP-231), or LV-*CMV*::eGFP MDA-MB-231 (eGFP-231) breast cancer cells were infused intravenously (*i.v.*) into immunocompromised female nude mice (8 weeks, #088, Charles River Laboratories) or NOD-SCID gamma (NSG) mice (8 weeks, #005557, The Jackson Laboratory). For the spontaneous metastasis model, 1 x 10^6 Luc-RFP-231 cells in Matrigel were implanted subcutaneously (*s.c.*) into the fat pads of female NSG mice (8 weeks). All animals injected with cancer cells or DPBS as healthy controls were picked randomly. All animal experiments and procedures were performed after the approval from the University of California Irvine (UCI) Institution of Animal Care and Use Committee (IACUC protocol number 2012-3062) and conducted according to the Animal Welfare Assurance (#A3416.01).

MSC transplantation and prodrug treatment

Four (NSG *i.v.* model) or six (nude *i.v.* model or NSG *s.c.* model) weeks after Luc-RFP-231 cell transplantation, 1 x 10^6 LV-*CMV*::eGFP MSCs co-transduced with MRCS-CD (eGFP-MRCS-CD), LV-MRCS-eGFP MSCs (MRCS-eGFP), CD-MSC, MRCS-CD, N-MSC (5 x 10^6 /ml in DPBS), or DPBS were *i.v.* infused into the mice harboring breast cancer cells and into tumor-free control mice (Day 0) through the tail vein. For second harmonic generation (SHG) imaging and immunohistochemistry (IHC) (ex vivo), animals infused with eGFP-MRCS-CD or MRCS-eGFP were euthanized *(n* = 3 for each group) 24 hours later (Day 1) and lungs were harvested. For the cancer treatment experiment, Luc-RFP-231 tumor-bearing or tumor-free mice infused with CD-MSC, MRCS-CD, N-MSC, or DPBS were intraperitoneally (*i.p.*) treated with 5-FC (500 mg/kg in DPBS) for 7 days (two doses/day for Day 1-Day 5 and one dose/day for Day 6-Day 7). Representative mice (*n* = 3 for each group) were euthanized on Day 1 and Day 9 for ex vivo assays. For the survival experiment, the endpoint for mice was defined as "found dead" or euthanasia criteria stated in UCI IACUC protocol 2012-3062. For the survival experiment, the endpoint for mice was defined as "found dead" or euthanasia criteria stated in UCI IACUC protocol 2012-3062: that is, a condition scoring system was used to monitor if the mouse has body weight loss (0 to 3), abnormalities on physical appearance (0 to 3), unprovoked behavior (0 to 3), and/or abnormal behavioral responses to external stimuli (0 to 3), with 0 being healthy. Any mouse was to be euthanized if 1) the total score was ≥ 5 or 2) it scored a "3" for any variable regardless of the total score.

In vivo and ex vivo bioluminescence imaging

Four (NSG *i.v.* model) or six (nude *i.v.* model or NSG *s.c.* model) weeks after Luc-RFP-231 cell transplantation, in vivo Luc activity from Luc-RFP-231 cells was measured (Day 0) as previously described [15]. Briefly, in vivo Luc signal was imaged with IVIS Lumina (Caliper LifeSciences) 10 minutes after intraperitoneal (*i.p.*) injection of D-luciferin (150 mg/kg in DPBS) into mice. Mice were anesthetized with 2-3% of isoflurane (Western Medical Supply), and in vivo Luc activity was measured at the indicated time points. Before cancer treatment, nude mice with Luc signals in the lungs were imaged and grouped randomly. Minimal adjustment was performed to keep the differences between "week 0" groups (red spots) not statistically significant. After the cancer treatment experiments, in vivo Luc activity from Luc-RFP-231 cells was measured on Day 9 and 6 weeks after treatment.

Four (NSG) or six (nude) weeks after eGFP-231 cell transplantation, 1 x 10^6 Luc-MSC, MRCS-Luc, N-MSC (5 x 10^6 /ml in DPBS), or DPBS were systemically infused into the mice harboring breast cancer cells and into tumor-free control mice (Day 0). In vivo Luc activity was measured at the indicated time points.

Six weeks after *s.c.* Luc-RFP-231 cell transplantation, mice were sacrificed and lungs were harvested. 150 μg/ml D-luciferin was added onto the lungs, and ex vivo Luc activity from Luc-RFP-231 cells in the lungs was measured with IVIS Lumina.

Tissue processing, histology, and TUNEL assays

Lungs, livers, and brains were collected from tumor-bearing or tumor-free nude mice (Day 0 or Day 9). After overnight fixation in 4% PFA, followed by overnight incubation in 30% sucrose solution (Amresco), samples were flash frozen in Tissue-Tek O.C.T Compound

(Sakura Finetek). Frozen sections 8 μm thick were taken using a Reichert-Jung Cryocut 1800 microtome (Leica Instruments) onto UltraClear positively charged slides (Denville, 25 x 75 x 1 mm). Bones were fixed overnight in 4% PFA, then decalcified for 10 days in a 14% EDTA solution with 0.2% PFA in PBS before embedding in paraffin and sectioning with a Leica microtome.

Masson's trichrome staining was performed to assess extent of tissue crosslinking and fibrosis (Day 0). Slides were fixed in Bouin's solution (Sigma) overnight at room temperature, then briefly rinsed in tap water before further washing in water on a shaker for 20 minutes. Slides were stained in a working solution of Weigert's hematoxylin (1: 1 ratio of solution A and solution B, Sigma) for 8 minutes and washed thoroughly in running tap water. Slides were then stained in Biebrich scarlet-acid fuchsin solution (Sigma) for 5 minutes and washed in water. Slides were differentiated in a 1: 1 phosphomolybdic-phosphotungstic acid solution (Sigma) for 5 minutes. Slides were then stained in aniline blue solution (Sigma) for 5 minutes and differentiated in a 1% acetic acid (Sigma) solution for 2 minutes. Finally, slides were rinsed in water, then dehydrated with a few dips each in 70%, 90%, and 100% ethanol and cleared for 1 minute in Histoclear (Thermo Fisher Scientific) before mounting with Permount (Thermo Fisher Scientific).

Terminal deoxynucleotidyl transferase dUTP nick end labeling (TUNEL) assay was performed to further assess tissue damage (Day 0 and Day 9). The ApoBrdU-IHC DNA Fragmentation Assay Kit (Biovision) was used with the included protocol. Data were analyzed with ImageJ (http://imagej.nih.gov/, NIH). For each picture, the areas of TUNEL-positive cells (stained brown, [T+]) and those of TUNEL-negative cells (stained blue, [T-]) were extracted with ImageJ. Then the percentage of TUNEL-positive cells was calculated as

X = [T+] / ([T+] + [T-]) x 100%. 10 representative pictures per group were included in the analysis.

Hematoxylin and eosin (H&E) staining was performed to assess systemic tissue damage in lung, liver, brain, and bone. Slides were stained with Harris hematoxylin (Sigma) for 10 minutes, followed by acid alcohol (1% HCl in 70% ethanol), Scott's bluing reagent (Sigma) for 1 minute, and Eosin Y (Sigma) for 5 minutes. Slides were dehydrated and mounted as described above.

Ex vivo immunohistochemistry

Lung tissues were harvested from tumor-bearing or tumor-free nude or NSG mice (Day 0 for LOX staining, Day 1 for MRCS homing and activation, and Day 9 for Annexin V) and processed as mentioned above. Frozen slides (8 μm) were thawed and rehydrated in dH_2O for 5 minutes, then fixed in chilled acetone (Thermo Fisher Scientific) at -20°C for 10 minutes, permeabilized in 0.1% Triton X-100 for 10 minutes, and blocked in 0.1% Triton X-100 with 5% normal donkey serum for 1 hour. Primary antibodies (Table 1) were diluted 1: 100 from the stock solution and applied overnight at 4°C. Slides were washed in 1X PBS. Then, secondary antibodies (Table 2) were diluted 1: 500 from the stock solution and applied for 30 minutes at room temperature. Slides were stained for nuclei with DAPI (1 μg/ml), then washed in PBS and mounted with Fluoromount-G. Slides were imaged with Nikon Eclipse Ti inverted microscope.

Second Harmonic Generation (SHG) Imaging

For SHG imaging, frozen 40 μm sections of fixed (for LOX-SHG co-localization) or unfixed (for MRCS-SHG co-localization and SHG quantification), OCT-mounted mouse lungs (Day 0 for LOX-SHG co-localization and Day 1 for MRCS-SHG co-localization) were obtained as mentioned above and dried overnight, in the dark, at room temperature on slides. Slides were then prepared as described in the "Ex vivo Immunohistochemistry" session. The fluorescent signals from antibody-stained slides were imaged using a Zeiss LSM710 multiphoton/confocal microscope (Zeiss) with a 40x W1.2NA objective (Zeiss). Slides were sequentially imaged in order of increasing fluorescent wavelength to reduce photo bleaching. SHG was performed at an 840 nm excitation wavelength and narrow bandpass detection, with a spectral window of 420/20 nm [16-18]. Images were processed with ImageJ and Matlab (MathWorks Inc.). For MRCS-SHG co-localization and representative images for SHG quantification, multiple high quality pictures were generated per sample and tiled into a larger image, from which the representative pictures were selected. For SHG quantification, collagen fibers imaged by SHG were automatically or manually selected, and the ratio of displacement and length of the collagen fibers were analyzed and plotted. To minimize artifacts caused by collagen bundles close to blood vessels, the fibrillar length and curvature of collagen were extracted and adjusted by quasi-manual selection of fibrillar structures. CT-FIRE was used to automatically select and quantify the curvature of collagen fibers [19, 20]. Regions of the lung tissue defined as "cancer region" or "non-cancer region" were manually selected.

For SHG-PARP p85 co-localization, large lung tissue scans of fluorescent channels 594 nm (for cancer) and 640 nm (for PARP p85) were taken on a fluorescent microscope (Eclipse

Ti-E, Nikon) with 7-color Spectra X Light Engine (Lumencor) and Zyla sCMOS camera (Andor) at 20x magnification. The sample was then scanned in the same approximate area using Zeiss LSM710. The SHG scan was then overlaid upon the fluorescent scan using ImageJ to get a high-definition fluorescence and SHG combined image for analysis. The overlaid large scans were then divided into sections using a grid of approximately 500 x 500 µm. Each section of the grid was treated as a separate data point for SHG-PARP p85 co-localization.

Bone marrow flushing and flow cytometry

1 day, 2 days, 7 days, or 9 days after MSC infusion with 5-FC treatment as mentioned above, nude or NSG mice were sacrificed, and bones, specifically femurs from both legs, were harvested, with muscle tissue removed carefully. Bone marrow was then flushed with PBS, dissociated, and filtered using a 70 µm cell strainer (Corning). The red blood cells were then lysed using ammoniumchloride potassium buffer (Lonza) for 3 minutes at 37°C. The remaining cells were washed twice with PBS and diluted to 1 x 10^6 cells/ml. 300 µl of cells in suspension were then stained with either Annexin V-FITC (BioLegend) in Annexin V binding buffer (BioLegend) and 7-Aminoactinomycin D dye (7-AAD, Thermo Fisher Scientific) or anti-B220 APC (CD45R), anti-CD11b FITC, and anti-Gr-1-PE-Cy7 (Ly6G) (Table 1) according to the manufacturer's instructions. Compensation and unstained controls were also prepared for the analysis. For samples requiring multiple stains, a compensation coefficient was first estimated from controls using unstained cells or only a single stain and inputted into the analysis software to correct for fluorescent signal spillover from other channels. Finally, the cells were analyzed with a BD Accuri C6 flow cytometry machine (BD

Biosciences). The different populations were analyzed as follows: monocytes/macrophages (CD11b^{+}, Gr-1$^{neg/low}$), granulocytes (CD11b^{+}, Gr-1^{high}), and B cells (B220^{low} and B220^{high}).

Atomic force microscopy (AFM)

Six weeks after *i.v.* infusion of Luc-RFP-231 cancer cells or DPBS administration for the tumor-free control, nude mice (Day 0) were euthanized and lungs were immediately harvested and kept in ice-cold Ringer solution (Thermo Fisher Scientific). All the AFM assays were performed within 48 hours after mouse euthanasia. Lung samples were cut into 500 μm-thick slices using a rat heart slicer matrix (Zivic Instruments) and mounted to a 60 mm plastic petri dish using epoxy glue (Devcon). Samples were measured using Bruker BioScope Catalyst Atomic Force/ Zeiss LSM5 Confocal Fluorescence Microscope (Bruker/ Zeiss) using contact mode in fluid with MLCT C Triangular cantilevers (spring constant = 0.01 N/m, Bruker). Data points were taken 5 μm apart on 50 x 50 μm scans. Data were analyzed with Nanoscope Analysis v1.5 software, using a Sneddon conical model with Poisson ratio 0.4 [19, 20].

Study Design

This study was designed to investigate the hypothesis that a cell-based system can be engineered to respond specifically to mechanoenvironmental cues (MRCS) to target cancer metastases. In vitro experiments including tunable hydrogels, qPCR, co-cultures, and mass spectrometry, and in vivo and ex vivo experiments using nude and NSG mice, including luciferase imaging, antibody staining, SHG, and AFM, were performed to demonstrate that MRCS can sense and kill cancer cells in response to biophysical cues. For all in vitro studies except for mass spectrometry, three independent experiments with at least three samples per condition were performed. $n = 9$ for the in vivo cancer killing and survival assays. $n \geq 3$ for ex vivo characterization of the biophysical cues in the metastatic niche and the validation of MRCS. For the survival experiment, the endpoint for mice was defined as "found dead" or euthanasia criteria stated in UCI IACUC protocol 2012-3062 described in Supplementary Materials and Methods. Groups for animal experiments were randomized, except for the cancer killing study where manual group adjustments were performed to keep the differences in initial cancer burden between all "week 0" group animals not statistically significant. In vitro experiments were not blinded. In vivo and ex vivo experiments were blinded.

Statistical analysis

Data were analyzed by Student's *t* test when comparing 2 groups and by ANOVA when comparing more than 2 groups. Log-rank (Mantel-Cox) test was performed for animal survival data analysis by two-way ANOVA and Mann Whitney test was used for AFM data. Outliers in AFM data were removed by Grubb's test ($P < 0.05$). Data were expressed as mean ± SD or mean ± SEM. Two-sided testing with normal-based 95% confidence interval was performed for each analysis, and differences were considered significant at $P < 0.05$.

3.8 Supplemental Figures

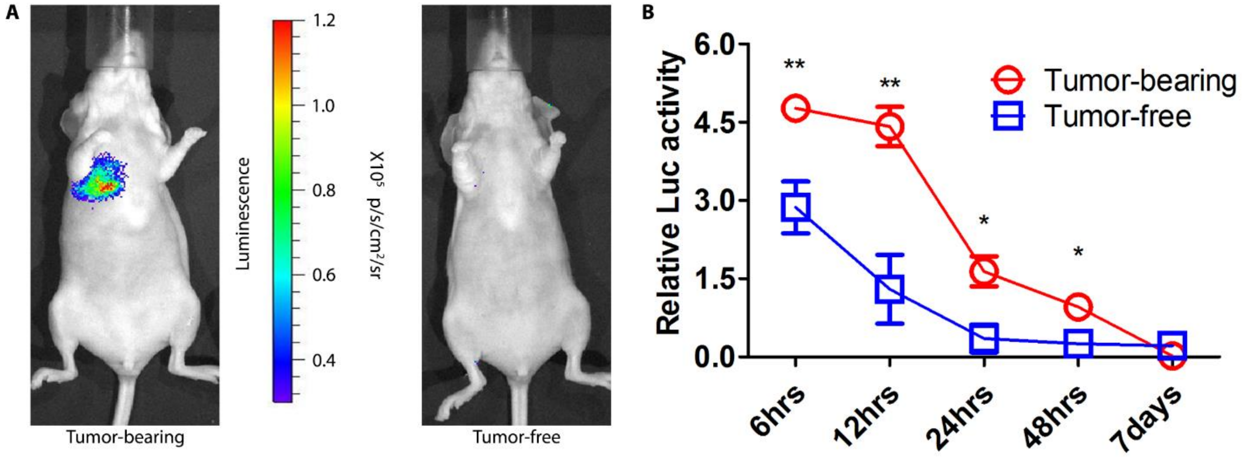

Fig. 3.S1. Luc-MSC homing to the metastatic niche in vivo

(**A**) Representative pictures of in vivo luciferase imaging of systemically infused Luc-MSC 12 hours after MSC infusion. (**B**) Quantification of luciferase activity of Luc-MSC in the lungs of eGFP-231 tumor-bearing and tumor-free nude mice at different time points after systemic infusion. MSCs persisted longer in tumor-bearing mice than in tumor-free mice but were cleared out in approximately 1 week. Relative Luc Activity = Log_2 [(luciferase read of the tested mouse infused with Luc-MSC) / (luciferase read of control mice average injected with DPBS)], such that the RLA of mice injected with DPBS = 0. *n* = 4 for tumor-bearing and *n* = 3 for tumor-free nude mice. Data shown as mean ± SEM. * $P < 0.05$, ** $P < 0.01$.

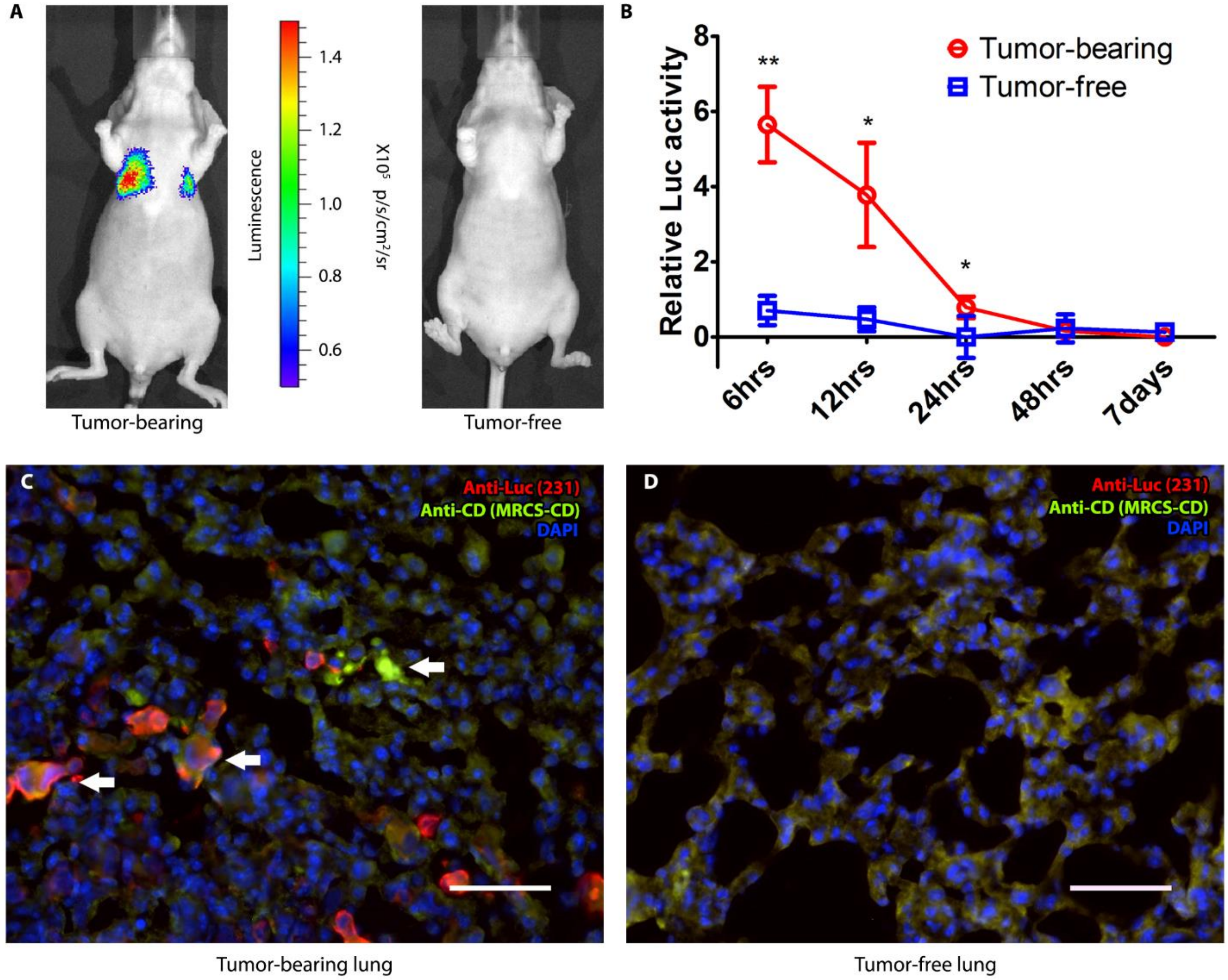

Fig. 3.S2. MRCS homing and specific activation in response to the metastatic niche in vivo

(**A**) Representative pictures of in vivo luciferase imaging of systemically infused MRCS-Luc 12 hours after infusion. (**B**) Systemically infused MRCS-Luc were turned on in the lungs of eGFP-231 tumor-bearing nude mice but not tumor-free mice. Relative Luc Activity (RLA) = Log_2 [(luciferase read of the mouse infused with MRCS-Luc) / (luciferase read of control mice average injected with DPBS)], such that the RLA of mice injected with DPBS = 0. RLA were measured and plotted for tumor-bearing and tumor-free mice at different time points after systemic infusion of MRCS-Luc. *n* = 4 for tumor-bearing and *n* = 3 for tumor-free nude mice. Data shown as mean

± SEM. * $P < 0.05$ and ** $P < 0.01$. (**C** and **D**) Frozen sections of lungs of Luc-RFP-231 tumor-bearing NSG mice and tumor-free NSG mice sacrificed 24 hours after MRCS-CD infusion were stained with anti-Luc (red) for lung metastasis, anti-CD (green) for cytosine deaminase expressed by MRCS-CD, and DAPI (blue). White arrows indicate the co-localization of lung metastatic sites and MRCS-CD expressing CD (turned on). Scale bar = 50 μm.

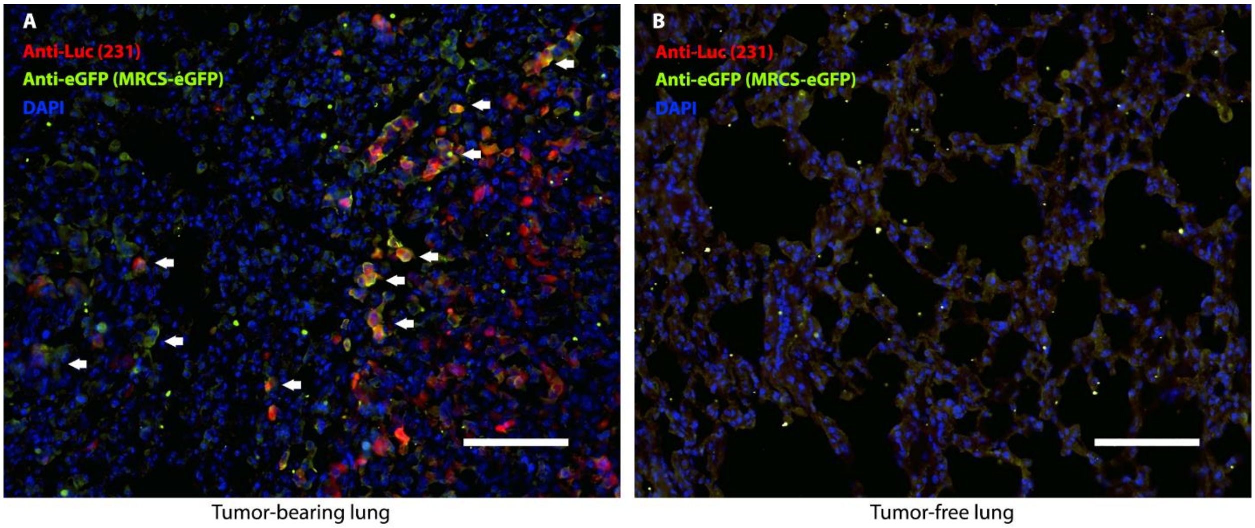

Fig. 3.S3. Specific activation of MRCS-eGFP in response to the metastatic niche in vivo

Frozen sections of lungs of (**A**) Luc-RFP-231 tumor-bearing mice and (**B**) tumor-free mice sacrificed 24 hours after MRCS-eGFP infusion were stained with anti-Luc (red) for lung metastasis, anti-eGFP for eGFP expressed by MRCS-eGFP (green), and DAPI (blue). White arrows indicate the co-localization of lung metastatic sites and MRCS-eGFP expressing eGFP (turned on). Scale bar = 100 μm.

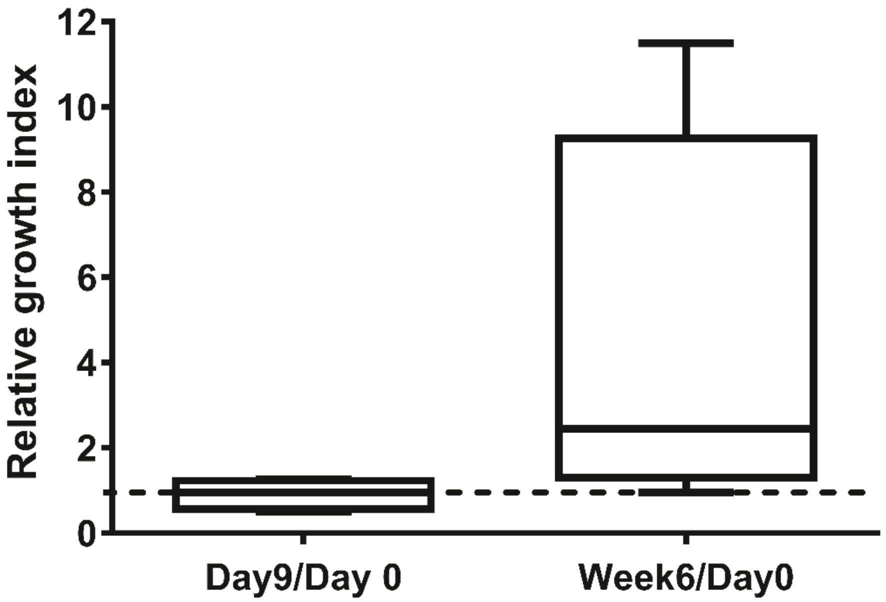

Fig. 3.S4. MRCS-CD unable to attenuate cancer growth in the absence of 5-FC in vivo

Six weeks after Luc-RFP-231 were seeded i.v. into nude mice, 10^6 MRCS-CD were administered systemically into tumor-bearing mice without 5-FC injection. In vivo luciferase activity was measured at different time points [before (Day 0), 9 days (Day 9) and 6 weeks (Week 6) after MRCS infusion]. Relative Metastasis Index (RMI) = luciferase read on Day 9 or Week 6 (after) / luciferase read on Day 0 (before). *n* = 4 for each group. The data are shown as box and whisker plots, with the box indicating 25% to 75% percentiles and the center line being the median. The error bars on either side indicate min and max of the data set.

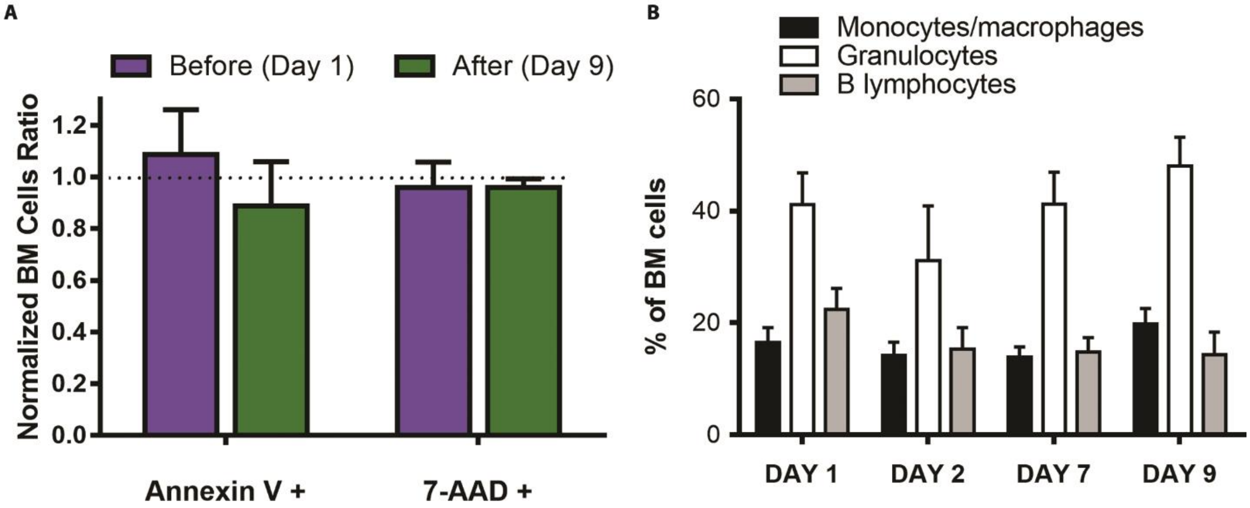

Fig. 3.S5. No detectable side effects in bone marrow cell populations after systemic treatment with MRCS-CD

(**A**) Luc-RFP-231 tumor-bearing and tumor-free nude mice treated by MRCS-CD were sacrificed before (Day 1) or after (Day 9) 5-FC injections. Bones were harvested, and bone marrow (BM) was flushed and stained with Annexin V and 7-AAD for FACS assay. Normalized BM cells = BM cells treated with MRCS-CD / BM cells treated with native MSCs, thus if ratio = 1, it would meant that MRCS-CD cause similar damage to the BM as native MSCs. (**B**) FACS assay shows no significant difference in bone marrow cell population during MRCS-CD treatment in the presence of 5-FC (Day 1, Day 2, Day 7, and Day 9 as indicated). Triplicate samples were used for the analysis. Data shown as mean ± SD.

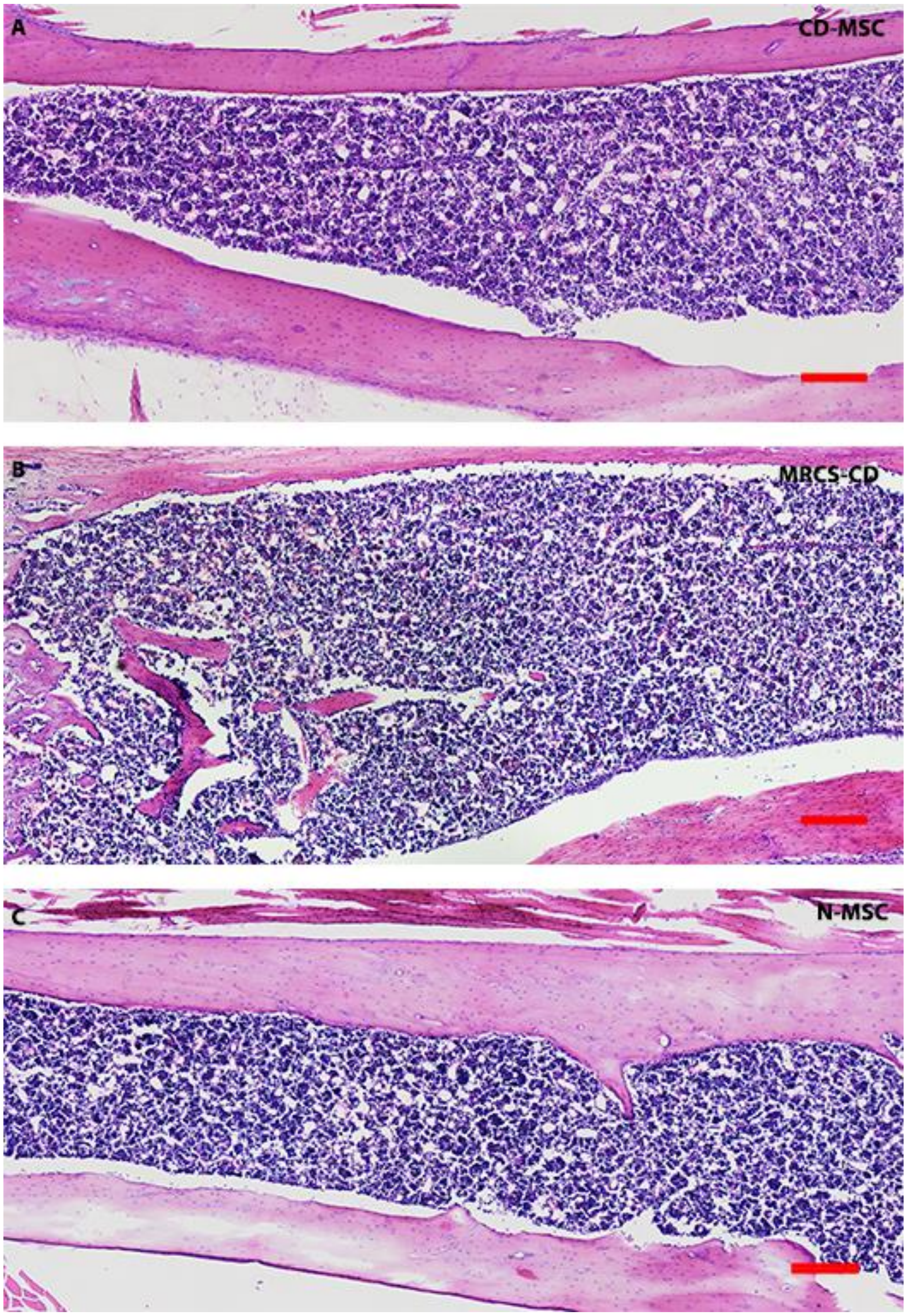

Fig. 3.*S6*. MRCS-CD causing no detectable side effects in vivo in bone marrow

Representative images of sectioned bones with H&E staining indicate no detectable tissue damage in bone marrow of tumor-bearing mice treated with (**A**) CD-MSC, (**B**) MRCS-CD, or (**C**) native MSCs, accompanied by 5-FC treatment. Scale bar = 200 μm.

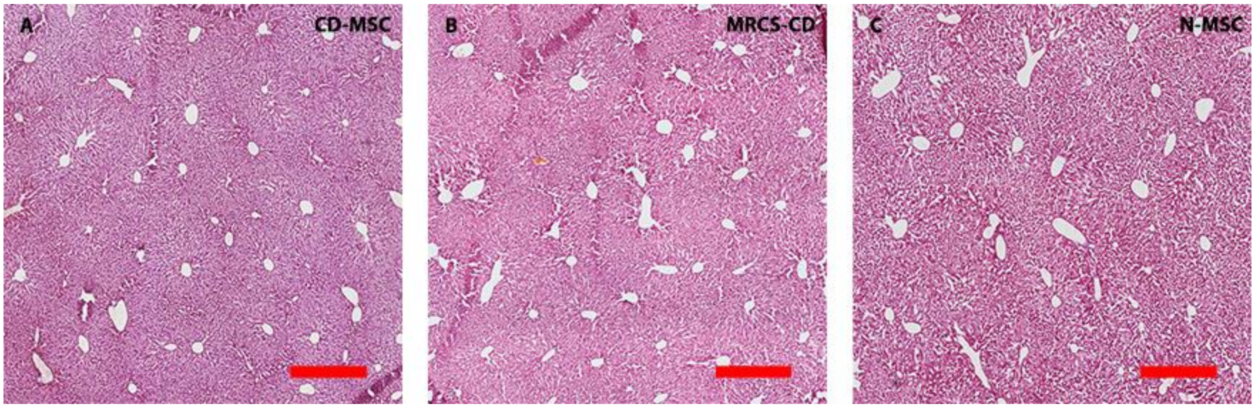

Fig. 3.S7. MRCS-CD causing no detectable side effects in vivo in livers

Representative images of sectioned livers with H&E staining indicate no detectable tissue damage in livers of tumor-bearing mice treated with (**A**) CD-MSC, (**B**) MRCS-CD, or (**C**) native MSCs, accompanied by 5-FC treatment. Scale bar = 200 μm.

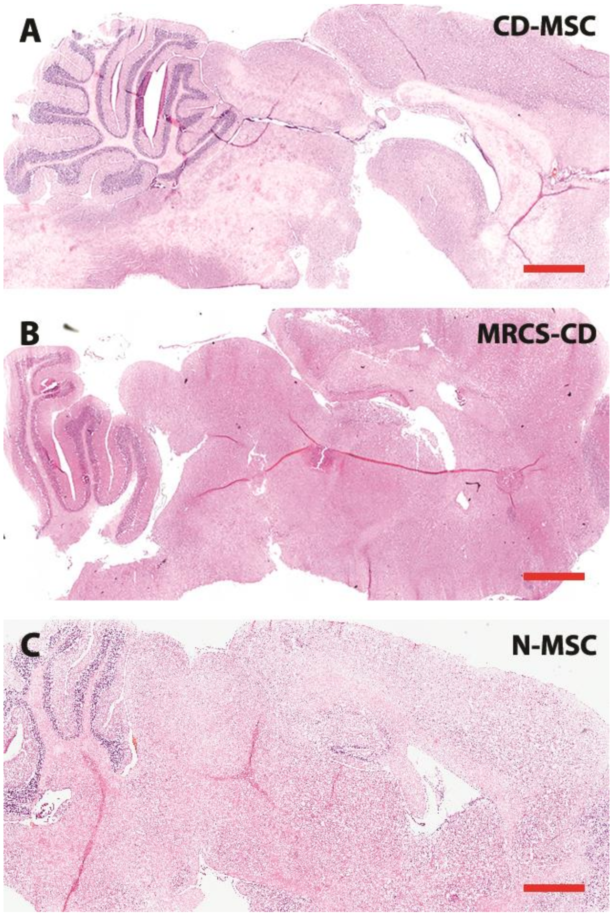

Fig. 3.S8. MRCS-CD causing no detectable side effects in vivo in brains

Representative images of sectioned brains with H&E staining indicate no detectable tissue damage in brains of tumor-bearing mice treated with (**A**) CD-MSC, (**B**) MRCS-CD, or (**C**) native MSCs, accompanied by 5-FC treatment. Scale bar = 200 μm.

3.9 References

1. Wong, C.C., et al., *Hypoxia-inducible factor 1 is a master regulator of breast cancer metastatic niche formation.* Proc Natl Acad Sci U S A, 2011. **108**(39): p. 16369-74.
2. Fidler, I.J., *Rationale and methods for the use of nude mice to study the biology and therapy of human cancer metastasis.* Cancer Metastasis Rev, 1986. **5**(1): p. 29-49.
3. Xie, X., et al., *Comparative studies between nude and scid mice on the growth and metastatic behavior of xenografted human tumors.* Clin Exp Metastasis, 1992. **10**(3): p. 201-10.
4. Kidd, S., et al., *Direct evidence of mesenchymal stem cell tropism for tumor and wounding microenvironments using in vivo bioluminescent imaging.* Stem Cells, 2009. **27**(10): p. 2614-23.
5. Reagan, M.R. and D.L. Kaplan, *Concise review: Mesenchymal stem cell tumor-homing: detection methods in disease model systems.* Stem Cells, 2011. **29**(6): p. 920-7.
6. Liu, L., et al., *Exogenous marker-engineered mesenchymal stem cells detect cancer and metastases in a simple blood assay.* Stem Cell Res Ther, 2015. **6**: p. 181.
7. Aboody, K.S., et al., *Neural stem cell-mediated enzyme/prodrug therapy for glioma: preclinical studies.* Sci Transl Med, 2013. **5**(184): p. 184ra59.
8. Sos, M.L., et al., *Predicting drug susceptibility of non-small cell lung cancers based on genetic lesions.* J Clin Invest, 2009. **119**(6): p. 1727-40.
9. Karp, J.M. and G.S. Leng Teo, *Mesenchymal stem cell homing: the devil is in the details.* Cell Stem Cell, 2009. **4**(3): p. 206-16.
10. Shaikh, A., et al., *Delineating the effects of 5-fluorouracil and follicle-stimulating hormone on mouse bone marrow stem/progenitor cells.* Stem cell research & therapy, 2016. **7**(1): p. 59.
11. Engler, A.J., et al., *Matrix elasticity directs stem cell lineage specification.* Cell, 2006. **126**(4): p. 677-89.
12. Huebsch, N., et al., *Matrix elasticity of void-forming hydrogels controls transplanted-stem-cell-mediated bone formation.* Nat Mater, 2015. **14**(12): p. 1269-77.
13. Ankrum, J. and J.M. Karp, *Mesenchymal stem cell therapy: Two steps forward, one step back.* Trends Mol Med, 2010. **16**(5): p. 203-9.
14. Yang, C., et al., *Mechanical memory and dosing influence stem cell fate.* Nat Mater, 2014. **13**(6): p. 645-52.
15. Liu, L., et al., *Exogenous marker-engineered mesenchymal stem cells detect cancer and metastases in a simple blood assay.* Stem Cell Res Ther, 2015. **6**(1): p. 181.
16. Bianchini, P. and A. Diaspro, *Three-dimensional (3D) backward and forward second harmonic generation (SHG) microscopy of biological tissues.* J Biophotonics, 2008. **1**(6): p. 443-50.
17. Campagnola, P.J., et al., *Three-dimensional high-resolution second-harmonic generation imaging of endogenous structural proteins in biological tissues.* Biophys J, 2002. **82**(1 Pt 1): p. 493-508.
18. Altendorf, H., et al., *Imaging and 3D morphological analysis of collagen fibrils.* J Microsc, 2012. **247**(2): p. 161-75.
19. Liu, F. and D.J. Tschumperlin, *Micro-mechanical characterization of lung tissue using atomic force microscopy.* J Vis Exp, 2011(54).

20. Plodinec, M., et al., *The nanomechanical signature of breast cancer.* Nat Nanotechnol, 2012. **7**(11): p. 757-65.

CHAPTER 4:
MRCS MECHANISM OF ACTION

Authors: Linan Liu[1-6]† , **Shirley X. Zhang**[1-6]†, Wenbin Liao[1-6], Henry P. Farhoodi[1-6], Chi W. Wong[1-6], Claire C. Chen[1-6], Aude I. Ségaliny[1-6], Jenu V. Chacko[5], Lily P. Nguyen[1-6], Mengrou Lu[1-6], George Polovin[1-6], Egest J. Pone[1-6], Timothy L. Downing[1,5], Devon A. Lawson[1,3,7], Michelle A. Digman[5,8,9], Weian Zhao[1-6]

Affiliations:

[1]Sue and Bill Gross Stem Cell Research Center, 845 Health Sciences Road, University of California-Irvine, Irvine, California, 92697, USA.

[2]Department of Pharmaceutical Sciences, University of California-Irvine, Irvine, California, 92697, USA.

[3]Chao Family Comprehensive Cancer Center, University of California-Irvine, Irvine, California, 92697, USA.

[4]Edwards Life Sciences Center for Advanced Cardiovascular Technology, University of California-Irvine, Irvine, California, 92697, USA.

[5]Department of Biomedical Engineering, University of California-Irvine, Irvine, California, 92697, USA.

[6]Department of Biological Chemistry, University of California-Irvine, Irvine, California, 92697, USA.

[7]Department of Physiology & Biophysics, University of California-Irvine, Irvine, California, 92697, USA.

[8]Laboratory for Fluorescence Dynamics, University of California-Irvine, California 92697, USA.

[9]Centre for Bioactive Discovery in Health and Ageing, School of Science and Technology, University of New England, Armidale, New South Wales 2351, Australia.

† These authors contributed equally to this work.

4.1 Introduction

After showing therapeutic efficacy of MRCS in a murine tumor model, we then verify the proposed mechanism of action by characterizing the tumor microenvironment and the activation of the engineered cells specifically within the cancer niche. Although we have previously shown that off-target deleterious side effects were low in comparison to constitutive controls, here we show that MRCS activation and cell death triggered by CD is specifically localized to stiffer, more crosslinked tumor regions of lung tissues.

4.2 Characterization of Biophysical Cues in Metastasis

Secretion of LOX by primary breast tumor increases the linearization and crosslinking of collagen at the metastatic niche, resulting in increased matrix stiffness [1]. Therefore, collagen linearization and crosslinking are robust surrogate markers of matrix stiffness. In addition, exogenous MSCs recruited to the metastatic lung assume an osteogenic differentiation profile not observed in the normal lung [2], although whether this is mediated by matrix stiffness is unclear. To mechanistically elucidate the activation and function of MRCS in the metastatic niche in vivo, we first validated the correlation between LOX expression and collagen expression in metastatic tissues. Upregulation of LOX expression was observed in tumor-bearing lungs (Day 0) compared to that in tumor-free lungs, and it correlated with the location of tumor cells (fig. 4.S1 and fig. 4.S2, A and B). Tumor-bearing lungs (Day 0) had higher collagen expression than tumor-free lungs by Masson's trichrome staining (fig. 4.S2, C and D), which is consistent with a previous study [3]. To further explore the correlation between collagen crosslinking and the metastatic niche, we performed second harmonic generation (SHG) imaging to co-localize collagen and lung metastases. SHG microscopy is a powerful modality for imaging collagen fibers (fibrillar network and linearization) in the tissue environment with high specificity [4]. With SHG imaging, high collagen expression was observed to co-localize with cancer metastasis (fig. 4.S2, A and B and fig. 4.S3) and LOX expression (Day 0, fig. 4.S2, A and B). We also observed that the collagen networks are significantly ($P < 0.0001$) more linearized in cancer-specific regions of tumor-bearing lungs than in non-cancer regions of tumor-bearing lungs and tumor-free lungs (Day 0, Fig. 4.1, A to D and fig. 4.S3, A to F), which indicates that the metastatic niches in the lungs have a distinctive mechano-microenvironment. Tumor-bearing lungs (Day 0) were also confirmed to have higher stiffness compared to tumor-free lungs by atomic force microscopy (AFM) (Fig. 4.1, E to H). Results from AFM microindentation of tissue sections showed that, besides having higher overall Young's modulus (17.68 ± 25.63 kPa), tumor-bearing lungs are more heterogeneous in stiffness as compared to tumor-free lungs that were less stiff (1.61 ± 3.97 kPa) (Fig. 4.1, G and H). Together, this set of data suggests a strong correlation between metastasis, LOX expression, increased collagen expression/crosslinking/linearization, and increased stiffness at the metastatic sites.

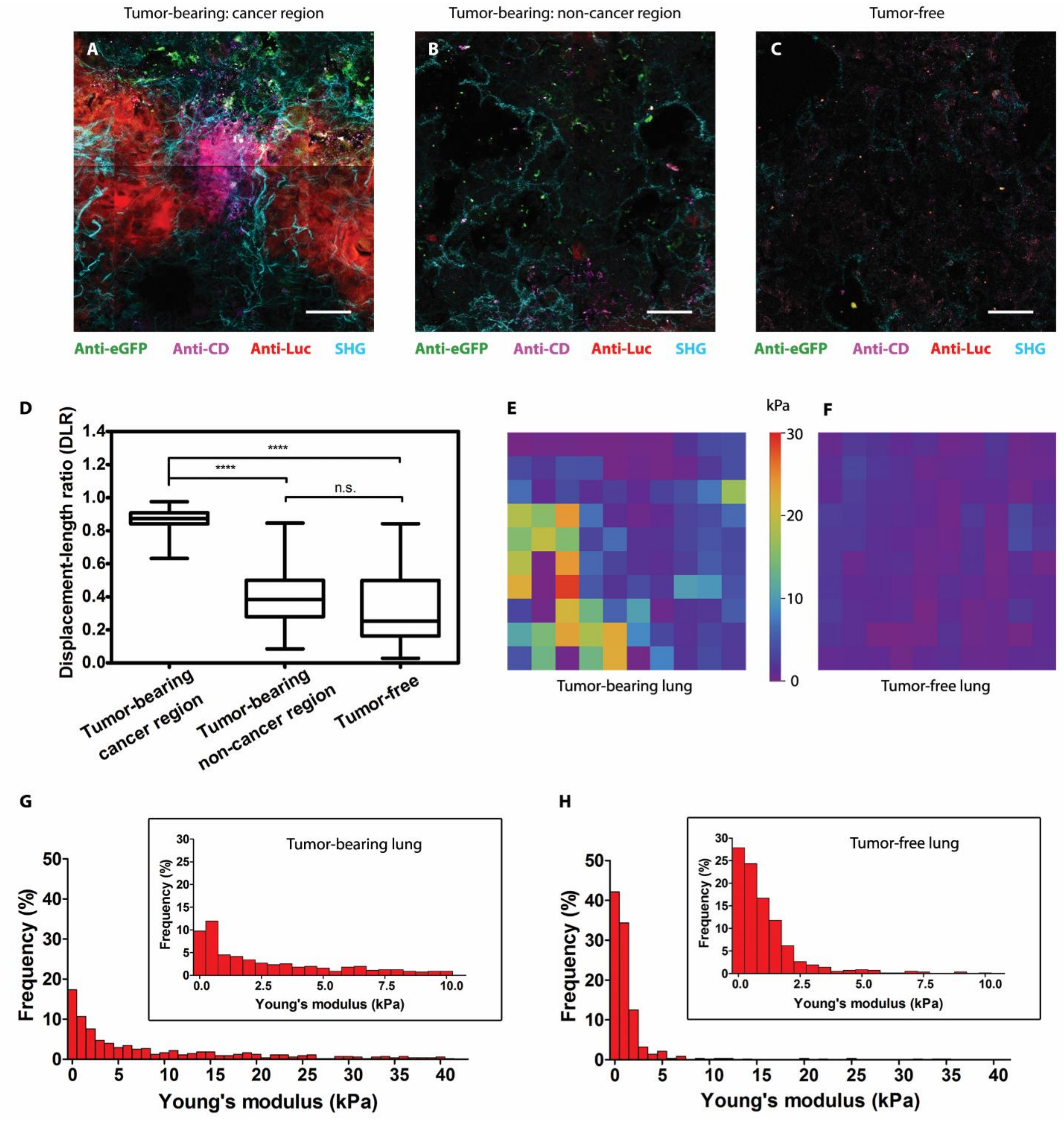

Fig. 4.1. Specific activation of MRCS in response to mechano-cues in the metastatic niche in vivo

(**A** to **C**) Frozen sections of lungs of Luc-RFP-231 tumor-bearing NSG mice (cancer region in **A** and non-cancer region in **B**) and tumor-free NSG mice (**C**) sacrificed 24 hours after infusion of MRCS-CD cotransfected with eGFP were stained with anti-Luc (red) to detect lung metastasis, anti-CD (magenta) for CD expressed by MRCS-CD, and anti-eGFP (green) for MRCS-CD tracking. Second harmonic generation (SHG) imaging of collagen networks (cyan) was also overlaid on IHC imaging. Scale bar = 50 μm. Multiple images were tiled into a larger composite image. Each representative picture was then extracted from the tiled image. (**D**) Quantification of collagen linearization using displacement to length ratio (DLR) of collagen fibers in SHG images. For a line, DLR = 1, and for a curve, DLR < 1. Representative images are in fig. S20. 45 fibers per group were used for this analysis. Box and whisker plot shown as min, 25th percentile, median, 75th percentile, max. n.s., not significant. *****P* < 0.0001. (**E** and **F**) Representative Atomic Force Microscopy (AFM) stiffness maps (50 μm x 50 μm) of tumor-bearing (**E**) and tumor-free (**F**) lungs. (**G** and **H**) display the frequency of Young's Modulus values of tumor-bearing (**G**) and tumor-free (**H**) lungs from AFM micro-indentation in the range 0 ~ 40 kPa (bin size = 1 kPa), whereas the inset graphs show the frequency within the range 0 ~10 kPa (bin size = 0.5 kPa). 500 measurements per group were analyzed. ****P* < 0.001 (Young's Modulus of tumor-bearing lungs vs. tumor-free lungs).

4.3 Specific Activation of MRCS in Response to Biophysical Cues

In order to further study how our MRCS interacts with the metastatic niche, we co-transduced the MRCS-CD to constitutively express eGFP as a cell tracker. We then performed SHG imaging with ex vivo IHC staining 24 hours after the systemic infusion of MRCS to tumor-bearing (Fig. 4.1, A and B) and tumor-free (Fig. 4.1C) mice (Day 1). As observed on the

SHG-IHC overlaid images, more MRCS (characterized by the constitutively expressed eGFP) was observed in tumor-bearing lungs. CD of eGFP-labeled MRCS-CD was preferentially activated in the cancer regions that are associated with more linearized collagen crosslinking (Fig. 4.1A). By contrast, few MRCS-CD were activated to express CD in less linearized non-cancer regions (Fig. 4.1B) or in tumor-free lungs (Fig. 4.1C). Additionally, in Fig. 4.1A, although MRCS-CD was recruited to tumor regions, but CD expression (magenta) was limited to direct contact with cancer (red) and crosslinking (cyan). The MRCS-CD in the periphery of the tumor region did not express CD, but only the constitutive eGFP (green). Separate images for each color layer are shown in fig. 4.S4. With MRCS-CD, the apoptosis (visualized via PARP p85 antibody staining) is correlated with the presence of cancer and increased crosslinked collagen (fig. 4.S5). With CD-MSC, there is apoptosis regardless of the tissue environment, and PARP signals are present in highly cancerous and crosslinked regions (fig. 4.S6A), but also in less crosslinked regions (fig. 4.S6B) and in healthy controls (fig. 4.S6C).

To demonstrate the translatability and broad applicability of our MRCS platform, we also evaluated MRCS in a spontaneous model of breast cancer metastasis to the lungs. The establishment of the spontaneous model is shown in fig. 4.S7, demonstrating that lung metastasis occurs within about 6 weeks after implantation of cancer cells to the mouse fat pads. We then demonstrated that MRCS-CD can specifically target cancer regions (RFP) with higher tissue collagen crosslinking (SHG) and induce specific tissue damage (apoptosis via PARP p85 staining) in the metastatic niches in vivo (Fig. 4.2A). In contrast, we observed minimal off-target damage in non-cancer regions of tumor-bearing lungs (Fig. 4.2B and fig. 4.S8) or in healthy lungs (Fig. 4.2C and fig. 4.S8) where there is low crosslinking compared to the cancer regions of the lungs.

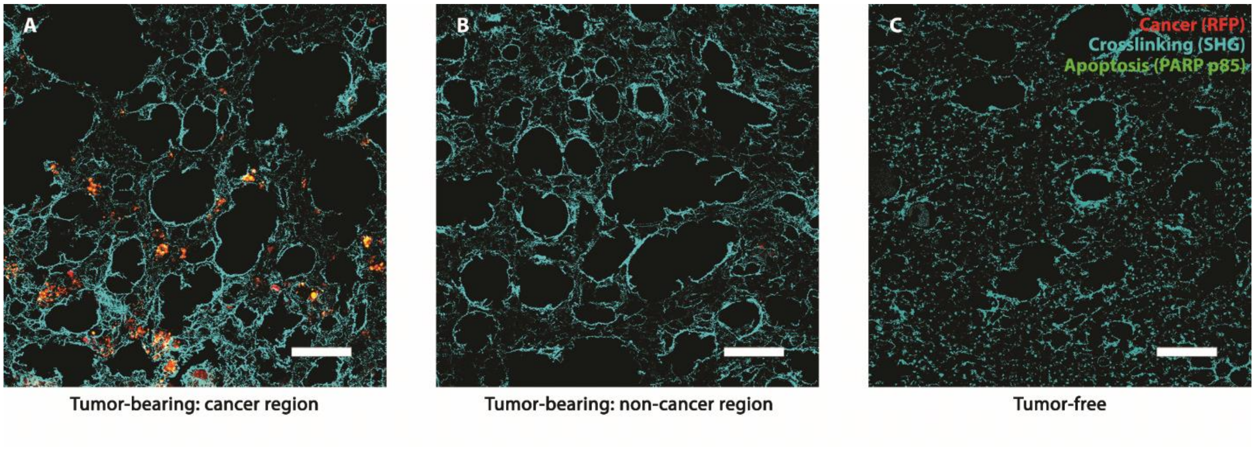

Fig. 4.2. Crosslinking-specific tissue damage by MRCS in response to mechano-cues in the metastatic niche in vivo in spontaneous lung metastasis model

Frozen sections of lungs of tumor-bearing NSG mice with Luc-RFP-231 spontaneous lung metastasis from primary tumors (cancer region in **A** and non-cancer region in **B**) and tumor-free NSG mice (**C**) sacrificed after MRCS-CD infusion and 5-FC treatment as indicated (Day 9) were stained with anti-PARP p85 (green) for tissue apoptosis. RFP signal (red) indicates the presence of lung metastasis, and co-localization of red and green appears yellow. SHG imaging of collagen networks (cyan) was presented and overlaid with IHC imaging. Scale bar = 100 µm.

4.4 Discussion

Despite decades of effort, little progress has been made to improve the diagnosis and treatment of cancer metastases. In particular, due to the heterogeneity of cancer and its ability to develop resistance to current treatments that target biochemical markers, new targeting strategies are urgently needed. Inspired by the tight correlation between increases in tissue stiffness and breast cancer metastatic niches found in recent studies [1, 3-6] and the fact that MSCs differentiate to specific lineages depending on the stiffness of the microenvironment [7], we have developed a class of cancer therapeutics that directly target the mechanoenvironmental cues of cancer metastases. The MRCS is an attempt to directly interrogate the mechano-niche in vivo and apply it for localized delivery of agents including imaging reporters and therapeutics.

Mechano-niches play vital roles in development, homeostasis, and disease progression, including many types of cancer, and therefore serve as an emerging target for next generation therapeutics [8, 9]. In particular, matrix stiffness is an appealing target for cancer therapeutics due to its long persistence in the body (measured in years), making it refractory to development of resistance to treatments [10, 11]. Furthermore, cancer and cancer biomarkers are highly heterogeneous within the population, making it difficult to develop treatments that can accurately target the disease. Mechanical markers such as matrix stiffness, however, manifest similarly in most cases and present a more universal target for therapeutics [8, 12]. Given the enormous challenge in the search of specific cancer biomarkers, matrix stiffness may present an opportunity, especially when used in combination with chemical biomarkers, to improve the sensitivity and specificity in cancer targeting. In addition, the natural ability of MRCS to actively home to and integrate into tumors and metastases enables the efficient delivery of therapeutics to the target site. Together, our MRCS system could have major clinical implications in increasing the effectiveness of therapies for patients with metastatic cancer while also ameliorating the deleterious side effects associated with chemotherapy [13] or other, less specific cell-based delivery systems that are engineered to constitutively express therapeutics. In addition, our system could potentially be used to prevent metastasis by targeting the LOX-mediated, stiff pre-metastatic niche [1, 3, 4], for example by engineering the MRCS to secrete matrix remodeling enzymes, such as metalloproteases, to reduce the stiffness of the niche.

MSCs have been proven safe for transplantation into humans in the clinic [14, 15], which paves the way for clinical translation of the proposed MRCS. Transplanted MSCs themselves have previously been proposed to regulate cancer progression, both positively and negatively [16-18]. We do not consider it as a major issue because MRCS only stay in tumors transiently (< 7 days) and would be eliminated by suicide genes (CD). Our data show that MRCS can continue to functionally convert 5-FC to 5-FU for at least 5 days while in contact with stiff substrate, though the process of cancer killing could begin as early as 2 days after treatment, with the MRCS-CD themselves dying shortly after. This suggests that MRCS can be a transient yet efficient drug delivery system for treating cancer. Future studies will need to further investigate the activity of both CD-MSC and MRCS-CD in vivo, in particular with regards to conversion of 5-FC, to determine the time points of conversion and killing of the drug source (MSCs) as well as dosages required to ensure efficacy while still minimizing side effects.

Our approach to targeting the mechano-niche in vivo by MRCS may also be relevant for the treatment of other types of fibrotic diseases through, for example, delivery of metalloproteases. Moreover, by using cells engineered to respond to variations in matrix stiffness to drive expression of diagnostic reporters (such as the *HSV-1-tk* gene coupled with positron emission tomography imaging [19]), the MRCS could also be used to detect micrometastases at a higher resolution than current imaging techniques. Our system potentially has major advantages over current methods of identifying micrometastases in that it can amplify the signal from smaller numbers of cells by detecting the properties of the local microenvironment, and that it can be used in vivo without a need for biopsy or other invasive techniques. Finally, our MRCS could also serve as an approach to elucidate mechanobiology, specifically the interplay of biomechanical cues [20] with cells in their native environment in vivo in the context of cancer and other conditions such as inflammation and injury. It is also important to note that MRCS is not restricted to lung metastasis of breast cancer, although that was the focus of this study due to its high morbidity and its robustness as a model to test our hypothesis. However, future studies using other models of metastasis, especially in sites other than the lung, will need to be investigated to evaluate the broad applicability of our approach. Although previous studies have established that matrix stiffness is tightly linked to invasiveness and metastasis, current methods of measuring stiffness rely on elastography or ex vivo measurements with AFM or compression devices [4, 8]. Unfortunately, these techniques lack the resolution to directly measure the stiffness of the ECM with which the cells interact; instead, they measure the average stiffness of larger regions encompassing both ECM and cellular components of the tissues of interest. A cell-based stiffness sensor should reveal what cells actually “feel” in the microenvironment and dynamically interrogate the mechano-environment of primary tumors, metastases, and changes in matrix stiffness during disease progression and response to therapies at a cellular resolution in vivo.

4.5 Materials and Methods

Breast cancer lung metastasis animal models

0.5 x 10^6 (2.5 x 10^6/ml in Dulbecco's Phosphate-Buffered Saline (DPBS, Lonza)) LV-*CMV*::Luc-RFP MDA-MB-231 (Luc-RFP-231), or LV-*CMV*::eGFP MDA-MB-231 (eGFP-231) breast cancer cells were infused intravenously (*i.v.*) into immunocompromised female nude mice (8 weeks, #088, Charles River Laboratories) or NOD-SCID gamma (NSG) mice (8 weeks, #005557, The Jackson Laboratory). For the spontaneous metastasis model, 1 x 10^6 Luc-RFP-231 cells in Matrigel were implanted subcutaneously (*s.c.*) into the fat pads of female NSG mice (8 weeks). All animals injected with cancer cells or DPBS as healthy controls were picked randomly. All animal experiments and procedures were performed after the approval from the University of California Irvine (UCI) Institution of Animal Care and Use Committee (IACUC protocol number 2012-3062) and conducted according to the Animal Welfare Assurance (#A3416.01).

MSC transplantation and prodrug treatment

Four (NSG *i.v.* model) or six (nude *i.v.* model or NSG *s.c.* model) weeks after Luc-RFP-231 cell transplantation, 1 x 10^6 LV-*CMV*::eGFP MSCs co-transduced with MRCS-CD (eGFP-MRCS-CD), LV-MRCS-eGFP MSCs (MRCS-eGFP), CD-MSC, MRCS-CD, N-MSC (5 x 10^6 /ml in DPBS), or DPBS were *i.v.* infused into the mice harboring breast cancer cells and into tumor-free control mice (Day 0) through the tail vein. For second harmonic generation (SHG) imaging and immunohistochemistry (IHC) (ex vivo), animals infused with eGFP-MRCS-CD or MRCS-eGFP were euthanized *(n* = 3 for each group) 24 hours later (Day 1) and lungs were harvested. For the cancer treatment experiment, Luc-RFP-231 tumor-bearing or tumor-free mice infused with CD-MSC, MRCS-CD, N-MSC, or DPBS were intraperitoneally (*i.p.*) treated with 5-FC (500 mg/kg in DPBS) for 7 days (two doses/day for Day 1-Day 5 and one dose/day for Day 6-Day 7). Representative mice (*n* = 3 for each group) were euthanized on Day 1 and Day 9 for ex vivo assays. For the survival experiment, the endpoint for mice was defined as "found dead" or euthanasia criteria stated in UCI IACUC protocol 2012-3062. For the survival experiment, the endpoint for mice was defined as "found dead" or euthanasia criteria stated in UCI IACUC protocol 2012-3062: that is, a condition scoring system was used to monitor if the mouse has body weight loss (0 to 3), abnormalities on physical appearance (0 to 3), unprovoked behavior (0 to 3), and/or abnormal behavioral responses to external stimuli (0 to 3), with 0 being healthy. Any mouse was to be euthanized if 1) the total score was ≥ 5 or 2) it scored a "3" for any variable regardless of the total score.

In vivo and ex vivo bioluminescence imaging

Four (NSG *i.v.* model) or six (nude *i.v.* model or NSG *s.c.* model) weeks after Luc-RFP-231 cell transplantation, in vivo Luc activity from Luc-RFP-231 cells was measured (Day 0) as previously described [21]. Briefly, in vivo Luc signal was imaged with IVIS Lumina (Caliper LifeSciences) 10 minutes after intraperitoneal (*i.p.*) injection of D-luciferin (150 mg/kg in DPBS) into mice. Mice were anesthetized with 2-3% of isoflurane (Western Medical Supply), and in vivo Luc activity was measured at the indicated time points. Before cancer treatment, nude mice with Luc signals in the lungs were imaged and grouped randomly. Minimal adjustment was performed to keep the differences between "week 0" groups (red spots) not statistically significant. After the cancer treatment experiments, in vivo Luc activity from Luc-RFP-231 cells was measured on Day 9 and 6 weeks after treatment.

Four (NSG) or six (nude) weeks after eGFP-231 cell transplantation, 1 x 10^6 Luc-MSC, MRCS-Luc, N-MSC (5 x 10^6 /ml in DPBS), or DPBS were systemically infused into the mice harboring breast cancer cells and into tumor-free control mice (Day 0). In vivo Luc activity was measured at the indicated time points.

Six weeks after *s.c.* Luc-RFP-231 cell transplantation, mice were sacrificed and lungs were harvested. 150 µg/ml D-luciferin was added onto the lungs, and ex vivo Luc activity from Luc-RFP-231 cells in the lungs was measured with IVIS Lumina.

Tissue processing, histology, and TUNEL assays

Lungs, livers, and brains were collected from tumor-bearing or tumor-free nude mice (Day 0 or Day 9). After overnight fixation in 4% PFA, followed by overnight incubation in 30% sucrose solution (Amresco), samples were flash frozen in Tissue-Tek O.C.T Compound (Sakura Finetek). Frozen sections 8 µm thick were taken using a Reichert-Jung Cryocut 1800 microtome (Leica Instruments) onto UltraClear positively charged slides (Denville, 25 x 75 x 1 mm). Bones were fixed overnight in 4% PFA, then decalcified for 10 days in a 14% EDTA solution with 0.2% PFA in PBS before embedding in paraffin and sectioning with a Leica microtome.

Masson's trichrome staining was performed to assess extent of tissue crosslinking and fibrosis (Day 0). Slides were fixed in Bouin's solution (Sigma) overnight at room temperature, then briefly rinsed in tap water before further washing in water on a shaker for 20 minutes. Slides were stained in a working solution of Weigert's hematoxylin (1: 1 ratio of solution A and solution B, Sigma) for 8 minutes and washed thoroughly in running tap water. Slides were then stained in Biebrich scarlet-acid fuchsin solution (Sigma) for 5 minutes and washed in water. Slides were differentiated in a 1: 1 phosphomolybdic-phosphotungstic acid solution (Sigma) for 5 minutes. Slides were then stained in aniline blue solution (Sigma) for 5 minutes and differentiated in a 1% acetic acid (Sigma) solution for 2 minutes. Finally, slides were rinsed in water, then dehydrated with a few dips each in 70%, 90%, and 100% ethanol and cleared for 1 minute in Histoclear (Thermo Fisher Scientific) before mounting with Permount (Thermo Fisher Scientific).

Terminal deoxynucleotidyl transferase dUTP nick end labeling (TUNEL) assay was performed to further assess tissue damage (Day 0 and Day 9). The ApoBrdU-IHC DNA Fragmentation Assay Kit (Biovision) was used with the included protocol. Data were analyzed with ImageJ (http://imagej.nih.gov/, NIH). For each picture, the areas of TUNEL-positive cells (stained brown, [T+]) and those of TUNEL-negative cells (stained blue, [T-]) were extracted with ImageJ. Then the percentage of TUNEL-positive cells was calculated as X = [T+] / ([T+] + [T-]) x 100%. 10 representative pictures per group were included in the analysis.

Hematoxylin and eosin (H&E) staining was performed to assess systemic tissue damage in lung, liver, brain, and bone. Slides were stained with Harris hematoxylin (Sigma) for 10 minutes, followed by acid alcohol (1% HCl in 70% ethanol), Scott's bluing reagent (Sigma) for 1 minute, and Eosin Y (Sigma) for 5 minutes. Slides were dehydrated and mounted as described above.

Ex vivo immunohistochemistry

Lung tissues were harvested from tumor-bearing or tumor-free nude or NSG mice (Day 0 for LOX staining, Day 1 for MRCS homing and activation, and Day 9 for Annexin V) and processed as mentioned above. Frozen slides (8 μm) were thawed and rehydrated in dH_2O for 5 minutes, then fixed in chilled acetone (Thermo Fisher Scientific) at -20°C for 10 minutes, permeabilized in 0.1% Triton X-100 for 10 minutes, and blocked in 0.1% Triton X-100 with 5% normal donkey serum for 1 hour. Primary antibodies (Table 1) were diluted 1: 100 from the stock solution and applied overnight at 4°C. Slides were washed in 1X PBS. Then, secondary antibodies (Table 2) were diluted 1: 500 from the stock solution and applied for 30 minutes at room temperature. Slides were stained for nuclei with DAPI (1 μg/ml), then washed in PBS and mounted with Fluoromount-G. Slides were imaged with Nikon Eclipse Ti inverted microscope.

Second Harmonic Generation (SHG) Imaging

For SHG imaging, frozen 40 μm sections of fixed (for LOX-SHG co-localization) or unfixed (for MRCS-SHG co-localization and SHG quantification), OCT-mounted mouse lungs (Day 0 for LOX-SHG co-localization and Day 1 for MRCS-SHG co-localization) were obtained as mentioned above and dried overnight, in the dark, at room temperature on slides. Slides were then prepared as described in the "Ex vivo Immunohistochemistry" session. The fluorescent signals from antibody-stained slides were imaged using a Zeiss LSM710 multiphoton/confocal microscope (Zeiss) with a 40x W1.2NA objective (Zeiss). Slides were sequentially imaged in order of increasing fluorescent wavelength to reduce photo bleaching. SHG was performed at an 840 nm excitation wavelength and narrow bandpass detection, with a spectral window of 420/20 nm [22-24]. Images were processed with ImageJ and Matlab (MathWorks Inc.). For MRCS-SHG co-localization and representative images for SHG quantification, multiple high quality pictures were generated per sample and tiled into a larger image, from which the representative pictures were selected. For SHG quantification, collagen fibers imaged by SHG were automatically or manually selected, and the ratio of displacement and length of the collagen fibers were analyzed and plotted. To minimize artifacts caused by collagen bundles close to blood vessels, the fibrillar length and curvature of collagen were extracted and adjusted by quasi-manual selection of fibrillar structures. CT-FIRE was used to automatically select and quantify the curvature of collagen fibers [25, 26]. Regions of the lung tissue defined as “cancer region” or “non-cancer region” were manually selected.

For SHG-PARP p85 co-localization, large lung tissue scans of fluorescent channels 594 nm (for cancer) and 640 nm (for PARP p85) were taken on a fluorescent microscope (Eclipse Ti-E, Nikon) with 7-color Spectra X Light Engine (Lumencor) and Zyla sCMOS camera (Andor) at 20x magnification. The sample was then scanned in the same approximate area using Zeiss LSM710. The SHG scan was then overlaid upon the fluorescent scan using ImageJ to get a high-definition fluorescence and SHG combined image for analysis. The overlaid large scans were then divided into sections using a grid of approximately 500 x 500 µm. Each section of the grid was treated as a separate data point for SHG-PARP p85 co-localization.

Bone marrow flushing and flow cytometry

1 day, 2 days, 7 days, or 9 days after MSC infusion with 5-FC treatment as mentioned above, nude or NSG mice were sacrificed, and bones, specifically femurs from both legs, were harvested, with muscle tissue removed carefully. Bone marrow was then flushed with PBS, dissociated, and filtered using a 70 µm cell strainer (Corning). The red blood cells were then

lysed using ammoniumchloride potassium buffer (Lonza) for 3 minutes at 37°C. The remaining cells were washed twice with PBS and diluted to 1 x 10^6 cells/ml. 300 µl of cells in suspension were then stained with either Annexin V-FITC (BioLegend) in Annexin V binding buffer (BioLegend) and 7-Aminoactinomycin D dye (7-AAD, Thermo Fisher Scientific) or anti-B220 APC (CD45R), anti-CD11b FITC, and anti-Gr-1-PE-Cy7 (Ly6G) (Table 1) according to the manufacturer's instructions. Compensation and unstained controls were also prepared for the analysis. For samples requiring multiple stains, a compensation coefficient was first estimated from controls using unstained cells or only a single stain and inputted into the analysis software to correct for fluorescent signal spillover from other channels. Finally, the cells were analyzed with a BD Accuri C6 flow cytometry machine (BD Biosciences). The different populations were analyzed as follows: monocytes/macrophages (CD11b$^+$, Gr-1$^{neg/low}$), granulocytes (CD11b$^+$, Gr-1^{high}), and B cells (B220^{low} and B220^{high}).

Atomic force microscopy (AFM)

Six weeks after *i.v.* infusion of Luc-RFP-231 cancer cells or DPBS administration for the tumor-free control, nude mice (Day 0) were euthanized and lungs were immediately harvested and kept in ice-cold Ringer solution (Thermo Fisher Scientific). All the AFM assays were performed within 48 hours after mouse euthanasia. Lung samples were cut into 500 µm-thick slices using a rat heart slicer matrix (Zivic Instruments) and mounted to a 60 mm plastic petri dish using epoxy glue (Devcon). Samples were measured using Bruker BioScope Catalyst Atomic Force/ Zeiss LSM5 Confocal Fluorescence Microscope (Bruker/ Zeiss) using contact mode in fluid with MLCT C Triangular cantilevers (spring constant = 0.01 N/m, Bruker). Data points were taken 5 µm apart on 50 x 50 µm scans. Data were analyzed with

Nanoscope Analysis v1.5 software, using a Sneddon conical model with Poisson ratio 0.4 [25, 26].

Study Design

This study was designed to investigate the hypothesis that a cell-based system can be engineered to respond specifically to mechanoenvironmental cues (MRCS) to target cancer metastases. In vitro experiments including tunable hydrogels, qPCR, co-cultures, and mass spectrometry, and in vivo and ex vivo experiments using nude and NSG mice, including luciferase imaging, antibody staining, SHG, and AFM, were performed to demonstrate that MRCS can sense and kill cancer cells in response to biophysical cues. For all in vitro studies except for mass spectrometry, three independent experiments with at least three samples per condition were performed. $n = 9$ for the in vivo cancer killing and survival assays. $n \geq 3$ for ex vivo characterization of the biophysical cues in the metastatic niche and the validation of MRCS. For the survival experiment, the endpoint for mice was defined as "found dead" or euthanasia criteria stated in UCI IACUC protocol 2012-3062 described in Supplementary Materials and Methods. Groups for animal experiments were randomized, except for the cancer killing study where manual group adjustments were performed to keep the differences in initial cancer burden between all "week 0" group animals not statistically significant. In vitro experiments were not blinded. In vivo and ex vivo experiments were blinded.

Statistical analysis

Data were analyzed by Student's *t* test when comparing 2 groups and by ANOVA when comparing more than 2 groups. Log-rank (Mantel-Cox) test was performed for animal survival data analysis by two-way ANOVA and Mann Whitney test was used for AFM data. Outliers in AFM data were removed by Grubb's test ($P < 0.05$). Data were expressed as mean ± SD or mean ± SEM. Two-sided testing with normal-based 95% confidence interval was performed for each analysis, and differences were considered significant at $P < 0.05$.

4.7 Acknowledgements and Author Contributions

Acknowledgments: We thank D.-K. Kang, M. M. Ali, and J. Zimak for discussion and comments. We are grateful to K. Zhang and X. E. Guo for kind help on *in vitro* experiments and discussion. We thank F. Grun, the director of the UCI Mass Spectrometry Facility (Department of Chemistry, University of California-Irvine) for his precious advice and help with the mass spectrometry training and analysis. We thank K. Aboody, T. Synold, and M. Metz from City of Hope for sharing their LC-MS/MS method for prodrug conversion. We thank C. Schmidt-Dannert, C. Contag, S. Piccolo, and D. Trono for the plasmids. We thank California NanoSystems Institute (CNSI) at University of California-Los Angeles for AFM.

Author contributions: L.L. designed and performed experiments, analyzed and interpreted data, drafted the manuscript, and coordinated the project. S.X.Z. performed the in vivo experiments, tissue processing, histology, mass spectrometry exams and AFM micro-indentation test, analyzed data and drafted the manuscript. W.L. designed and performed the in vivo experiments and edited the manuscript. H.P.F. performed tissue processing, immunohistochemistry, and SHG imaging and participated in the in vivo experiments. C.W.W. engineered the cells, conducted the immunocytochemistry, qPCR, XTT and transwell assays, in vitro luciferase assays, mass spectrometry exams, bone marrow flush, and flow cytometry, and analyzed the data. C.C.C. carried out the qPCR, XTT assays and in vitro luciferase assays, analyzed the data, and participated in the mass spectrometry exams. A.I.S. designed and performed the mass spectrometry exams, designed the histology assays, conducted the flow cytometry assay, and analyzed the data. J.V.C. and M.A.D. performed SHG imaging and edited the manuscript. L.P.N. participated in the in vivo experiments and the mass spectrometry exams, performed the histology assays, and acquired the data. M.L. engineered the cells, helped to prepare the figures, and performed cloning and manuscript editing. G.P. contributed to in vivo experiments and participated in immunohistochemistry and manuscript editing. T.L.D edited the manuscript. D.A.L. edited the manuscript. E.J.P. conducted the flow cytometry assay, edited the manuscript, and interpreted the data. W.Z. was responsible for conception and design of the research, interpreted the results, revised the manuscript, and supervised the overall project.

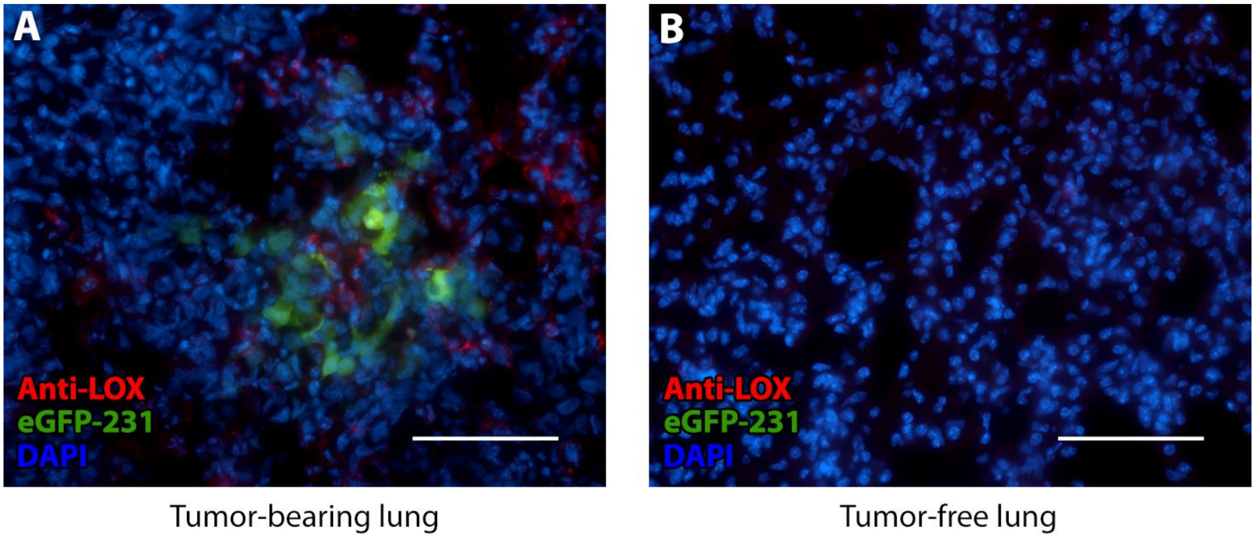

Tumor-bearing lung

Tumor-free lung

Fig. 4.S1. Upregulation and co-localization of lysyl oxidase (LOX) expression with tumor in tumor-bearing lungs

Representative frozen sections of lungs of (**A**) eGFP-231 tumor-bearing NSG mice and (**B**) tumor-free NSG mice sacrificed before MRCS infusion (Day 0) were stained with anti-LOX (red) and DAPI (blue). eGFP (green) indicates lung metastasis. Scale bar = 50 μm.

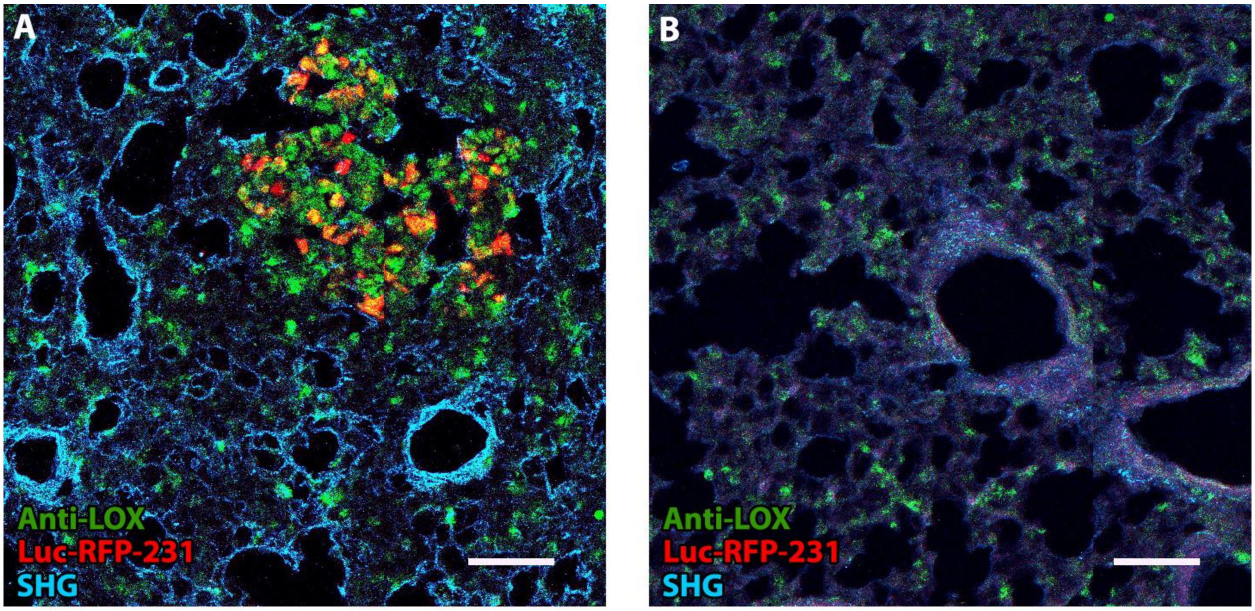

Tumor-bearing lung Tumor-free lung

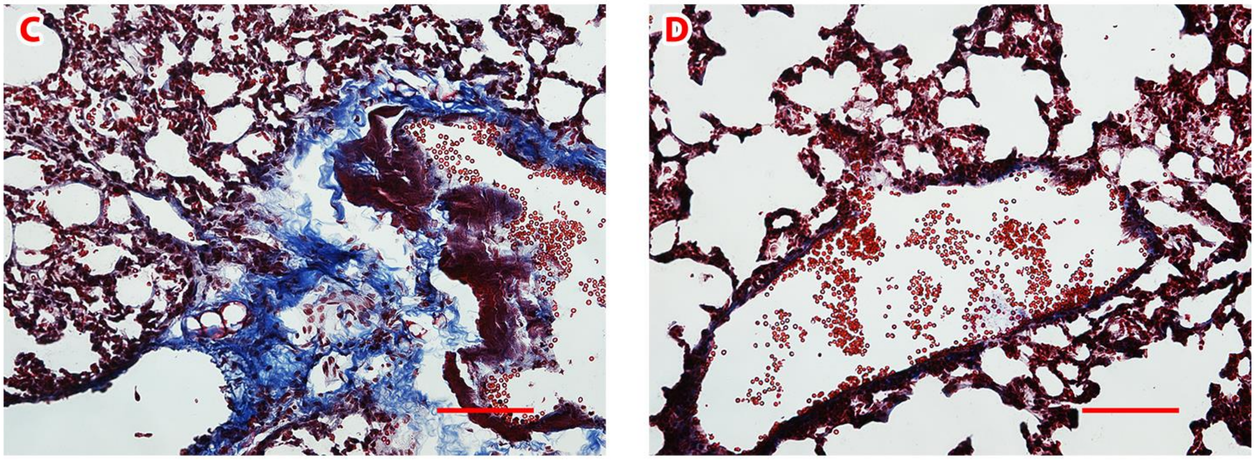

Tumor-bearing lung Tumor-free lung

Fig. 4.*S*2. **LOX expression upregulated with increased collagen expression in metastatic niche**

Representative frozen sections of lungs of (**A**) Luc-RFP-231 tumor-bearing NSG mice and (**B**) tumor-free NSG mice sacrificed before MRCS infusion, showing staining with anti-LOX (green), lung metastases (RFP, red), and SHG imaging of collagen networks (cyan). Scale bar = 100 μm. Trichrome staining on representative frozen sections of lungs from (**C**) tumor-bearing and (**D**) tumor-free mice shows the degree of collagen expression in the lungs of tumor-bearing and tumor-free nude mice. Scale bar = 100 µm.

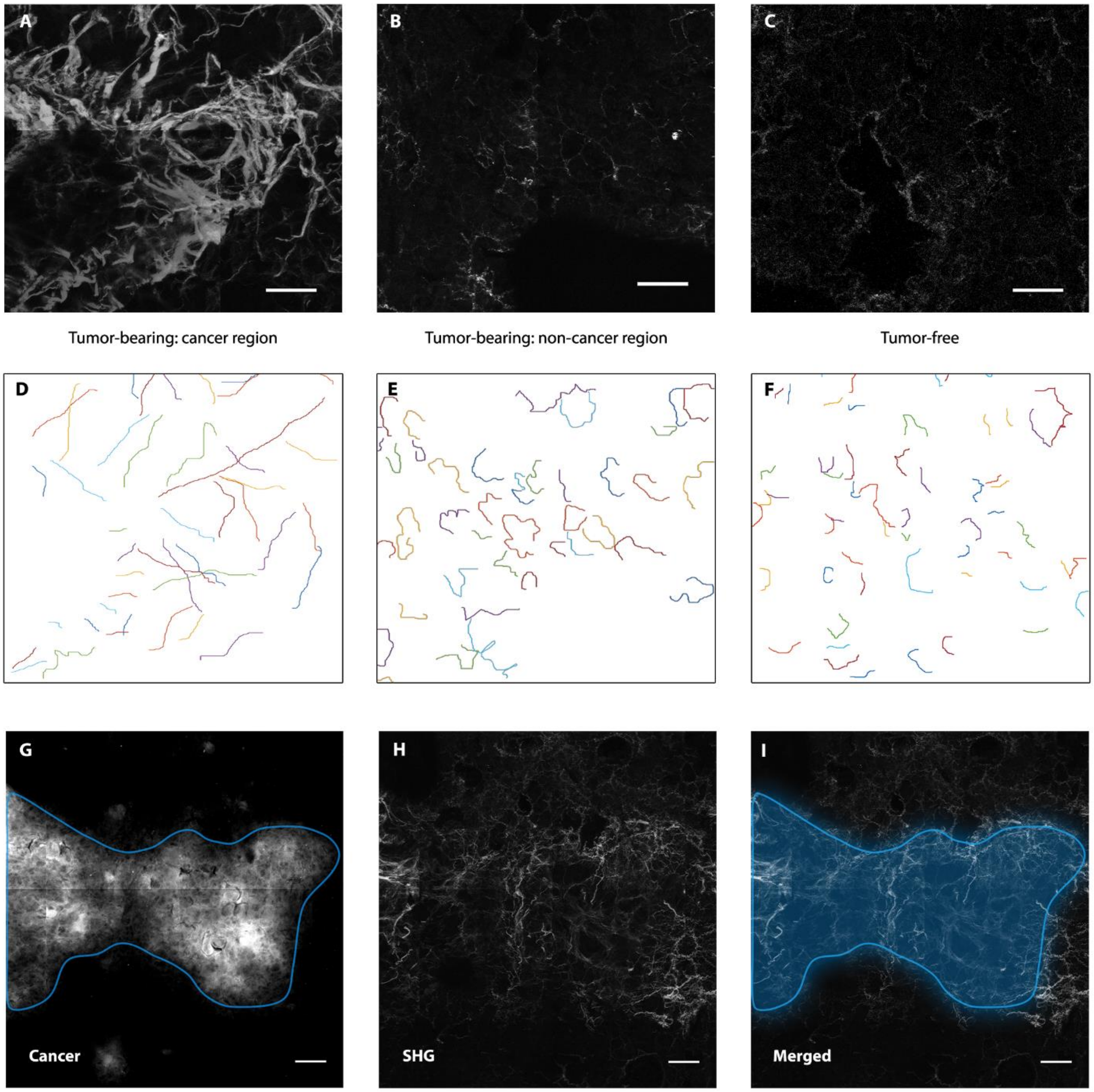

Fig. 4.S3. SHG imaging showing upregulated and more linearized collagen in tumor-bearing lungs

Representative SHG images of (**A**) cancer (Luc-RFP-231) region and (**B**) non-cancer region of tumor-bearing lungs as well as (**C**) tumor-free lungs of NSG mice show that collagen is upregulated and more linearized in cancer regions. Scale bar = 50 μm. (**D**, **E**, and **F**) are corresponding images of selected fibrillar structures of (**A**, **B**, and **C**), respectively. They were used for quantification of collagen linearization. (**G**) The regions of cancer expressing RFP were imaged with confocal microscopy and highlighted with a blue outline. (**H**) SHG imaging of the corresponding area of panel **G**. (**I**) Co-localization of cancer signal and collagen network by merging panels **G** and **H**. The highlighted areas are defined as “cancer regions.” Scale bar = 50 μm.

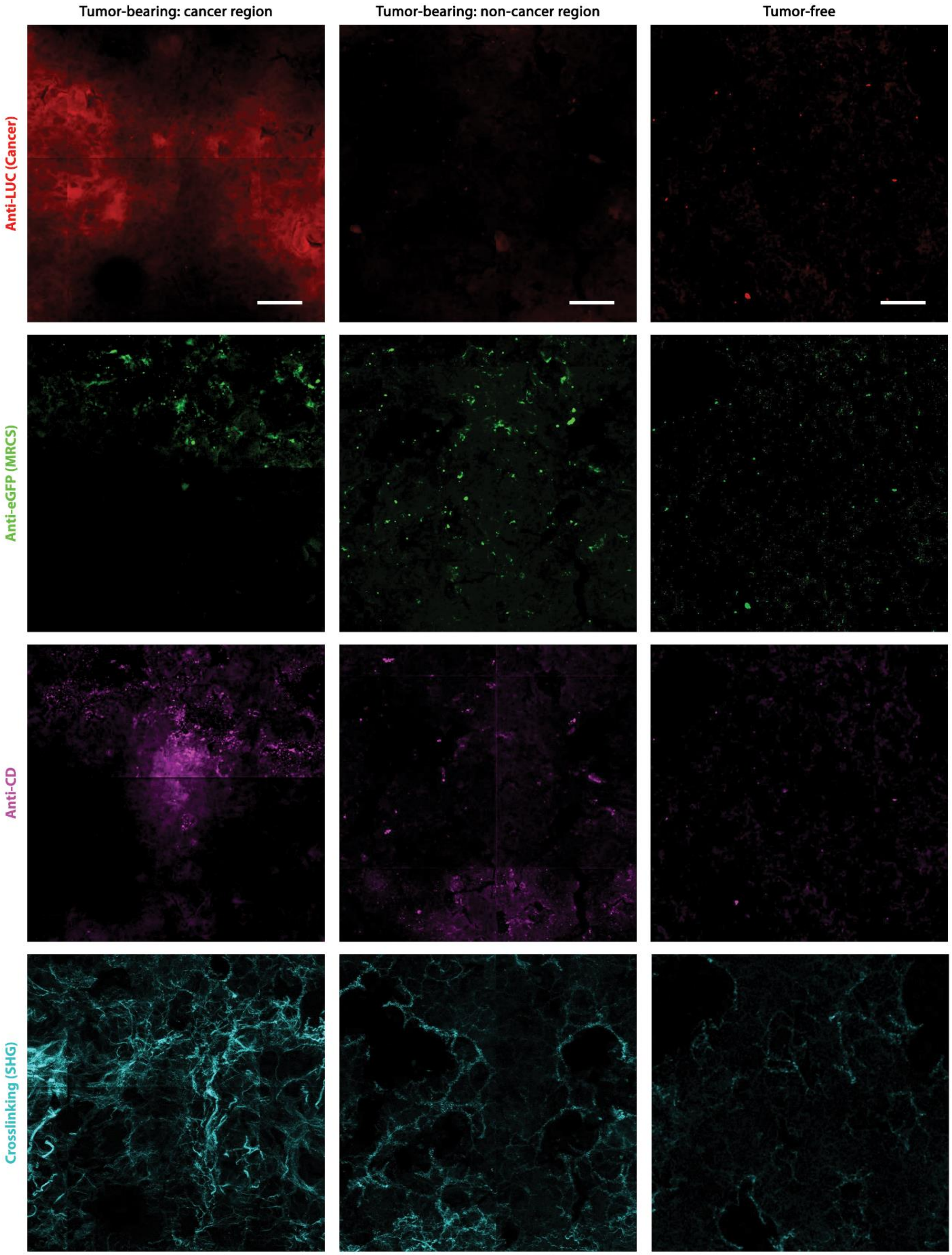

Fig. 4.S4. **Split channel views of MRCS activation in the metastatic niche in vivo**

Frozen sections of lungs of Luc-RFP-231 tumor-bearing NSG mice (cancer region and non-cancer region) and tumor-free NSG mice sacrificed 24 hours after infusion of MRCS-CD co-transfected with eGFP were stained with anti-Luc (red) to detect lung metastasis, anti-CD (magenta) for CD expressed by MRCS-CD, and anti-eGFP (green) for MRCS-CD tracking. Second harmonic generation (SHG) imaging of collagen networks (cyan) was also presented and overlaid on IHC imaging in Fig. 4.1. The data indicate that the MRCS-CD and its specific activation were co-localized with lung metastatic sites and collagen crosslinking and linearized networks. Scale bar = 50 μm.

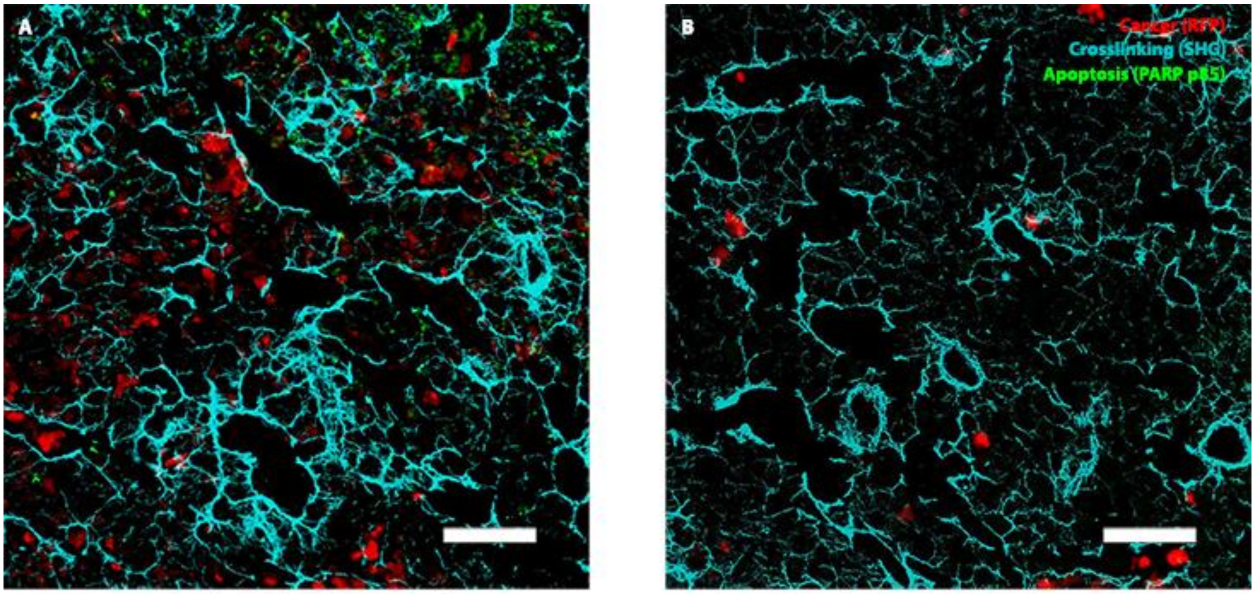

Tumor-bearing: high- density cancer region

Tumor-bearing: low-density cancer region

Fig. 4.S5. Crosslinking-specific tissue damage by MRCS in response to mechano-cues in the metastatic niche in vivo

Frozen sections of lungs of Luc-RFP-231 tumor-bearing NSG mice sacrificed after MRCS-CD infusion and 5-FC treatment (Day 9) were stained with anti-PARP p85 (green) for tissue apoptosis. RFP signal (red) indicates the presence of lung metastasis. SHG imaging of collagen networks (cyan) was overlaid with IHC imaging. (**A**) Tissue damage was only observed in lung metastatic sites with crosslinked collagen network but not in less crosslinked (**B**) regions, indicating that the MRCS-CD and its specific tissue damage were co-localized with lung metastatic sites and collagen crosslinking and linearized networks. Scale bar = 100 μm.

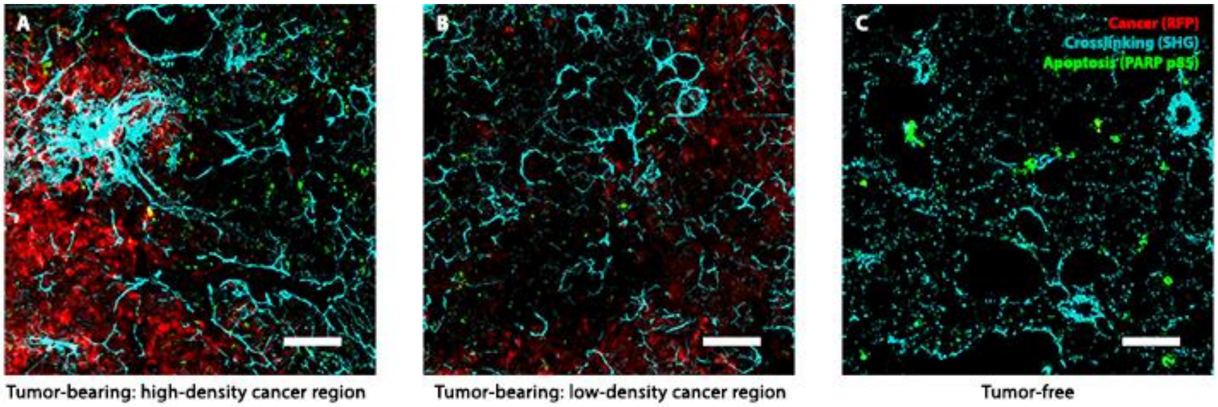

Fig. 4.S6. Constitutively CD-expressing MSCs causing non-specific tissue damage in vivo

Frozen sections of lungs of Luc-RFP-231 tumor-bearing NSG mice and tumor-free NSG mice sacrificed after CD-MSC infusion and 5-FC treatment (Day 9) were stained with anti-PARP p85 (green) for tissue apoptosis. RFP signal (red) indicates the presence of lung metastasis. SHG imaging of collagen networks (cyan) was overlaid with IHC imaging. Non-specific tissue damage was observed in both (**A** and **B**) tumor bearing and (**C**) tumor free lungs regardless of the extent of collagen crosslinking. Scale bar = 100 µm.

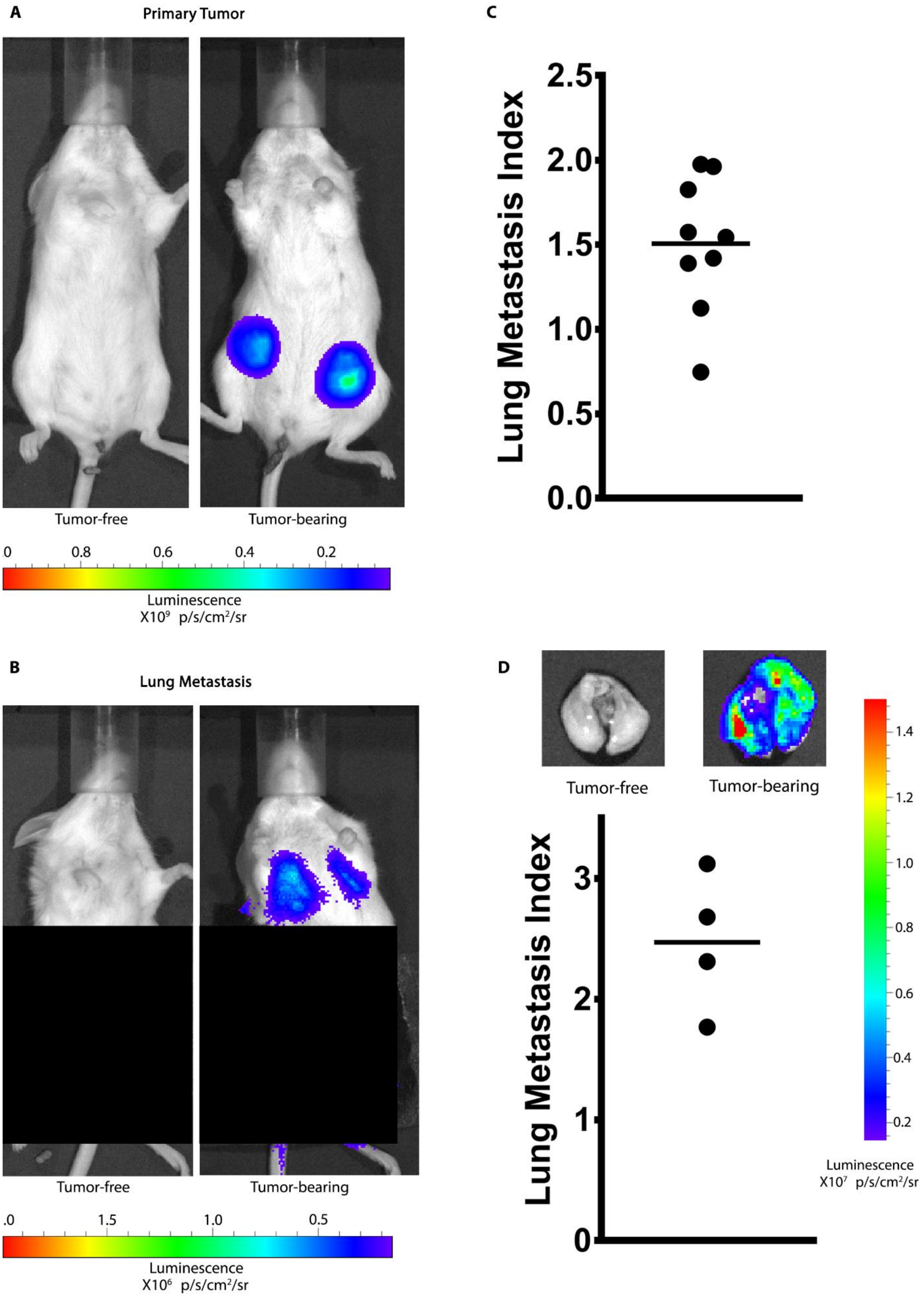

[redacted]

[redacted]

Fig. 4.S7. Spontaneous lung metastasis model establishment

(**A** to **C**) 6 weeks after subcutaneous implantation of Luc-RFP-231 into fat pads of female NSG mice, in vivo luciferase imaging was performed with an IVIS Lumina. Representative pictures of in vivo luciferase imaging of (**A**) primary tumors and (**B**) lung metastasis. Primary tumors were covered with opaque tape during imaging to prevent oversaturation. Black squares were added for consistency. (**C**) Quantification of luciferase activity of Luc-RFP-231 in the lungs of tumor-bearing NSG mice 6 weeks after Luc-RFP-231 implantation. $n = 9$ (**D**) 6 weeks after Luc-RFP-231 implantation, tumor-bearing NSG mice were sacrificed, and lungs were imaged with an IVIS Lumina. $n = 4$. Lung Metastasis Index = Log_{10} [(luciferase read of the tested tumor-bearing mouse/lung) / (luciferase read of tumor-free mice/lungs average)], such that the LMI of tumor-free mice or lungs = 0.

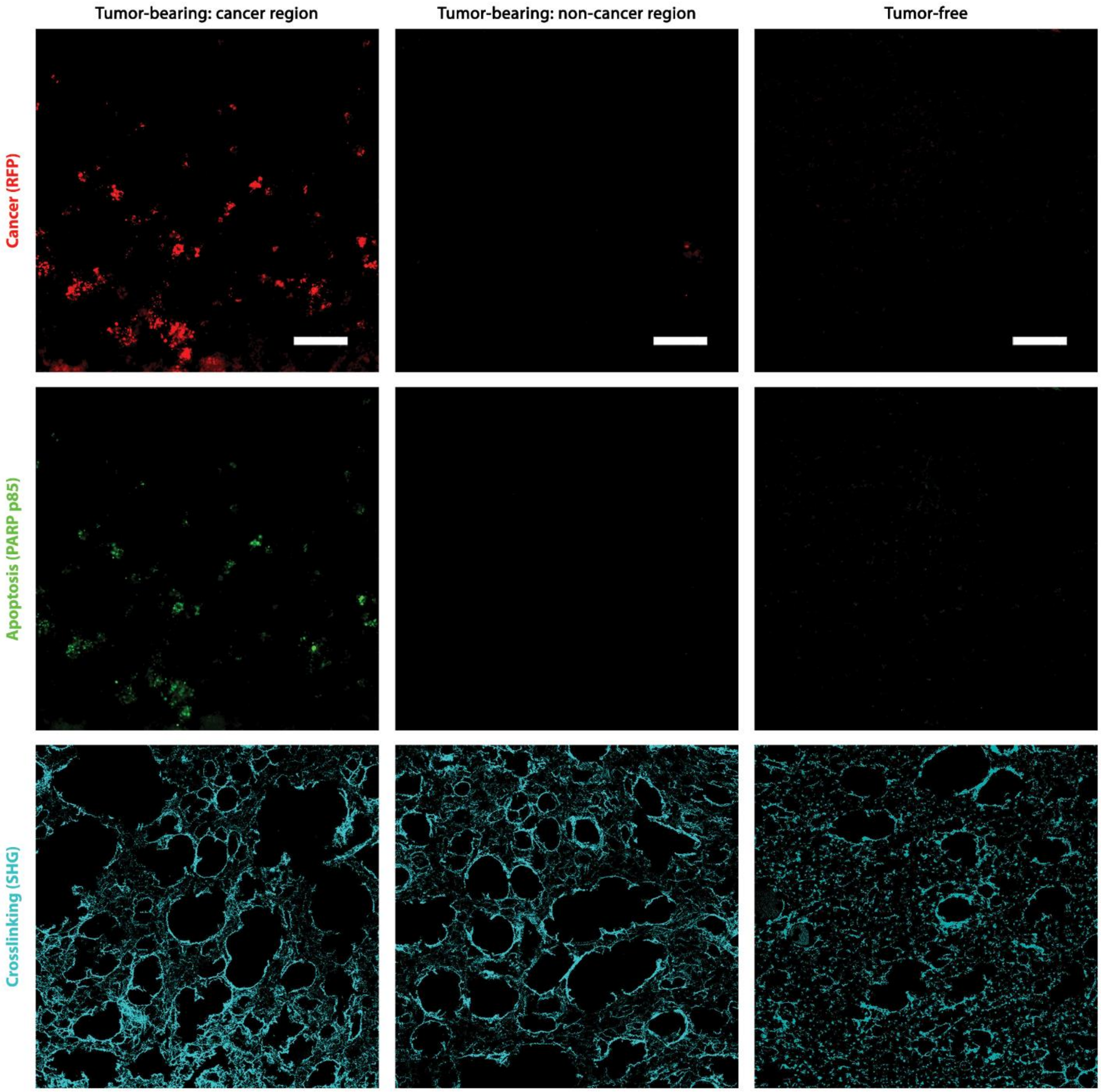

Fig. 4.S8. Split channel views of crosslinking-specific tissue damage by MRCS in the metastatic niche in vivo in spontaneous lung metastasis model

Frozen sections of lungs of tumor-bearing NSG mice with Luc-RFP-231 spontaneous lung metastasis from primary tumors (cancer region and non-cancer region) and tumor-free NSG mice sacrificed after MRCS-CD infusion and 5-FC treatment as indicated (Day 9) were stained with anti-PARP p85 (green) for tissue apoptosis. RFP signal (red) indicates the presence of lung metastasis. SHG imaging of collagen networks is also shown (cyan).

4.8 References

1. Erler, J.T., et al., *Hypoxia-induced lysyl oxidase is a critical mediator of bone marrow cell recruitment to form the premetastatic niche.* Cancer Cell, 2009. **15**(1): p. 35-44.
2. Wang, H., et al., *Trafficking mesenchymal stem cell engraftment and differentiation in tumor-bearing mice by bioluminescence imaging.* Stem Cells, 2009. **27**(7): p. 1548-58.
3. Cox, T.R., et al., *LOX-mediated collagen crosslinking is responsible for fibrosis-enhanced metastasis.* Cancer Res, 2013. **73**(6): p. 1721-32.
4. Levental, K.R., et al., *Matrix crosslinking forces tumor progression by enhancing integrin signaling.* Cell, 2009. **139**(5): p. 891-906.
5. Erler, J.T. and A.J. Giaccia, *Lysyl oxidase mediates hypoxic control of metastasis.* Cancer Res, 2006. **66**(21): p. 10238-41.
6. Erler, J.T., et al., *Lysyl oxidase is essential for hypoxia-induced metastasis.* Nature, 2006. **440**(7088): p. 1222-6.
7. Engler, A.J., et al., *Matrix elasticity directs stem cell lineage specification.* Cell, 2006. **126**(4): p. 677-89.
8. Cox, T.R. and J.T. Erler, *Remodeling and homeostasis of the extracellular matrix: implications for fibrotic diseases and cancer.* Dis Model Mech, 2011. **4**(2): p. 165-78.
9. Gasiorowski, J.Z., C.J. Murphy, and P.F. Nealey, *Biophysical cues and cell behavior: the big impact of little things.* Annu Rev Biomed Eng, 2013. **15**: p. 155-76.
10. Sherratt, M.J., *Tissue elasticity and the ageing elastic fibre.* Age (Dordr), 2009. **31**(4): p. 305-25.
11. McPherson, J.M., S.J. Sawamura, and A. Conti, *Preparation of [3H]collagen for studies of the biologic fate of xenogenic collagen implants in vivo.* J Invest Dermatol, 1986. **86**(6): p. 673-7.
12. Frantz, C., K.M. Stewart, and V.M. Weaver, *The extracellular matrix at a glance.* J Cell Sci, 2010. **123**(Pt 24): p. 4195-200.
13. Hall, J.M., et al., *Activation of the aryl-hydrocarbon receptor inhibits invasive and metastatic features of human breast cancer cells and promotes breast cancer cell differentiation.* Mol Endocrinol, 2010. **24**(2): p. 359-69.
14. Trounson, A., et al., *Clinical trials for stem cell therapies.* BMC Med, 2011. **9**: p. 52.
15. Liu, L., et al., *From blood to the brain: can systemically transplanted mesenchymal stem cells cross the blood-brain barrier?* Stem Cells Int, 2013. **2013**: p. 435093.
16. Ankrum, J. and J.M. Karp, *Mesenchymal stem cell therapy: Two steps forward, one step back.* Trends Mol Med, 2010. **16**(5): p. 203-9.
17. Droujinine, I.A., M.A. Eckert, and W. Zhao, *To grab the stroma by the horns: from biology to cancer therapy with mesenchymal stem cells.* Oncotarget, 2013. **4**(5): p. 651-64.
18. El-Haibi, C.P., et al., *Critical role for lysyl oxidase in mesenchymal stem cell-driven breast cancer malignancy.* Proc Natl Acad Sci U S A, 2012. **109**(43): p. 17460-5.
19. Brader, P., et al., *Imaging of lymph node micrometastases using an oncolytic herpes virus and [F]FEAU PET.* PLoS One, 2009. **4**(3): p. e4789.
20. Singh, A.K., et al., *Effect of thermal stress on HSP70 expression in dermal fibroblast of zebu (Tharparkar) and crossbred (Karan-Fries) cattle.* J Therm Biol, 2014. **43**: p. 46-53.

21. Liu, L., et al., *Exogenous marker-engineered mesenchymal stem cells detect cancer and metastases in a simple blood assay.* Stem Cell Res Ther, 2015. **6**(1): p. 181.
22. Bianchini, P. and A. Diaspro, *Three-dimensional (3D) backward and forward second harmonic generation (SHG) microscopy of biological tissues.* J Biophotonics, 2008. **1**(6): p. 443-50.
23. Campagnola, P.J., et al., *Three-dimensional high-resolution second-harmonic generation imaging of endogenous structural proteins in biological tissues.* Biophys J, 2002. **82**(1 Pt 1): p. 493-508.
24. Altendorf, H., et al., *Imaging and 3D morphological analysis of collagen fibrils.* J Microsc, 2012. **247**(2): p. 161-75.
25. Liu, F. and D.J. Tschumperlin, *Micro-mechanical characterization of lung tissue using atomic force microscopy.* J Vis Exp, 2011(54).
26. Plodinec, M., et al., *The nanomechanical signature of breast cancer.* Nat Nanotechnol, 2012. **7**(11): p. 757-65.

CHAPTER 5:

USING BIOPHYSICAL CUES TO STUDY CANCER BIOLOGY

Authors: **Shirley X. Zhang**[1-3], Jan Zimak[3,4], Weian Zhao[1-6]

Affiliations:

[1]Department of Biomedical Engineering, University of California-Irvine, Irvine, California, 92697, USA.

[2]Edwards Life Sciences Center for Advanced Cardiovascular Technology, University of California-Irvine, Irvine, California, 92697, USA.

[3]Sue and Bill Gross Stem Cell Research Center, 845 Health Sciences Road, University of California-Irvine, Irvine, California, 92697, USA.

[4]Department of Pharmaceutical Sciences, University of California-Irvine, Irvine, California, 92697, USA.

[5]Chao Family Comprehensive Cancer Center, University of California-Irvine, Irvine, California, 92697, USA.

[6]Department of Biological Chemistry, University of California-Irvine, Irvine, California, 92697, USA.

5.1 Introduction

Biophysical cues, as discussed in previous chapters, are attractive biomarkers targeted cancer therapy due to the intrinsic mechanical characteristics of solid tumors. However, there are many potential uses of this targeted approach outside of therapeutic applications. At a fundamental level, there is still much we do not understand about the mechanics of the tumor microenvironment (TME), and, by extension, the effect of those mechanics on cancer onset, progression, and metastasis. Here, we will discuss using an engineered cell-based stiffness sensor to directly probe the TME to further our understanding of cancer mechanobiology.

Physicians have long used physical palpation to detect cancer nodules [1], but we now know that this stiffness difference is primarily due to collagen density, crosslinking, and fiber linearization within the tumor microenvironment (TME) [2-4]. Increased tissue stiffness facilitates tumor growth, invasion, and metastasis and can affect treatment efficacy and resistance [1, 5]. However, the mechanisms that underlie how tumor cells interact reciprocally with their mechanical environment during cancer progression remain incompletely understood [6, 7]. One critical barrier to further understanding stiffness-mediated tumor progression lies in the limitations of current technologies to characterize physical properties of tissues at a cellular resolution in their native environment. Imaging modalities such as ultrasound and elastography are capable of longitudinal measurements *in vivo* but have limitations in spatial resolution and feature size [8]. Conversely, AFM, microrheology, and traction force microscopy have high spatial resolution but cannot be used *in vivo* and only provide surface measurements [9, 10]. Techniques such as FRET-based molecular sensors, magnetic tweezers and optical traps tend to interrogate particular molecular pathways but fail to characterize mechanobiology at a tissue level [11-14]. Importantly, most existing technologies measure substrate mechanics but cannot directly interrogate cell responses.

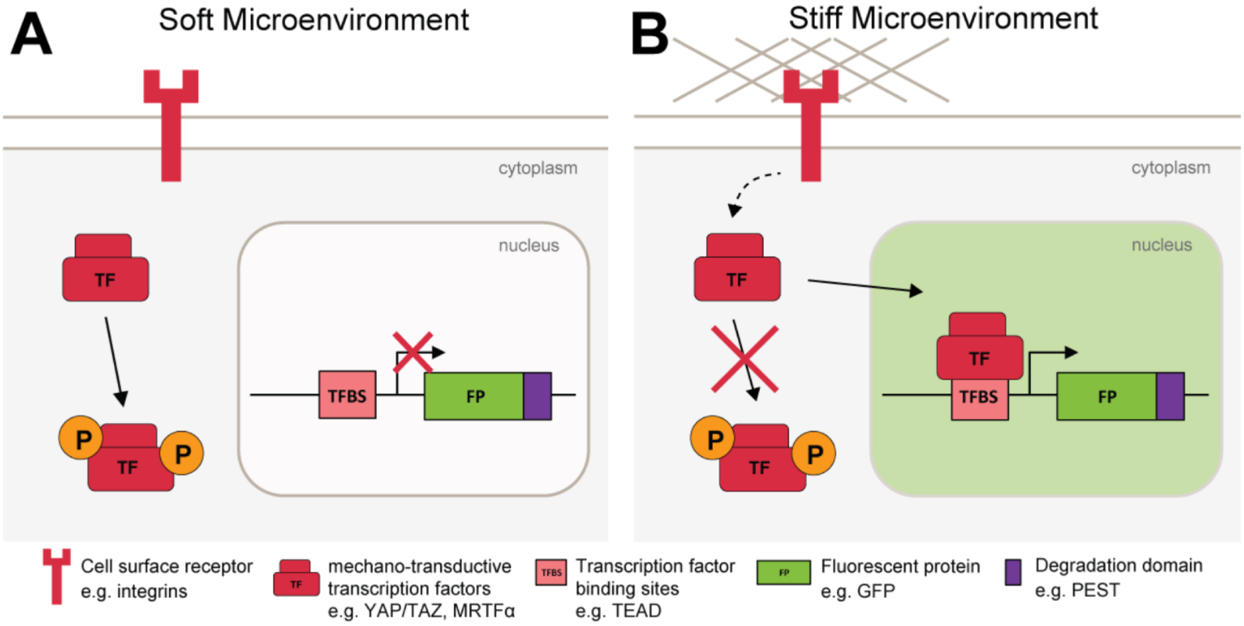

Fig 5.1. Scheme of cell-based mechanosensors

(A) Cell sensors do not express fluorescent reporter (FP) on soft microenvironments.

(B) In response to increased stiffness, mechano-sensitive transcription factor localizes to the nucleus to drive expression of FP.

5.2 From the Cell's Perspective

Cells constantly sense their biochemical and biophysical surroundings with unparalleled spatiotemporal resolution and precision and can rapidly transduce that information to regulate downstream gene expression through transcriptional programs. For instance, the transcriptional factor YAP(Yes-associated protein)/TAZ(transcriptional co-activator with PDZ-binding motif) preferentially translocates to the nucleus to trigger downstream gene expression in a stiffness-dependent manner [15]. Leveraging cell's innate mechanosensing mechanisms, we propose developing cell-based mechanosensors that can dynamically and quantitatively assess tumor tissue mechanics in their native environment *in vivo.* Using CRISPR/Cas9-mediated site-specific genomic integration of modular genetic circuits, we will repurpose known mechano-sensitive transcriptional regulators such as YAP/TAZ to drive downstream expression of reporter fluorescent proteins (Fig. 5.1). These fluorescent sensors will be dynamic and reversible and can quantitatively interrogate a wide range of distinct biologically-relevant stiffness in a multiplex and continuous fashion.

Currently available technologies rely on external measurements to infer the effect of biophysical cues on resident cells. Thus, a cell-based mechanosensor will reveal what cells actually "feel" in their TME and represent a paradigm-shifting method of dynamically interrogating tumor mechanics during disease progression or treatment over time at a cellular resolution *in vivo.* With this approach focused on the cell's perspective, cancer mechanobiology shifts the paradigm from characterizing ECM mechanics as most existing techniques due to equipping cancer cells with mechanosensors to reveal how they actually sense and respond to TME cues. In particular, incorporating mechanosensors with transcriptional programs allows us to examine how cells integrate mechanical and other cues together and translate that information into functional readouts. To our knowledge, our cell-based mechanosensors, for the first time, will allow one to interrogate dynamic cell-ECM interactions in the native, 3D TME *in vivo* in longitudinal studies. It also enables dissection of cellular level variability and survey of the biomechanical landscape across the entire tumor tissue through multiscale, temporal and spatial analysis.

5.3 Engineering Cell Stiffness Sensors

Cell-based mechanosensors can dynamically and quantitatively assess tumor tissue mechanics at cellular resolution in their native environment *in vivo.* Using modular genetic circuits, we will construct multiplex sensors that activate over a biologically relevant stiffness range and produce cells with multiple colors indicating their response to a specific stiffness. We will engineer non-tumorigenic or tumorigenic breast epithelial cells with multiple transcriptional units, each with distinct number of repeats for transcription factor binding sites to two major mechano-sensitive transcription factors: YAP/TAZ and MRTFα. This will allow us to generate a repertoire of mechanosensors to quantitatively sense distinct stiffness in a multiplex fashion.

Our sensors are constructed by repurposing the cell's innate mechanosensing machinery. Triggered by mechanical stimuli (e.g., increased ECM stiffness), mechano-sensitive transcription factors (e.g. YAP/TAZ) translocate to the nucleus and bind to synthetic promoters to drive downstream expression of reporter fluorescent proteins (Fig. 5.1). Therefore, individual sensors function by changing the expression level of reporters (fluorescence intensity) in response to different nuclear concentrations of the mechano-sensitive transcription factors (i.e. dosage of mechanical stimuli). Using modular genetic circuits, we will engineer cells with multiple transcriptional units, each with distinct number of repeats for transcription factor binding sites (TFBS). This design augments transcription factor-TFBS interactions in a cooperative fashion and allows our mechanosensors to quantitatively sense distinct stiffness in a multiplex assay (Fig. 5.2A, B, long-pass filters). Stiffness reporter specificity and resolution can be improved using a band-pass filter where reporters of high-stiffness will also co-express protease that specifically degrades reporters of lower stiffness (Fig. 5.2C).

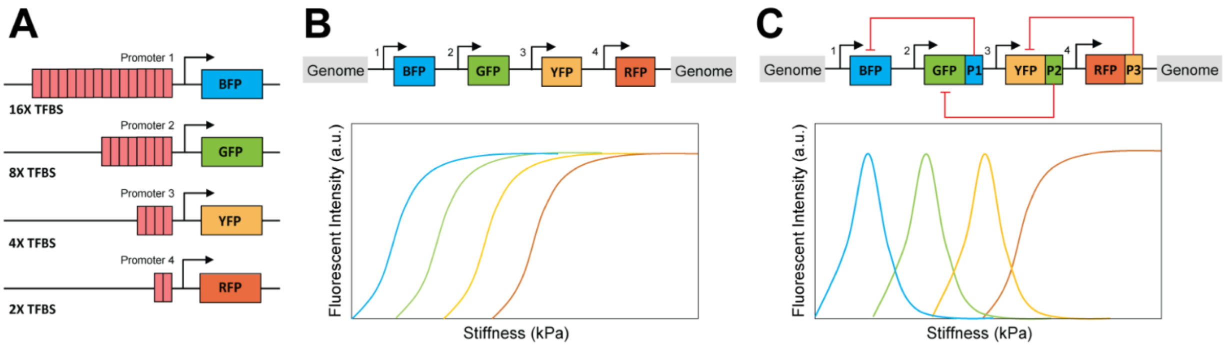

Fig 5.2. Scheme of stiffness sensors

(A) Varying number of TFBS repeats to construct singleplex sensors with different stiffness response, **(B)** Long-pass filter multiplex sensor design, and **(C)** Band-pass filter multiplex sensor design with inhibition by protease cleavage. P1, P2, P3, proteases for fluorescent proteins; BFP, GFP, YFP, and RFP: blue, green, yellow and red fluorescent proteins, respectively.

We will construct the stiffness-sensor in non-tumorigenic MCF-10A and its control H-Ras transformed MCF-10AT epithelial cells. These cell lines are chosen as they 1) are isogenic, 2) sense and respond to ECM stiffness using known mechano-sensitive transcription factors including YAP/TAZ, 3) exhibit difference stiffness sensitivities [16, 17]: MCF10A (experimental group) is mechanically sensitive, so they will only become fluorescent as the sensors turn on with increased stiffness. MCF10AT (positive control) will be always fluorescent because the oncogene forces sensors "on", independent of stiffness, and 4) are clonal making sensor insertion simple. We will make stiffness-sensors for established mechano-sensitive nuclear effectors: YAP/TAZ and myocardin-related transcription factor (MRTFα). YAP/TAZ and MRTFα exhibit distinct, substrate stiffness-dependent mechanoregulation in many tumor cell lines [17-19]. This will give our sensor platform expanded range across cell lines and stiffness. Our stiffness-inducible synthetic promoters are typically comprised of a specific number of repeat TFBS upstream of a minimal promoter (e.g. YB-TATA). By varying TFBS consensus sequences, number of binding site repeats, and repeat spacing we can control the dynamics and long-term or steady-state expression level of our sensors (Fig. 5.2A). For instance, we have demonstrated that increasing the number of TFBS from 4 to 8 can dramatically alter the stiffness response in HEK293T cells on tissue culture plastic (Fig. 5.3). TFBS sequences will be identified using a custom computational algorithm that uses widely available ChIP-Seq data to pad the consensus sequence [20]. Each variant will induce nuclear-localized GFP expression and will be assembled using landing pads and integrated using CRISPR/Cas9 to the safe harbor locus, AAVS1 [21]. This precise chromosomal integration of genetic payloads ensures copy number consistency of our sensors [21, 22]. We will first evaluate the ON/OFF capability of our sensors by measuring their steady-state stiffness response on tissue culture plastic (~1 GPa [23]) (positive) with or without mechano-inhibitors including blebbistatin [24] (negative) using fluorescence microscopy.

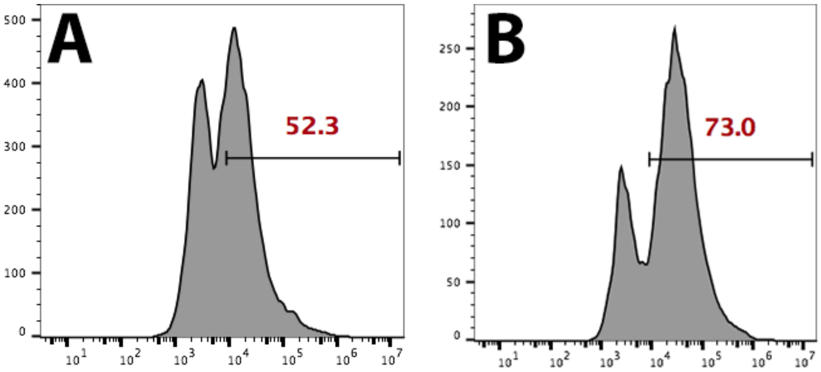

Fig 5.3. Effect of transcription factor binding site repeats

YAP/TAZ sensors with greater number of TFBS have a more sensitive response on tissue culture plastic in HEK293T cells. Cells were engineered with **(A)** 4x and **(B)** 8x TFBS respectively. Flow cytometry data shows both higher fraction of cells (73% vs. 52%) respond as well as a shift in mean fluorescence intensity (1x10^^{4} vs 2.5x10^^{4}) as the number of TFBS increased.

We will then construct multiplexed sensors by integrating the 4 sensors from each transcription factor (YAP/TAZ and MRTFα) described above into one multi-transcriptional unit (TU) vector ("long-pass filters", Fig. 5.2B). Each TU is separated by chromatin insulators to isolate each TU from genomic enhancer domains and promoters in adjacent TUs, thus allowing independent activation of each sensor. Therefore, the multiplexed sensor will be a series of fluorescent reporters that each activate at distinct levels of stiffness including mTurquoise2 (blue-green, 474nm), mNeonGreen (green-yellow, 517nm), mOrange2 (orange-red, 565nm) and mKate2 (far-red, 633nm). These fluorescent proteins are selected for their significant spectral separation, brightness and low toxicity[25].

We will then further improve stiffness reporter sensitivity and resolution by coupling each stiffness sensor together to create a novel band-pass filter stiffness sensor (Fig. 5.2C).

The goal with this genetic circuit is to decrease the number of fluorescent reporters expressed at one time enabling increased resolution of stiffness-sensing due to less spectral overlap at each stiffness. To achieve this, reporters of high-stiffness will also co-express a protease that specifically degrades reporters of lower stiffness. Specifically, the band-pass filter variants will inducibly express fluorescent proteins carrying peptides sequences that are degradable by viral proteases (TEVp, SbMVp, and PPVp) [26]. We will validate the specific degradability and orthogonality of our multiplexed band-pass filter stiffness sensor. The steady state ON/OFF states of the multiplexed stiffness sensors including both long-pass and band-pass filters will be characterized as described above.

5.4 Stiffness Sensor Validation *in vitro*

Prior to construction of the multiplexed sensors, we will first test the stiffness-sensing capability of a simpler sensor construct. We chose to use MDA-MB-231 breast cancer cells as a control, as these cells have previously been shown to be mechanoresponsive using the YAP/TAZ mechanoregulation pathway.

Plasmids for a two-color stiffness sensor system are cloned by Gibson assembly. One expression unit is a constitutive promoter to express GFP. The second expression unit is a stiffness-sensing YAP/TAZ (Yes-associated protein/transcriptional coactivator with PDZ-binding motif) activated promoter to express RFP and a silencing domain (KRAB) to turn off GFP expression. MDA-MB-231 cells are transduced via nucleofection. A consistent cell line of MDA-MB-231 cells with the desired gene expression was established after FACS and clonal selection. Stiffness sensor cells are validated in vitro by culturing on 2D polyacrylamide hydrogels of varying stiffness (1 to 40kPa) for up to 10 days. Cells are imaged for both GFP and RFP fluorescence, quantified by Nikon analysis software.

After 5-10 days of culture on polyacrylamide hydrogels of varying stiffness, the normalized fluorescent ratio of the cells on each stiffness is calculated. Each data point is normalized to the RFP signal on 40kPa, and the ratio is calculated as the RFP signal divided by the GFP signal. It is expected that the stiffer the substrate, the more YAP/TAZ mediated expression of RFP and KRAB, and thus a higher resulting calculated ratio. The GFP signal is not completely silenced, even on the stiffest hydrogel, due to the inherent limitations on the efficiency of the KRAB silencing domain. Nevertheless, a statistically significant ($p<0.001$) trend is observed in the fluorescent ratio between cells cultured on different stiffness hydrogels (Figure 5.4).

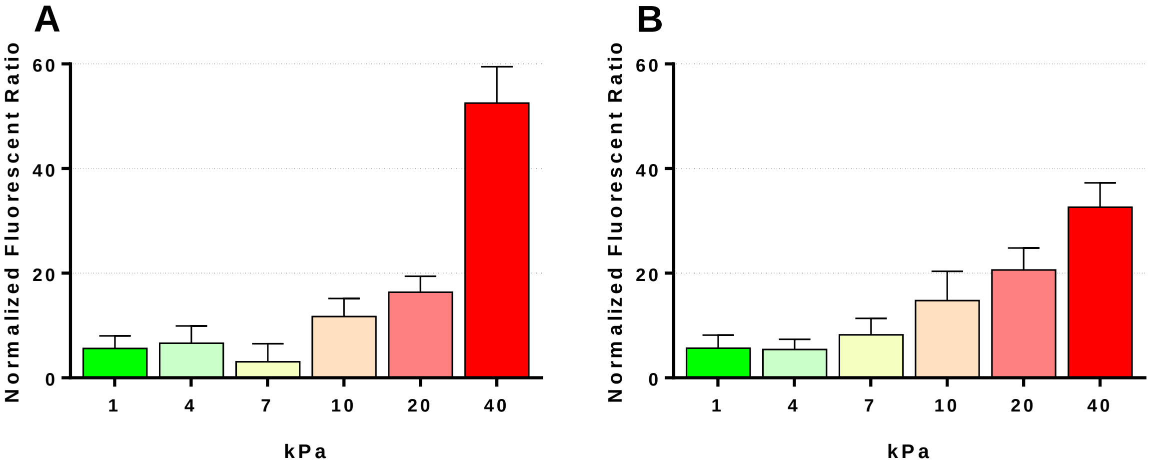

Figure 5.4. Stiffness-specific reporter response in engineered cell sensors

Engineered MDA-MB-231 cultured on polyacrylamide gels of varying elastic moduli for (A) 5 or (B) 10 days show higher RFP/GFP fluorescent signal ratio on stiffer hydrogels, indicating successful detection and reporter gene expression activation in response to increased substrate stiffness.

Next, we will characterize and determine the range of biologically relevant matrix stiffness at which our engineered singleplex and multiplexed sensors activate, the sensitivity of the sensors, and their reversible dynamics. To characterize the mechano-sensitivity of the engineered cell lines, we will use 2D collagen-conjugated methacrylated hyaluronic acid (meHA) hydrogel substrates with a stiffness gradient between 0.1 and 40 kPa. This range encompasses normal and malignant tumor tissues [27]. Using our established protocol [28, 29], MeHA hydrogel stiffness can be tuned spatiotemporally by adjusting the amount of photoinitiator Irgacure 2959 and UV light exposure (<90 sec) used in free radical polymerization. Our studies on cell sensor dynamics and reversibility may allow us to uniquely characterize cell mechanical memory, which is poorly understood [30].

To investigate cell sensor sensitivity, MCF10A and MCF10AT cells containing the sensors will be seeded on gradient MeHA hydrogel substrates (created by gradient photomasks and UV exposure), GFP fluorescence will be imaged via Nikon microscope, and activated cell sensor intensity will be quantified after 24 hours. The smallest difference in substrate stiffness on which a statistically different sensor response is detected will indicate system sensitivity. Previous studies suggest that mechanotransduction in response to matrix stiffness are often reversible and dynamic [31, 32]. To investigate cell sensor dynamics and reversibility, the engineered cells will be seeded on soft MeHA hydrogels (<1kPa) where sensor output measured and then the hydrogel will be sequentially polymerized with light-activated crosslinking to stiffen it (>10 kPa) and sensor output measured again. Hydrogel stiffness can be reversed by degradation via hyaluronidase [33]. Neither UV nor hyaluronidase significantly harms cells. GFP fluorescence will be live-imaged for 24 hours after each stiffness change and cell sensor intensity quantified. To verify that reporter activation is specifically dependent on matrix stiffness, we will treat cells with inhibitors of focal adhesion kinase (FAK) (PF228) [34] and myosin light chain kinase (blebbistatin and ML7) [24] which abrogate downstream matrix stiffness signal transduction.

An important new capability of our cell sensor system is the ability to report stiffness in a 3D microenvironment. To test that, engineered cell sensors will be plated onto meHA substrate with stiffness gradient [35, 36] and then coated with Matrigel in a 'sandwich' format to create a 3D culture environment, as established in the literature [16]. Cells in 3D will be imaged via confocal microscopy, and sensor response will be evaluated as above. Each cell experiment on hydrogel substrates will be performed in triplicate, and average nuclear fluorescent signal of at least 30 cells from each of the separate hydrogels will be used to characterize each cell sensor individually. Pearson's correlation coefficient will be tested between GFP fluorescence and substrate stiffness. Furthermore, we will use linear regression to quantify how sensor fluorescence and substrate stiffness changes with each other.

We will repeat the tunable hydrogel experiments and analyses for our multiplexed stiffness sensors to assess their stiffness sensitivity and dynamics. We will measure difference in intensity and variability of multiplexed sensors using a ratiometric approach by measuring the relative expression level of each reporter [37]. This approach allows us to reduce non-specific interference such as tissue autofluorescence and photobleaching in fluorescence measurement and analysis. We also expect ratiometric differences to be more distinct for our band-pass sensor compared to our long-pass sensor. The peak activation stiffness will be identified for each promoter, and the difference in stiffness between peaks for a multiplexed sensor will be quantified to evaluate the overlap of stiffness response.

5.5 Stiffness Sensor Validation *in vivo*

To demonstrate that sensors have the capability of measuring stiffness in the native tumor microenvironment, we will test them in murine cancer models. Cellular-level stiffness maps of tumor mechanical landscape will be constructed, which will be quantitatively compared to *ex vivo* AFM analysis, thus characterizing the precision, resolution, dynamic range of our *in vivo* stiffness sensor.

Multiplexed sensors in MCF10A cells (5×10^5 cells) will be suspended in Matrigel and then transplanted orthotopically into mammary fat pads of adult female nonobese diabetic/ severe combined immunodeficiency gamma (NSG) mice [38]. Female mice are most appropriate for a model of breast cancer, which overwhelmingly affect women. This murine xenograft model is widely used to develop breast tumors that are expected to manifest a natural and variable mechanical landscape as tumor grows, which is ideal for us to characterize our cell sensors. Specifically, MCF10A cells are mechanosensitive and can form tumors in Matrigel or hydrogel when stiffened in vivo [17], recapitulating natural malignant transformation of epithelial cells.

As a control, as with the *in vitro* experiments we first established a model using MDA-MB-231 as a control. With the two-color construct as described above, we established a primary tumor xenograft. After 8 weeks, the tumors were harvested, fixed in 4% PFA, cryosectioned and imaged under fluorescent microscopy. Since the cancer cells themselves are expressing the fluorescent proteins, no antibodies were needed to visualize them.

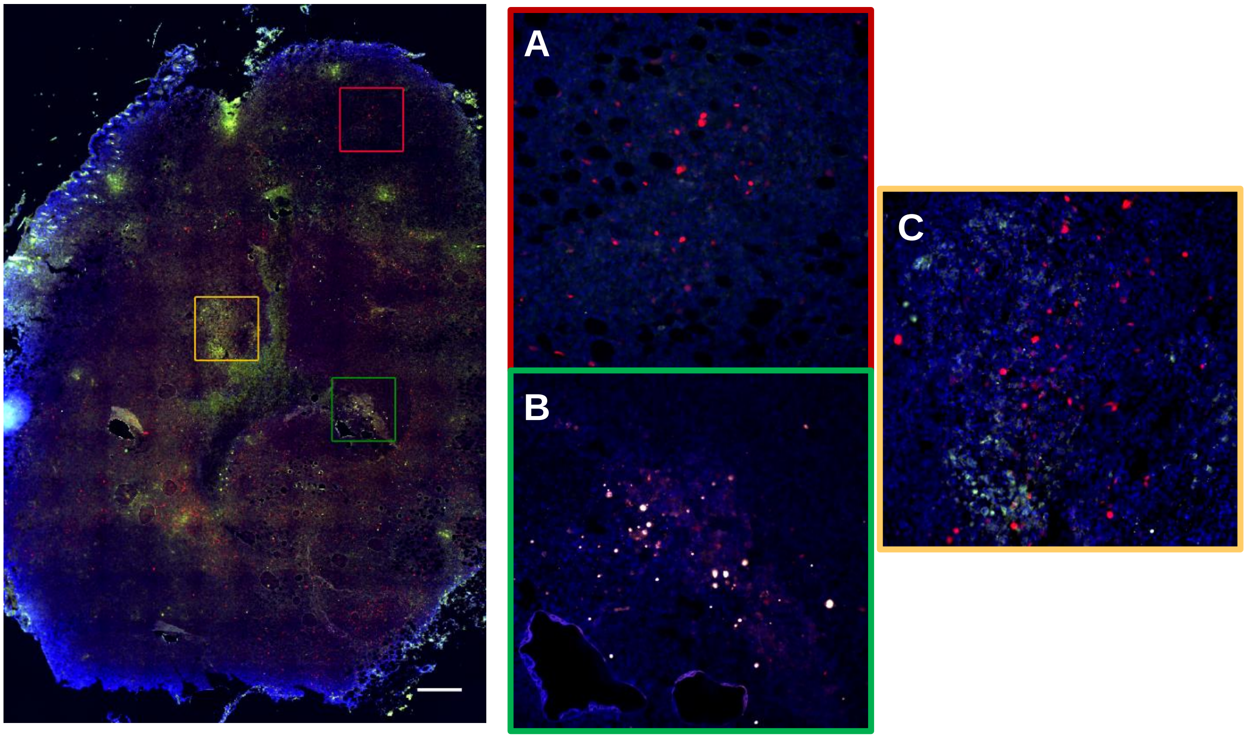

Figure 5.5. Stiffness sensor breast tumor

Engineered MDA-MB-231 were transplanted orthotopically into mammary fat pads of adult female nonobese diabetic/ severe combined immunodeficiency gamma (NSG) mice. Tumors were harvested and sectioned after 8 weeks. Close-up images of (A) distal and (B-C) central regions of the tumor are shown. Nuclei DAPI stain in blue.

The tumor showed a clear necrotic region in the center (Fig 5.5), and most tumor cells close to this region were green, indicating they are sensing lower stiffness. Cells closer to the edge of the tumor tended to be red, indicating they are sensing increased stiffness. Further experiments and samples are required to quantify this trend for statistical analysis. However, given what is known about the softer necrotic cores of solid tumors, thus far the data matches expected results and the *in vitro* data. It is also important to note that, as was also observed in the *in vitro* experiments, many of the engineered cells have no fluorescence, or very low fluorescence. This is in part due to the innate heterogeneity of the MDA-MB-231 cell line, and differences in fluorescent expression can be observed even after sorting and clonal selection. More so, though, the heterogeneity is likely due to the KRAB silencing domain which will not be used in future constructs to avoid recurrence of this issue.

To directly assess the cell sensor capability against known measurements of tissue stiffness, we will also utilize SHG two-photon microscopy coupled with fluorescence on the tissue sections to quantify and co-localize areas of high collagen density, crosslinking and linearization with fluorescence from the cell sensors. Using this approach, we have imaged frozen lung tissue sections containing breast cancer metastases with SHG and fluorescence imaging overlay. We will also use an MFP-3D-Bio AFM (Asylum Research) to create a stiffness map of tissue sections and overlay cell sensor fluorescence. AFM data will be analyzed using custom-written code Matlab to determine Young's Modulus based on a Hertz model [28, 29]. By co-localizing the local stiffness measurements from AFM and the ratiometric fluorescence from our multiplexed sensors we will validate the stiffness response of cells with high spatial resolution. Data from sequential sections will be used to reconstruct 3D stiffness maps of whole tumors. Tumorigenic MCF10AT carrying sensors will be used as positive control.

We will characterize multiplex sensor dynamics with changing tissue stiffness in a continuous fashion *in vivo*. We will use an established dorsal window chamber [39] to continuously monitor tumor progression and fluorescence from our cell sensors over time via intravital fluorescence microscope. The platform combines wide-field imaging and multispectral imaging modes using multiple illumination sources, a camera equipped with an electro-optic filter, and a modular design which allows the user to image the dorsal window chamber using broadband transillumination. The microscope also is equipped with standard fluorescence filter cubes that cover our reporter proteins. Briefly, dorsal skin is stretched and secured, and an incision is made. Engineered sensor cells will be injected into the exposed dermis of the window chamber skin, and the window chamber is closed with a glass coverslip. The dorsal window chamber will allow us to monitor and image the tumor growth longitudinally *in vivo* to a depth of 2000μm with a maximum tumor size of 5mm [39]. We can thus directly visualize the reporter response from our sensor cells in response to natural perturbation of the 3D TME stiffness during tumor progression. After cell injection, we will allow the resulting tumor to grow for up to 4 weeks, imaging every 3 days. After 4 weeks, the mice will be sacrificed and the tumor harvested for *ex vivo* analysis.

To manipulate tissue stiffness *in vivo* in a more controlled fashion, we will use meHA hydrogel stiffening with UV *in situ, in vivo* [17]. This also facilitates stiffness-induced transformation of MCF10A to form tumors. If MCF10A exhibits inadequate tumor formation, we will use mechano-sensitive, tumorigenic MDA-MB-231. A mammary window of orthotopic breast cancer can be used to observe the development of the primary tumor in a more native environment [40].

5.6 Discussion

In recent years, biophysical cues have emerged as important factors in the study of cell behavior and disease progression. Disease states such as cancer and fibrosis have distinct biophysical cues, such as increased tissue stiffness, which have been directly linked to patient prognosis can serve as distinct biomarkers for specifically targeting affected areas of the body. However, current methods of detection such as elastography lack spatial resolution, and direct measurements of physical properties such as atomic force microscopy require invasive biopsies. We propose an engineered cell-based stiffness sensor which can directly interrogate biophysical cues in the native tissue microenvironment.

This cell-based stiffness sensor represents a new platform technology which can directly interrogate biophysical cues of the tissue microenvironment. With these new capabilities offered by our proposed technology, we can potentially answer outstanding questions in cancer biology and treatment that were previously not possible or difficult to address due to lack of tools. For instance, the cell-based mechanosensor will allow us to construct an ongoing "stiffness map" of the heterogeneous and evolving TME as cancer progresses and to reveal how the dynamic cell-ECM interactions affect the timing and evolution of physiological events such as growth, invasion, and metastasis. New insights of cancer mechanobiology provided by this cell-based mechanosensor will therefore have far reaching clinical significance in 1) using the aberrant tumor mechanical properties ("mechanophenotype") as a diagnostic and prognosis marker to detect small metastases and pre-metastatic legions and to predict cancer invasiveness, respectively, and 2) in improving efficacy and reducing resistance of current drugs by normalizing the tumor niche as well as in developing new drugs that directly target pathological stiffening. In fact, our cell-based mechanosensor may allow functional screening for drugs that perturb ECM mechanics or cancer cell mechanosensing directly *in vivo* [41]. By correlating differences in these biophysical cues with disease states such as cancer metastases, the sensors can advance our understanding of disease development and progression.

5.7 References

1. Nagelkerke, A., et al., *The mechanical microenvironment in cancer: How physics affects tumours.* Seminars in Cancer Biology, 2015. **35**: p. 62-70.
2. Fattet, L. and J. Yang, *Molecular and Cellular Mechanobiology of Cancer*, in *Molecular and Cellular Mechanobiology*, S. Chien, A.J. Engler, and P.Y. Wang, Editors. 2016, Springer New York: New York, NY. p. 277-290.
3. Maman, S. and I.P. Witz, *A history of exploring cancer in context.* Angiogenesis, 2018. **1501**: p. 1980s.
4. Cox, T.R., et al., *LOX-mediated collagen crosslinking is responsible for fibrosis-enhanced metastasis.* Cancer research, 2013: p. canres. 2233.2012.
5. Cukierman, E. and D.E. Bassi, *Physico-mechanical aspects of extracellular matrix influences on tumorigenic behaviors.* Seminars in Cancer Biology, 2010. **20**(3): p. 139-145.
6. Przybyla, L., J.M. Muncie, and V.M. Weaver, *Mechanical Control of Epithelial-to-Mesenchymal Transitions in Development and Cancer.* Annual Review of Cell and Developmental Biology, 2016. **32**(1): p. 527-554.
7. Iskratsch, T., H. Wolfenson, and M.P. Sheetz, *Appreciating force and shape — the rise of mechanotransduction in cell biology.* Nature Reviews Molecular Cell Biology, 2014. **15**: p. 825.
8. Wickramaratne, D., et al., *Fine Needle Elastography (FNE) device for biomechanically determining local variations of tissue mechanical properties.* Journal of biomechanics, 2015. **48**(1): p. 81-88.
9. Keating, M., et al., *Spatial distributions of pericellular stiffness in natural extracellular matrices are dependent on cell-mediated proteolysis and contractility.* Acta Biomaterialia, 2017. **57**: p. 304-312.
10. Roca-Cusachs, P., V. Conte, and X. Trepat, *Quantifying forces in cell biology.* Nature Cell Biology, 2017. **19**: p. 742.
11. Kumar, A., et al., *Talin tension sensor reveals novel features of focal adhesion force transmission and mechanosensitivity.* The Journal of Cell Biology, 2016. **213**(3): p. 371-383.
12. Grashoff, C., et al., *Measuring mechanical tension across vinculin reveals regulation of focal adhesion dynamics.* Nature, 2010. **466**: p. 263.
13. Chang, C.-W. and S. Kumar, *Vinculin tension distributions of individual stress fibers within cell-matrix adhesions.* Journal of Cell Science, 2013.
14. Oldach, L. and J. Zhang, *Genetically Encoded Fluorescent Biosensors for Live-Cell Visualization of Protein Phosphorylation.* Chemistry & Biology, 2014. **21**(2): p. 186-197.
15. Dupont, S., et al., *Role of YAP/TAZ in mechanotransduction.* Nature, 2011. **474**: p. 179.
16. Wei, S.C., et al., *Matrix stiffness drives epithelial–mesenchymal transition and tumour metastasis through a TWIST1–G3BP2 mechanotransduction pathway.* Nature Cell Biology, 2015. **17**: p. 678.
17. Meng, Z., et al., *RAP2 mediates mechanoresponses of the Hippo pathway.* Nature, 2018: p. 1.
18. Zanconato, F., M. Cordenonsi, and S. Piccolo, *YAP/TAZ at the Roots of Cancer.* Cancer Cell, 2016. **29**(6): p. 783-803.

19. Liao, X.-H., et al., *MRTF-A and STAT3 synergistically promote breast cancer cell migration.* Cellular Signalling, 2014. **26**(11): p. 2370-2380.
20. Heinz, S., et al., *Simple Combinations of Lineage-Determining Transcription Factors Prime cis-Regulatory Elements Required for Macrophage and B Cell Identities.* Molecular Cell, 2010. **38**(4): p. 576-589.
21. Duportet, X., et al., *A platform for rapid prototyping of synthetic gene networks in mammalian cells.* Nucleic Acids Research, 2014. **42**(21): p. 13440-13451.
22. Guye, P., et al., *Rapid, modular and reliable construction of complex mammalian gene circuits.* Nucleic Acids Research, 2013. **41**(16): p. e156-e156.
23. Miyake, K., N. Satomi, and S. Sasaki, *Elastic modulus of polystyrene film from near surface to bulk measured by nanoindentation using atomic force microscopy.* Applied physics letters, 2006. **89**(3): p. 031925.
24. Engler, A.J., et al., *Matrix Elasticity Directs Stem Cell Lineage Specification.* Cell, 2006. **126**(4): p. 677-689.
25. Cranfill, P.J., et al., *Quantitative assessment of fluorescent proteins.* Nature Methods, 2016. **13**: p. 557.
26. *Protease orthogonality.* The International Genetically Engineered Machine Competition, 2016.
27. Samani, A., J. Zubovits, and D. Plewes, *Elastic moduli of normal and pathological human breast tissues: an inversion-technique-based investigation of 169 samples.* Physics in medicine & biology, 2007. **52**(6): p. 1565.
28. Ondeck, M.G. and A.J. Engler, *Mechanical Characterization of a Dynamic and Tunable Methacrylated Hyaluronic Acid Hydrogel.* Journal of Biomechanical Engineering, 2016. **138**(2): p. 021003-021003-6.
29. Kaushik, G., et al., *In situ mechanical analysis of myofibrillar perturbation and aging on soft, bilayered Drosophila myocardium.* Biophysical journal, 2011. **101**(11): p. 2629-2637.
30. Yang, C., et al., *Mechanical memory and dosing influence stem cell fate.* Nature Materials, 2014. **13**: p. 645.
31. Kloxin, A.M., et al., *Photodegradable Hydrogels for Dynamic Tuning of Physical and Chemical Properties.* Science, 2009. **324**(5923): p. 59-63.
32. Humphrey, J.D., E.R. Dufresne, and M.A. Schwartz, *Mechanotransduction and extracellular matrix homeostasis.* Nature Reviews Molecular Cell Biology, 2014. **15**: p. 802.
33. Burdick, J.A., et al., *Controlled degradation and mechanical behavior of photopolymerized hyaluronic acid networks.* Biomacromolecules, 2005. **6**(1): p. 386-391.
34. Slack-Davis, J.K., et al., *Cellular characterization of a novel focal adhesion kinase inhibitor.* Journal of Biological Chemistry, 2007. **282**(20): p. 14845-14852.
35. Lee, G.Y., et al., *Three-dimensional culture models of normal and malignant breast epithelial cells.* Nature Methods, 2007. **4**: p. 359.
36. Paszek, M.J., et al., *Tensional homeostasis and the malignant phenotype.* Cancer cell, 2005. **8**(3): p. 241-254.
37. Abelin, A.C., et al., *A ratiometric-based measure of gene co-expression.* BMC bioinformatics, 2014. **15**(1): p. 331.

38. Kocatürk, B. and H.H. Versteeg, *Orthotopic Injection of Breast Cancer Cells into the Mammary Fat Pad of Mice to Study Tumor Growth.* Journal of Visualized Experiments : JoVE, 2015(96): p. 51967.
39. Moy, A.J., et al., *Wide-field functional imaging of blood flow and hemoglobin oxygen saturation in the rodent dorsal window chamber.* Microvascular Research, 2011. **82**(3): p. 199-209.
40. Shan, S., B. Sorg, and M.W. Dewhirst, *A novel rodent mammary window of orthotopic breast cancer for intravital microscopy.* Microvascular Research, 2003. **65**(2): p. 109-117.
41. Pushkarsky, I., et al., *Elastomeric sensor surfaces for high-throughput single-cell force cytometry.* Nature Biomedical Engineering, 2018. **2**(2): p. 124.

CHAPTER 6:
BIOPHYSICAL CUES IN OTHER DISEASES

Authors: **Shirley X. Zhang**[1-3], Linan Liu[3,4], Henry Farhoodi[3,4], Weian Zhao[1-6]

Affiliations:

[1] Department of Biomedical Engineering, University of California-Irvine, Irvine, California, 92697, USA.

[2] Edwards Life Sciences Center for Advanced Cardiovascular Technology, University of California-Irvine, Irvine, California, 92697, USA.

[3] Sue and Bill Gross Stem Cell Research Center, 845 Health Sciences Road, University of California-Irvine, Irvine, California, 92697, USA.

[4] Department of Pharmaceutical Sciences, University of California-Irvine, Irvine, California, 92697, USA.

[5] Chao Family Comprehensive Cancer Center, University of California-Irvine, Irvine, California, 92697, USA.

[6] Department of Biological Chemistry, University of California-Irvine, Irvine, California, 92697, USA.

6.1 Introduction

Fibrosis is an underlying cause of nearly 45% of deaths in the developed world. It is caused by an imbalance in the deposition and degradation of extracellular matrix (ECM) proteins, leading to excess connective tissue that impairs normal cellular and organ functions. Fibrotic tissues are characterized also by their increased elastic modulus, making matrix stiffness a potential target for therapeutics.

Pathologic tissue fibrosis is caused by an excess deposition of extracellular matrix (ECM) which leads to impaired tissue function, organ failure, and death. Fibrosis can form as part of the normal healing process, where cells lay down ECM to close wounds and then resolve the fibrosis at a later stage to replace it with new functional tissue. Conversely, pathological fibrosis can form due to many disease processes such as infection or autoimmune responses. In this case, there is often an imbalance of the deposition and degradation of ECM, and the excess ECM remains, disrupting normal tissue function and sometimes leading to organ failure and death [1-3].

The potential origins and risk factors of pathologic tissue fibrosis are numerous, including but not limited to age, genetics, environmental factors (e.g. pollution, chemicals, radiation), injury, infections and personal habits like smoking. Most organ systems in the body can be affected by pathological fibrosis, and the underlying cause of mortality for many common disease states, including respiratory failure, heart disease, and liver failure, can be traced back to the formation of fibrotic scars within tissues. The severity of fibrosis has been shown to correlate directly with patient outcomes [4]. The development of fibrosis has also been implicated in the development of cancer and metastases [5-7]. Due to the ubiquity of fibrosis diseases and its strong links to mortality, the specific burden of this condition on society is incalculable. It is estimated that the cause of nearly 45% of deaths in the developed world can be traced back to fibroproliferative diseases [8]. Therefore, further research into the underlying mechanisms of fibrosis as well as potential treatments is paramount.

Despite its prevalence, currently there are very few, if any, specific treatments for pathologic tissue fibrosis. The most commonly investigated therapeutics are small molecules and growth factors such as transforming growth factor beta (TGF-β) blockers and hepatocyte growth factor (HGF), which have been shown in numerous animal studies to reduce tissue fibrosis [9-11]. These therapies work to treat fibrosis by acting on various inflammatory pathways, for example downregulating myofibroblast activity and decreasing overall ECM deposition. TGF-β pathway blockers such as pirfenidone and nintedanib have even been approved by the FDA for the treatment of fibrosis, however a significant number of patients in the trials suffered from severe side effects [12, 13], likely due to low specificity in the drug mechanisms that result in too much anti-inflammatory activity [14].

An alternative method to improve therapeutic specificity for treating fibrosis is to use the tissue stiffness itself as a target. A predominant feature of fibrosis, in addition to excess ECM deposition, is tissue stiffening. As the severity of fibrosis increases, so does the elastic modulus of the tissue [15]. Whereas healthy tissues from soft organs such as lung or liver usually maintain Young's moduli of below 1 kPa, fibrotic tissue could be many times stiffer [16, 17]. Targeting abnormally stiff tissue would thus directly target regions of fibrosis. Importantly, stiffness is a single, consistent biomarker across all tissue types that is already being used to diagnosis fibrosis in the clinic [18]. This is in contrast to most biochemical and molecular factors which can differ greatly throughout the body and have not reliably been used to diagnose fibrosis [19].

This chapter will discuss the development of an engineered mesenchymal stem cell system with a stiffness-sensing promoter that can activate the expression of a therapeutic specifically when in contact with fibrotic tissues. As discussed in previous chapters, therapeutics developed to target stiffness in one organ system could conceivably be easily translated to all other organ systems, becoming a platform technology.

6.2 MSCs in Fibrosis

Mesenchymal stem cells or mesenchymal stromal cells are multipotent, fibroblastoid-like cells that can be derived from many adult tissue sources [20]. MSCs have been used in numerous studies as a therapeutic for tissue fibrosis, and have shown favorable results in treating cardiac fibrosis [21, 22], pulmonary fibrosis [23, 24], and liver fibrosis [25, 26], with few adverse side effects. The specific mechanisms of how MSCs are beneficial for fibrosis remain unclear and require further investigation. MSCs also display an ability to home to sites of injury, including fibrosis [27], likely due to an upregulation of various cytokines and growth factors during injury and inflammation.

Another important feature of MSCs is their differential response to matrix stiffness. Cells within tissues experience very different degrees of ECM elasticity, ranging from very soft surroundings (such as those found in the brain and adipose tissue) to very stiff and rigid environments (such as those found within bones or at the bone surface). By recapitulating these different ECM elasticities *in vitro*, it was found that MSCs differentiate optimally into neurons, adipocytes, skeletal muscle cells or osteoblasts at elasticities that match the physiological ECM stiffness of their corresponding natural niche (shown as coloured lines, with peaks indicating maximal differentiation) [28]. As various studies have shown, substrate stiffness alone is enough to drive MSC differentiation, activating different promoters and gene expression [28-30]. For example, stiff substrates of over 25 kPa activates *RUNX2* and osteogenic differentiation. This makes it possible to use fibrotic tissue, which is stiffer than normal healthy tissue, as a trigger for directed gene expression for engineered therapeutics. Thus, MSCs an attractive option for targeting fibrosis and delivering therapeutics, using matrix stiffness as the main biomarker for targeting and activation.

6.3 Matrix Metalloproteinases

Matrix metalloproteinases (MMPs) are a large family of endopeptidases capable of degrading extracellular matrix proteins. MMPs are important in many normal physiological functions, such as embryonic development, wound healing, growth, and angiogenesis, since the turnover of ECM is essential for cell migration and function [31]. Of this family of MMPs, only a few members are collagenases capable of degrading interstitial collagen [32]. In particular, MMP-1 is an interstitial collagenase capable of degrading fibrillar collagen 1, the main component of pathological fibrosis [33, 34]. During pathologic fibrosis, the expression of MMPs including MMP-1 is downregulated, while that of their inhibitors is upregulated. This imbalance is part of the mechanism that contributes to sustained fibrosis [35].

Several studies have investigated using MMP-1 to treat tissue fibrosis, summarized below in Table 4 [34, 36-40]. While the literature provides encouraging data to support the effectiveness of MMP-1 as an antifibrotic agent, there are some concerns regarding the use of MMP-1 that need to be addressed in future studies. MMPs in general have a short half-life of bioactivity *in vivo*, on the order of hours [41], and effects may be improved by prolonging its lifespan. While MMP-1 has demonstrated benefits under pathophysiological conditions such as fibrosis, sustained overexpression of MMP-1 in healthy tissues could result in unwanted ECM degradation and organ damage [34, 36]. If these concerns could be addressed, MMP-1 remains an attractive therapeutic agent for the treatment of tissue fibrosis.

6.4 Engineering MSCs for Fibrosis

The potent anti-fibrotic properties of MMP-1 can be better specifically targeted to fibrotic regions of tissue by using stiffness-sensing MSCs as a delivery vessel. Mechano-responsive MSCs can sense and respond to increased stiffness and selectively deliver therapeutics *in situ* to dissolve excess fibrotic ECM and improve organ function. Although MSCs and MMP-1 have been shown to have therapeutic benefits for tissue fibrosis, both have deficits that, if addressed, could further improve fibrosis treatment. MSCs are capable of homing to injured organs and have few deleterious side effects, but have mostly undefined therapeutic mechanisms. MMP-1 has specific mechanisms and directly targets degradation of collagen 1 formed during fibrosis, however has short half-life of bioactivity and can be damaging to healthy tissue if off-target contact occurs. By engineering MMP-1 expression into MSCs, the enzyme can benefit from increased homing to the sites of fibrosis and increased period of bioactivity due to continuous expression and secretion by the cells. Further combining this with a YAP/TAZ promoter system further ensures that the release of MMP-1 is specific to stiff, fibrotic regions of tissues to minimize deleterious side effects.

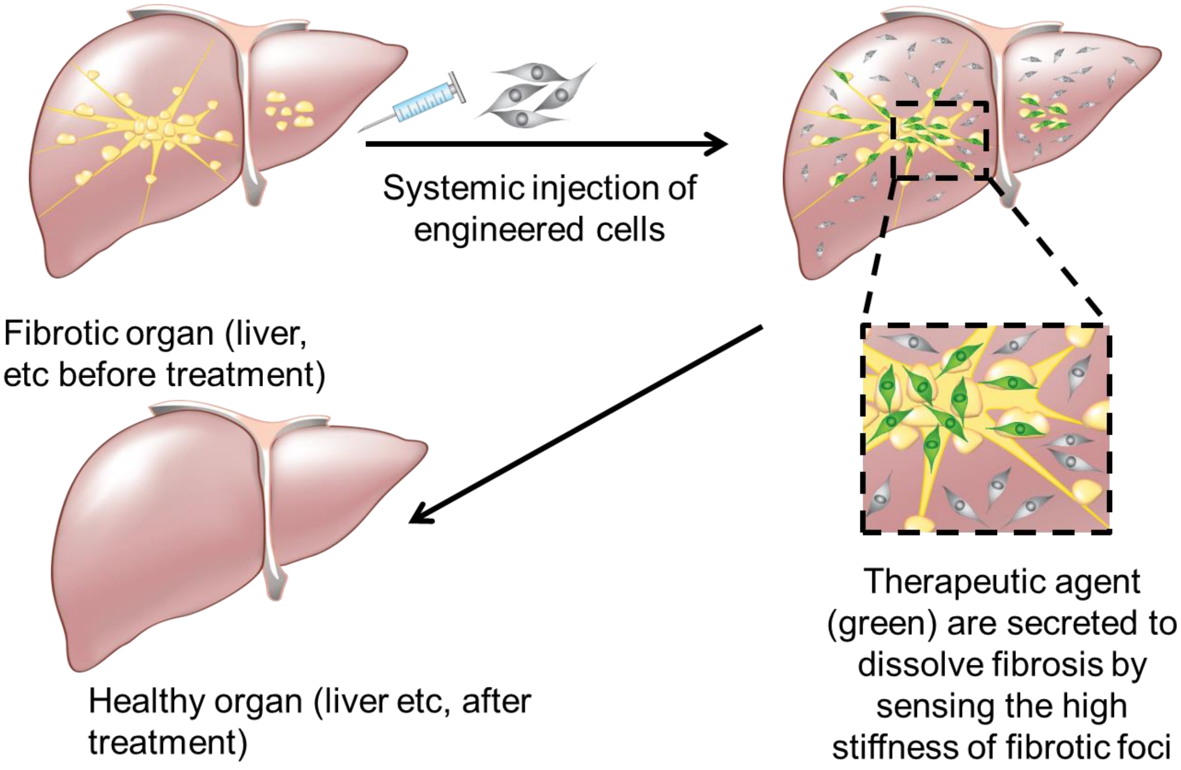

Fig. 6.1 Scheme of using mechano-responsive cells to treat liver fibrosis

Cells are only activated to secrete a therapeutic agent when in contact with stiff, fibrotic regions of the target organ.

YAP (Yes-Associated Protein) and TAZ (Transcriptional co-Activator with pdZ-binding motif) are transcriptional regulators upstream of promoters such as *RUNX2*. YAP/TAZ responds to a variety of mechanical cues, including ECM stiffness, cell geometry and stretching, and cell density and contact [42, 43]. Most importantly, high substrate rigidity causes YAP/TAZ to localize to the cell nucleus, where it can drive transcription. Low substrate rigidity causes YAP/TAZ to re-localize to the cytoplasm, implying this directed transcription can be reversible. YAP/TAZ promoter systems have already been developed to express reporters such as luciferase, depending on ECM stiffness [43]. For this study, YAP/TAZ promoters will be used to create a stiffness-sensing cell capable of expressing desired therapeutics when in contact with stiff, fibrotic tissue.

The goal is to use this endogenous ability of MSCs to selectively activate expression of MMP-1 when the cells are in contact with stiff substrates. This will allow the MMP-1 to be specifically released only when the MSCs are in contact with stiffer, fibrotic regions of tissue, which will not only potentially increase the length and potency of its therapeutic effects but also prevent off-target harm to healthy tissue architecture.

Though many stiffness-specific promoters have been identified to regulate gene expression in MSCs (e.g. *TUBB3, MYOD1, RUNX2*), in this study we will utilize YAP (Yes-associated protein) and TAZ (transcriptional coactivator with PDZ-binding motif, also known as WWTR1), which are bound to upstream transcriptional factors of the aforementioned promoters [43]. YAP/TAZ can activate expression of a desired gene. When the cell is in contact with soft substrates (<1kPa), YAP/TAZ remains in the cytoplasm and does not activate any gene transcription via the stiffness-sensing promoter. When the cell is in contact with stiffer substrates, YAP/TAZ localizes into the nucleus can activate the expression of a reporter or therapeutic gene of interest. For this study, human bone marrow MSCs will be engineered via lentiviral transduction to have this YAP/TAZ promoter or a constitutive promoter as a positive control.

To specifically target fibrotic regions of tissue, the engineered MSCs must be able to sense different substrate stiffness, and selectively activate the expression of a desired gene on high-stiffness substrates but not activate on low-stiffness substrates. To demonstrate this, MSCs were engineered with reporters green fluorescent protein (GFP) or Firefly luciferase (Luc) following the stiffness-sensing YAP/TAZ promoter.

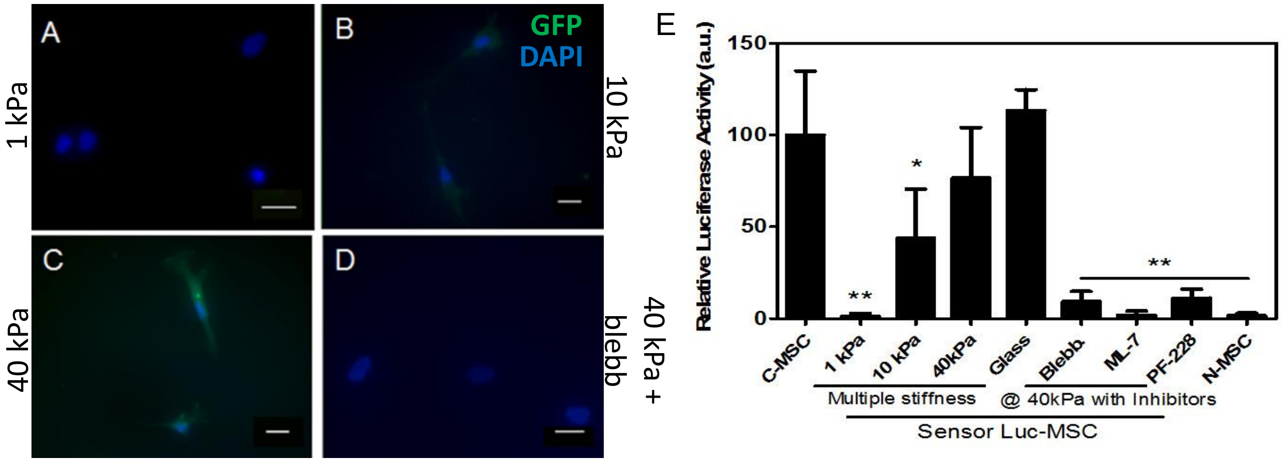

Fig. 6.2 Engineered MSCs have stiffness-specific gene expression *in vitro*

MSCs seeded on polyacrylamide gels with stiffness of **(A)** 1 kPa **(B)** 10 kPa **(C)** 40 kPa show expression of GFP only on stiffer (> 10 kPa) gels, which is inhibited by blebbistatin even on stiff gels **(D)**. **(E)** Engineered MSCs with Firefly luciferase show stiffness-specific expression of luciferase activity, with downregulated expression on soft gels and in the presence of mechanotransduction inhibitors. Scale bar = 25 µm. * $p < 0.05$, ** $p < 0.01$. Error bar: mean ± SD. C-MSC: constitutive positive control; N-MSC: native MSCs.

Sensor-GFP MSCs were plated on polyacrylamide gels of various stiffness, and were observed to only express GFP on stiffer gels over 10 kPa (Fig. 6.2B and 6.2C) but not on soft 1 kPa gels (Fig. 6.2A). The GFP expression was also stronger in the cells on the 40 kPa gels, as compared to the cells on the 10 kPa gels, demonstrating that increased stiffness also can increase gene expression levels. With the addition of blebbistatin, a myosin II inhibitor, MSCs on stiff gels did not express GFP (Fig. 6.2D), demonstrating that the expression is triggered by mechanotransduction. MSCs were also engineered to express Firefly luciferase after the stiffness-sensing promoter, and plated on polyacrylamide gels of various stiffness prior to measurement of luciferase activity (Fig. 6.2E). Luciferase activity in the sensor MSCs is significantly decreased on softer gels and in the presence of mechanotransduction inhibitors, while on stiff gels sensor MSCs displayed similar luciferase activity compared to constitutive expressing MSCs. These data show that engineered sensor MSCs are capable of selective expression of a desired gene when in contact with stiff substrates, but not on soft substrates, and that this expression is mediated by mechanotransduction.

MSCs were similarly engineered to express recombinant human MMP-1 after the stiffness-sensing promoter (MMP-MSCs). To verify the expression of the MMP-1 sequence, quantitative-PCR (qPCR) was performed on total mRNA collected from engineered 293T (Fig. 6.3A) and MSCs (Fig. 6.3B). All cells analyzed for this preliminary data were plated on tissue culture polystyrene (TCPS) which has a stiffness of ~1 GPa.

Compared to native cells, sensor cells had significantly higher MMP-1 mRNA expression for both 293T and MSCs. There was no significant difference in MMP-1 mRNA expression between sensor MSCs and constitutive expression MSCs on this stiff substrate (Fig. 6.3B), as also seen previously in (Fig. 6.2E) for luciferase activity in sensor and constitutive MSCs. However, there was a significant difference between sensor and constitutive 293T (Fig. 6.3A). This difference that is not seen in MSCs could be attributed to some inherent difference in the cell lines, and to the much higher expression levels seen in 293T which could have amplified any differences between groups.

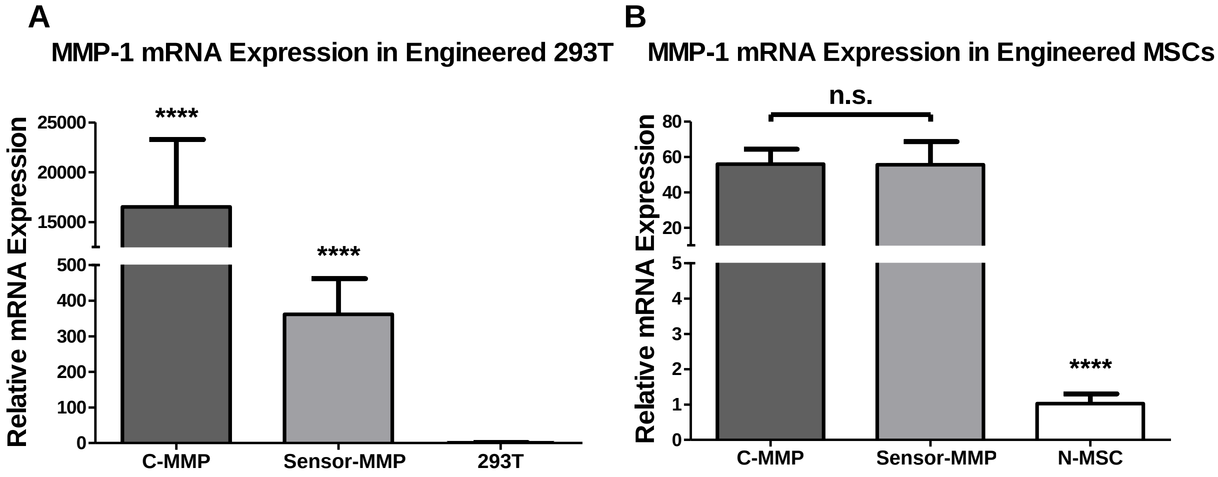

Fig. 6.3 Quantitative PCR analysis of MMP-1 mRNA expression levels

MMP-1 expression in **(A)** 293T and **(B)** MSCs on stiff substrate. Sensor cells expressed significantly higher levels of MMP-1 mRNA compared to native cells (normalized to 1 on this scale). **** $p < 0.001$, n.s. not significant. Error bar: mean ± SD. C-MSC: constitutive positive control; N-MSC: native MSCs.

To further characterize MMP-1 mRNA expression in the engineered cells, qPCR analysis will be repeated with cells seeded on polyacrylamide hydrogels of different stiffness. On softer substrates than the TCP used in the current data, sensor cells should have lower expression of MMP-1 mRNA. Constitutive cells should maintain high expression levels, and native cells low expression levels regardless of substrate stiffness. Future studies will also include the use of mechanotransduction inhibitors such as blebbistatin, ML-7 and PF228, which are expected to lower MMP-1 mRNA expression.

After validating MMP-1 mRNA expression from the engineered cells, it is also important to measure the amount of MMP-1 protein translated and secreted by the cells into the extracellular space. Enzyme-linked immunosorbent assay (ELISA) for MMP-1 was performed using conditioned cell culture medium collected from engineered 293T and MSCs plated on TCPS.

The amounts of MMP-1 detected in the conditioned medium for sensor cells were significantly higher for both 293T (Fig. 6.4A) and MSCs (Fig. 6.4B) when compared to native cells. The constitutive expressing controls secreted significantly higher levels of MMP-1 than the sensor cells.

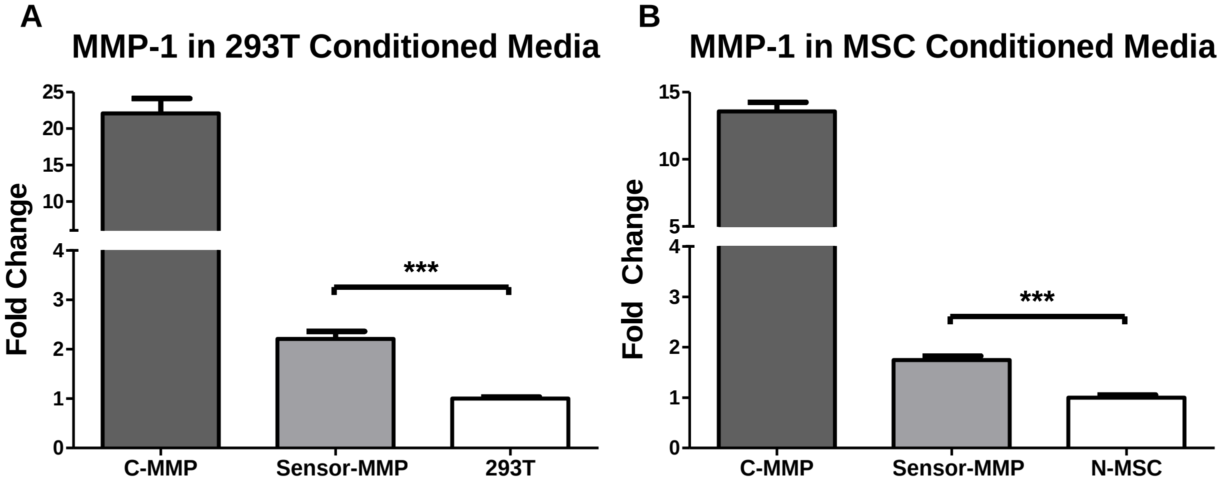

Fig. 6.4 ELISA analysis of secreted MMP-1 protein levels

Secreted MMP-1 in **(A)** 293T and **(B)** MSCs conditioned media, when cells are plated on stiff substrate. Sensor cells secreted significantly higher levels of MMP-1 compared to native cells (normalized to 1 on this scale). *** $p < 0.01$. Error bar: mean ± SD. C-MSC: constitutive positive control; N-MSC: native MSCs.

6.5 Establishing Murine Models of Liver Fibrosis

To fully study the interactions of engineered MMP-MSCs and fibrosis *in vivo*, a murine fibrosis model must first be established. The goal of this aim is to characterize the details of the animal model, as well as establish methods to detect the specific activities and effects of transplanted MSCs within the model. For this study we focus on liver fibrosis, which affects at a significant portion of the population but is often clinically silent until problems become too severe for conventional treatment [44]. Regression of liver fibrosis has also been strongly correlated to improved clinical outcomes [45]. The liver is also a structurally and functionally a relatively homogenous organ, and thus presents an optimal environment to study tissue fibrosis without confounding events such as mechanical forces or fluid flow.

The liver fibrosis model must demonstrate that fibrotic tissue is stiffer than healthy tissue, with sufficient difference in elastic modulus that the activation of the stiffness-sensing promoter (as characterized in Specific Aim 1) can differentiate between fibrotic and non-fibrotic tissue. For MMP-MSCs to be used successfully as a therapeutic, they must be successfully transplanted into and remain in the fibrotic liver, and specifically activate desired gene expression on fibrotic regions of the tissue that have higher stiffness.

Liver fibrosis was induced by direct intraperitoneal injections of carbon tetrachloride (CCl_4). CCl_4 acts by forming either CCl_3* radicals which bind to cell components such as nucleic acids and impairs crucial metabolic processes, or by forming CCl_3OO* radicals which cause lipid peroxidation [46]. The end result of this damage is hepatocyte apoptosis, necrosis and liver fibrosis.

Since the formation of fibrosis is in part mediated by an active immune response and inflammation [45], immunocompetent C57BL/6J were used for the liver fibrosis model. CCl_4

was injected twice per week for up to 8 weeks, and livers were collected for analysis every 2 weeks. Picrosirius red staining was used to visualize connective tissue in bright red (Fig. 6.5A). Fibrosis scoring can be assigned to each liver as follows: 0 = no fibrosis; 1 = fibrosis around portal areas, with no connections between portal areas; 2 = portal fibrosis with some bridging fibrosis between portal areas; 3 = portal fibrosis with many connecting bridges; 4 = cirrhosis [18].

Histology performed on both fibrotic and healthy livers show that over the course of 8 weeks of injections, the healthy livers do not show any development of fibrosis. However, for the fibrotic livers, fibrosis began forming around the portal regions by week 2 (fibrosis score 1), with some connections forming between portal regions by week 4 (fibrosis score 2), and many fibrotic connections and larger patches of connective tissue by week 8 (fibrosis score 3) (Fig. 6.5A). Quantification of many images from livers at each time point shows a steady increase of percent fibrosis area in the diseased livers, with no change over time in the healthy livers (Fig. 6.5B). Interestingly, after the last injection of CCl_4 at week 8, diseased livers were seen to exhibit some natural regeneration by week 14, which approached fibrosis levels seen at week 6. This suggests that given sufficient time after removal of the injury-inducing agent, livers can heal on their own to some degree, although it is unlikely that they will be able to completely revert to healthy liver levels.

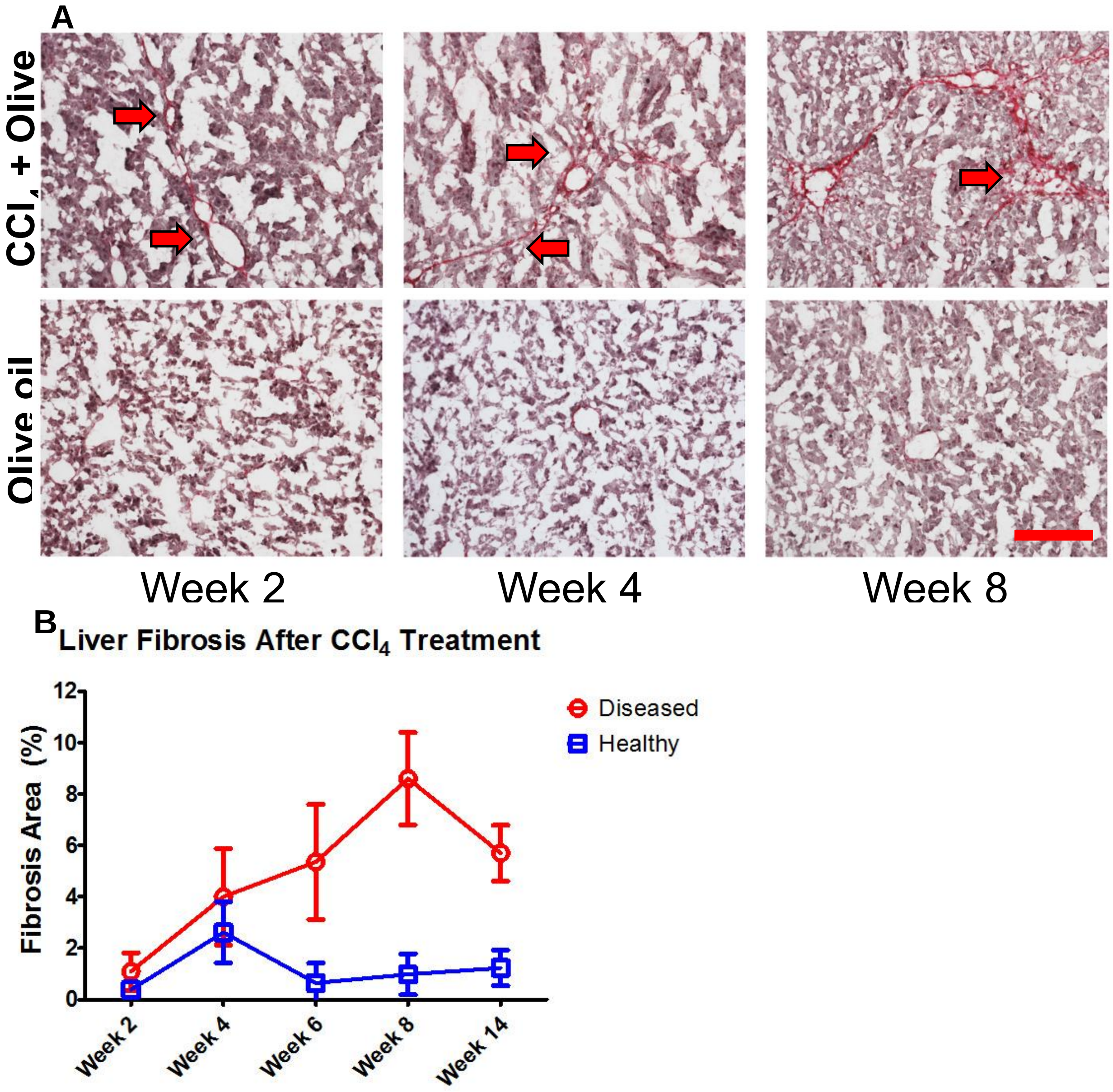

Fig.6.5 Histological staining and quantification of murine model of liver fibrosis induced by CCl_4

(A) Picrosirius red staining was performed to visualize collagen in bright red. Arrows added for emphasis. Scale bar = 100 µm. **(B)** Quantification of percent fibrosis area in stained liver sections for diseased and healthy mice. Difference between diseased and healthy for all time points $p < 0.01$.

Fibrotic livers must also have sufficiently increased stiffness in order to successfully activate the stiffness-sensing promoter in the engineered cells. This will allow the engineered cells to activate expression of a therapeutic agent on fibrotic liver, but remain quiescent on healthy liver to minimize potentially harmful side-effects. Atomic force microscopy (AFM) was used to measure the stiffness of fibrotic and diseased livers collected after 4 weeks of CCl_4+olive oil or olive oil only injections (Fig. 6.6). A representative scan of a liver from each group is shown in Fig. 6.6A, and plots of data points from multiple scans are shown in Fig. 6.6B. Overall, scans show that diseased livers are significantly stiffer than healthy livers. Diseased livers also show higher heterogeneity, likely due to scans on both fibrotic and non-fibrotic regions which could have very different modulus. Importantly, the average stiffness of the fibrotic livers was 11.7 kPa, which is over the 10 kPa stiffness threshold previously shown in Specific Aim 1 to activate expression from the stiffness-sensing YAP/TAZ promoter. The average stiffness of the healthy livers was under this threshold. This suggests that engineered cells using this stiffness-sensing promoter should be able to selectively activate on fibrotic livers but not healthy livers.

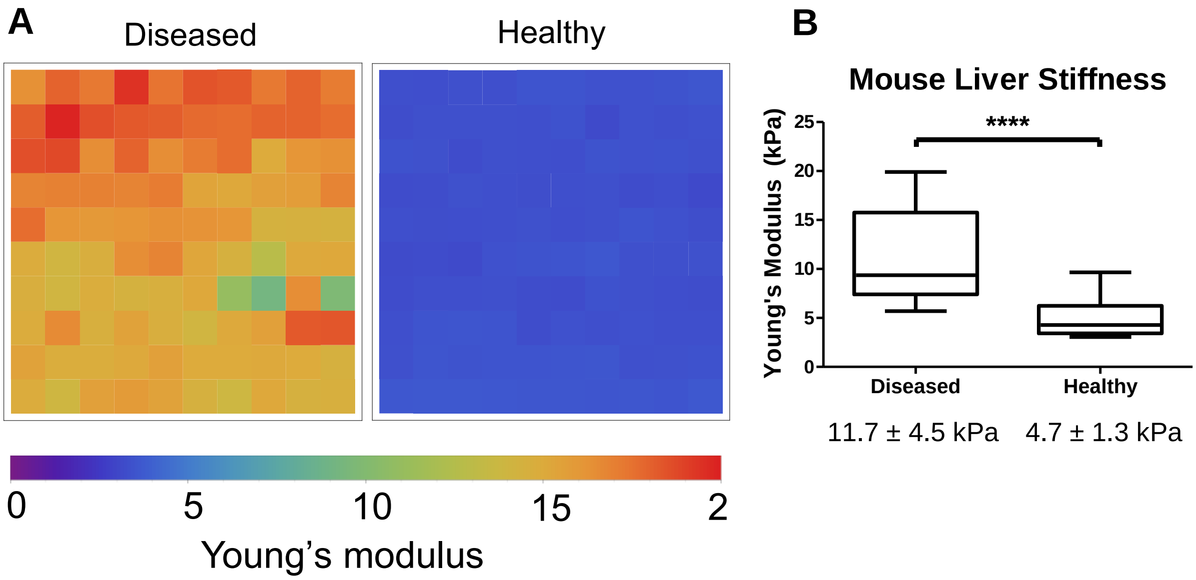

Fig. 6.6 Atomic force microscopy measurements on liver sections

After 4 weeks of CCl_4+olive oil or olive oil only injections, AFM analysis of healthy and diseased livers (A) Array plot of representative AFM scan. Scan size = 50 µm x 50 µm. (B) Plot of data points from multiple scans for each sample. **** $p < 0.001$

Once the murine model of liver fibrosis is established, the next step is to ensure that the engineered MSCs can reliably be delivered to and remain in the liver for a length of time that is sufficient to selectively activate gene expression via the stiffness-sensing promoter. To increase the localization of transplanted MSCs to the liver, the cells were delivered by direct injection into the hepatic portal vein.

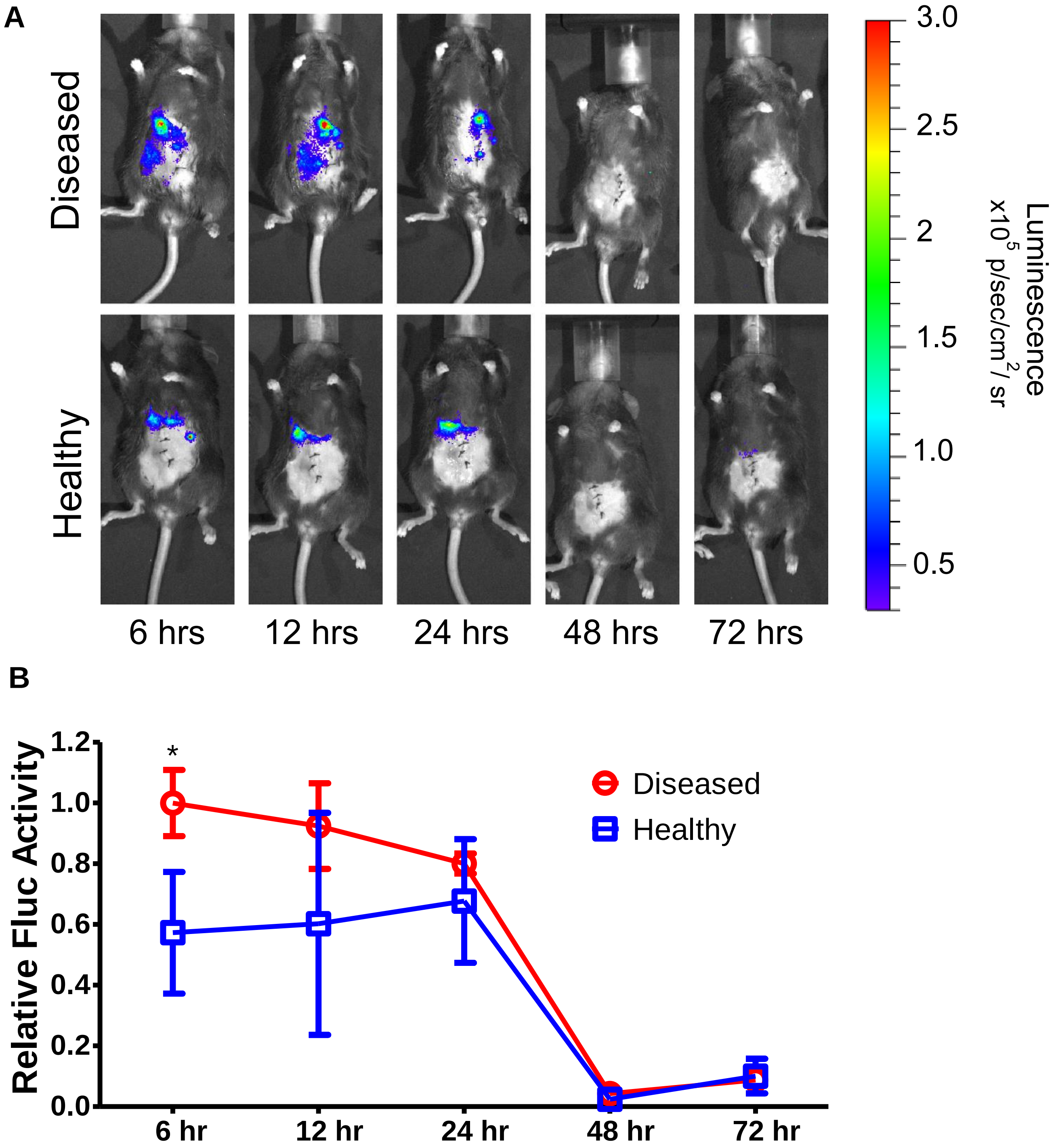

Fig. 6.7 Homing and retention of transplanted MSCs to liver

MSCs homing to fibrotic and healthy livers after portal vein injection (1x106 cells per mouse). MSCs were engineered to express Firefly luciferase (Fluc). Relative Fluc activity was measured at each of the time points (6 hrs, 12 hrs, 24 hrs, 48 hrs, and 72 hrs) using IVIS Lumina. Activity for each tested mouse image was normalized to control mouse images to negate background signals, then reported as a proportion as compared to the average diseased signal at 6 hrs, which is 1 on this scale. N = 3.

MSCs engineered with constitutive expression of Firefly luciferase were used to visualize homing and retention of the cells in the established murine liver fibrosis model (Fig. 6.7). $1x10^6$ luciferase-MSCs were injected per mouse, and the mice were imaged for bioluminescence at 6 hours, 12 hours, 24 hours, 48 hours and 72 hours after injections. Luciferase-MSCs seem to remain within the livers of both diseased and healthy mice for at least 24 hours, after which there is a sharp decline in the number of cells by 48 hours after injections. Quantification shows that there seems to be more MSCs retained in the fibrotic livers compared to the healthy ones (Fig. 6.7B), but there was no significant difference after 6 hours.

Another experiment of interest is using a different method of delivery for the MSCs. The current model of using portal vein injections was selected to maximize the number of cells that contact the liver, for the longest time possible, in order to better study the biophysical interactions between the liver tissue and the cells. However, if MSCs are in fact capable of homing to sites of tissue damage and fibrosis, then systemic injection of the cells through the tail vein should result in some significant portion of the cells in the liver, as well. Future studies will test this proposed MSC homing by first establishing the same liver fibrosis model, but replacing the portal vein injections with tail vein injections of $1x10^6$ luciferase-MSCs. The mice will be imaged at the same time points as before to detect *in vivo* luciferase activity in the liver. Since the MSCs now have to travel through systemic circulation to reach the liver, and since they may be trapped by the “lung barrier” [47], it is expected that the MSCs will take a longer time to reach the liver, and less cells will reach the liver and remain there in the end. The reduced number of cells could still be enough to provide therapeutic benefits to the liver, however, and this avenue of cell delivery is worth investigating as it is much less invasive than the surgeries required for portal vein injections. This experiment will also provide new insights into the homing abilities of MSCs to a fibrotic organ.

6.6 Engineered MSCs for Treating Fibrosis

The final goal of this project is to use engineered MMP-MSCs to successfully treat liver fibrosis in the previously established murine fibrosis model. Metrics for the effectiveness of the cell therapy include percent fibrosis area, tissue stiffness, and overall liver function before and after treatment. Sensor MMP-MSCs should be able to effectively improve those metrics, without incurring deleterious side effects.

MSCs with the stiffness-sensing promoter should only activate on stiff, fibrotic regions of the liver *in vivo*. To confirm this, sensor-MSCs with GFP following the stiffness-sensing promoter will be injected via the portal vein, and livers will be harvested at different time points (6 hours, 12 hours, 24 hours, 36 hours, 48 hours and 72 hours) for *ex vivo* analysis. Sections of liver samples will be taken and imaged by fluorescent microscope to detect the relative locations of MSCs and regions of collagen fibers. MSCs can be directly detected without the use of antibodies by labeling them with a far-red lipophilic dye prior to injections. Collagen can also be directly detected through the use of second harmonic generation (SHG) [48]. MSCs activated by stiffness should also be expressing GFP, which can be directly imaged as well. Fibrotic liver samples are expected to be positive for all three signals: lipophilic dye from MSCs, high SHG from collagen, and GFP, all co-localized with each other. Regions of diseased liver samples that are not highly fibrotic (low SHG signals) may have lipophilic dye from MSCs but should have less GFP from activated MSCs. Healthy liver samples are expected to be positive for lipophilic dye from MSCs, with low SHG from collagen and no GFP. At later time points (> 36 hours), MSCs may have cleared out from all liver samples and neither fibrotic nor healthy livers will show signals from the cells.

To confirm that engineered MMP-MSCs are successfully expressing MMP-1 after transplantation to the liver, a different strategy may be needed since MMP-1 is secreted from the cells into the extracellular space and does not remain within the cell for co-localization purposes like GFP. With proper fixation after organ harvest, it may still be possible to detect MMP-1 protein near MSCs and collagen regions using an MMP-1 antibody and immunohistochemistry. Total MMP-1 protein levels in the livers can also be quantified by homogenizing organ samples and performing ELISA.

To treat fibrosis by degrading excess collagen, MMP-MSCs must be able to secrete functional MMP-1 protein. Previously in Specific Aim 1, the secretion of MMP-1 from MMP-MSCs was confirmed, however the functional activity of the secreted protein was not measured. To do so, conditioned medium samples from sensor MMP-MSCs, constitutive expressing MMP-MSCs and native MSCs were collected. MMP-1 activity in the conditioned medium was measured by adding a 5-FAM/QXL™520 fluorescence resonance energy transfer (FRET) peptide substrate. When cleaved by MMP-1, the separation of 5-FAM and QXL results in fluorescence at 520 nm which can be measured by a plate reader. Because MMP-1 is one member of a large family of MMPs that have overlaps in substrate specificity, a monoclonal anti-MMP-1 antibody was used to isolate only this enzyme before addition of the FRET substrate.

Preliminary data using conditioned medium from cells plated on TCPS show that sensor-MMP-293T and MSCs secreted more functional MMP-1 and had significantly higher protein activity compared to native cells (Fig. 6.8). Constitutive expressing conditioned medium had much higher MMP-1 activity than both sensor and native cells. Importantly, sensor-MMP-MSCs displayed approximately 10 times the functional MMP-1 activity compared to native cells, higher than the ~2 fold increase in MMP-1 secretion between sensor-MMP-MSCs and native MSCs seen previously from ELISA data in Specific Aim 1. This suggests that even if total protein secretion level is low, the function of the enzyme itself could still be enough to make a significant difference therapeutically.

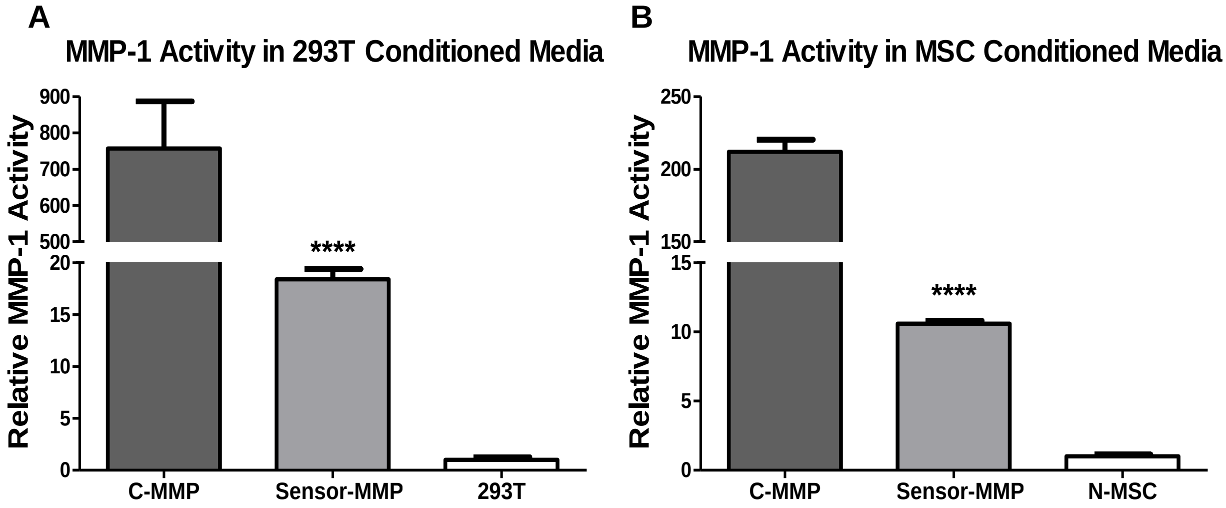

Fig. 6.8 Functional analysis of MMP-1 protein

Measured activity of MMP-1 in **(A)** 293T and **(B)** MSCs conditioned media on stiff substrate, using a FRET-based substrate. Sensor cells displayed higher levels of functional MMP-1 protein activity compared to native cells (normalized to 1 on this scale). **** $p < 0.001$. Error bar: mean ± SD. C-MSC: constitutive positive control; N-MSC: native MSCs.

It is important to show that sensor-MMP-MSCs can successfully treat fibrosis by improving the percent fibrosis area in the liver, decrease overall liver stiffness, and improve liver functions. An overview of the proposed fibrosis treatment study can be seen below: MMP-MSCs with constitutive expression will be used as a positive control. Native MSCs and PBS will be injected as negative and sham surgery controls, respectively.

Liver fibrosis will be established by injections of CCl_4 for 6 weeks, as described previously in Specific Aim 2. 1 x 10^6 cells in 200 µL PBS, or PBS alone will be injected on Day 0. Mice will be euthanized at 24 hours, 7 days and 4 weeks after injections, and livers and other major organs (lung, heart, spleen, brain, etc.) will be collected for further analysis. These time points are designed to provide a beginning time point with the most cells residing in the liver (24 hours), a short-term treatment time point when most cells have been cleared from the liver (7 days), and a long-term treatment time point to observe any lasting benefits of the cell therapy (4 weeks).

Liver samples will be analyzed for percent fibrosis area by histological staining for collagen with Masson's trichrome or picrosirius red. Liver stiffness will be measured by atomic force microscopy as well as elastography to cover both cellular and organ-wide scales. Compared to PBS and native MSCs, both constitutive and sensor MMP-MSCs should result in decreased fibrotic area and lower stiffness in the liver, although the timeframe of this effect will have to be determined. Liver function tests will be conducted using collected blood samples and measuring levels of liver enzymes such as alkaline phosphatase, alanine transaminase (ALT), and aspartate transaminase (AST) with ELISA. Liver damage would be reflected in higher levels of these enzymes in the blood samples. MMP-MSCs, in addition to decreasing the amount of fibrosis in the liver, will hopefully also improve overall liver function.

High expression of MMP-1 from engineered MSCs may be able to degrade excess collagen and improve overall fibrosis, but there are potentially harmful side-effects if the cell therapy is not targeted and could result in overzealous degradation of healthy matrix architecture. It is hoped that the sensor MMP-MSCs will have improved targeting to only fibrotic tissue, which would spare any normally healthy tissue. Preliminary homing data suggest that after portal vein injection, MSCs mostly remain within the liver and have not been detected elsewhere (See Specific Aim 2). However, some tissues in the body are naturally over 10 kPa, such as muscle and bone [21], and thus over the threshold at which the stiffness-sensor activates, and it is possible that the transplanted cells could migrate to other organs under certain conditions. To detect for this, tissue samples from other organs will also be collected during the treatment study and analyzed to determine where the transplanted cells may have gone outside of the liver. Since the MSCs are derived from human bone marrow, it is possible to detect the transplanted cells using Alu-PCR. Histological analysis such as hematoxylin and eosin staining could also be used to examine samples from other major organs to look for signs of tissue damage caused by excess ECM degradation and cell slippage.

6.7 Discussion

Fibrosis is a deadly, but often overlooked condition which is at the root of many major health problems and can be found in almost every organ system. Current treatment options available for fibrosis patients are very limited, with non-specific mechanisms that lead to serious side-effects. Whereas many current therapies can slow the progression of the disease, it is unclear whether treatment can reverse advanced fibrosis and improve organ function. In this proposal, a plan is presented to engineer a mechano-responsive mesenchymal stem cell system that can directly target fibrotic tissue and degrade the excess collagen using MMP-1 as the therapeutic agent. The use of a stiffness-sensing promoter system can greatly increase the specific targeting of fibrotic tissue, and potentially reduce deleterious side-effects that could result from off-target release of antifibrotic agents on healthy tissues.

In vitro experiments will have to be conducted on tunable hydrogels with different stiffnesses to verify that there are lower secretion levels on softer gels for the sensor cells, and also lower secretion levels in the presence of mechanotransduction inhibitors. In contrast, there should be no difference in activity for the constitutive expression control cells between different substrate stiffnesses.

The disparity between the high MMP-1 mRNA expression and the much lower (although statistically significant) secreted protein levels in the sensor cells suggests that although the mRNA for MMP-1 is being transcribed, the protein itself is either not being fully translated or secreted from the cells. Since the exact amount of MMP-1 secretion required to make a therapeutic difference for fibrosis treatment is unknown, it is still possible that the current ~2 fold increase of MMP-1 in the sensor MSCs compared to native MSCs is enough to improve fibrosis outcomes. However, in future work the sensor-MMP construct will be re-engineered to potentially increase MMP-1 secretion levels. The current MMP-1 construct is a fused protein, with the MMP-1 sequence directly attached to a turbo GFP sequence. While this would facilitate fluorescent detection of MMP-1, the fluorescent protein is not necessary for the function of the enzyme and the combined size of the fusion construct may be too large and hindering the translation or secretion of a complete MMP-1 protein. A new construct will be made which separates the MMP-1 and reporter sequences, and aforementioned experiments will be repeated using the new construct to compare expression and secretion levels.

For future *in vivo* studies, mice will be given cells as treatment after 6 weeks of CCl_4 injections. This is due to a sharp drop in animal survival between week 6 and week 8, and the invasive nature of the portal vein injections used to increase cell transplantation to the liver, which further decreases animal survival. Differences in liver fibrosis area and stiffness at week 6 should still be sufficient to demonstrate treatment efficacy. Further study using a larger cohort of animals will be conducted to confirm this trend and achieve better statistical significance between the two groups. An additional time point at 36 hours will also help elucidate the clearing out of MSCs that occurred between 24 and 48 hours. A potential justification for why there were more MSCs in the fibrotic livers could be that MSCs have natural homing to sites of inflammation and injury, which in the case of liver fibrosis can both initially recruit more MSCs to the liver and aid in their retention over time [25].

The relatively short retention time of the MSCs *in vivo* (< 2 days) could be due to the rejection of human transplanted cells by a competent murine immune system. Unfortunately, while immunocompromised mice would allow for MSCs to remain within the liver for a longer period of time, the formation of fibrosis may not be as robust without an active immune system. If after further study, this time frame is too short for the transplanted MSCs to have a beneficial therapeutic effect, there are several potential options to explore. One is to try and establish a liver fibrosis model in a strain of immunocompromised or partially immunocompromised mice. While the fibrosis formation may not be as robust as in immunocompetent mice, there may be enough of a fibrotic response to result in a sufficient difference in tissue stiffness. Another option is to use mouse-derived MSCs instead, which would avoid most of the rejection of the cells by the immune system.

Further homing and retention studies will be performed using sensor-MSCs also expressing Firefly luciferase. It is expected that after cell engraftment in the liver tissue, luciferase activity will be present in the stiffer, fibrotic livers but not on the softer, healthy livers due to the stiffness-specific activation of luciferase expression. Lipophilic dye (DiR) will be used to label the MSCs prior to injection, and the mice will also be imaged for far-red fluorescence under IVIS Lumina. This will serve as a quantification for the total amount of cells in the livers over time, and the amount of activated sensor-MSCs from the luciferase signal can be normalized to this value at each time point. The length of cell retention in the livers is expected to remain the same as the previous experiment using constitutive expression.

Future studies will also potentially explore different organ targets for fibrosis therapy, for example pulmonary fibrosis, cardiac fibrosis and atherosclerosis. Because matrix stiffness is a consistent biomarker found across all fibrotic tissue, the technologies developed in the current study should translate easily to other tissue types. Different therapeutic agents will also be investigated.

6.8 Materials and Methods

Cell Engineering

Sequences of interest from the following plasmids were used in this study: eGFP sequence from pUCBB-eGFP (Addgene #32548), Firefly luciferase sequence from pcDNA3.1(+)/Luc2=tdT (Addgene #32904), YAP/TAZ promoter sequence from 8xGTIIC-luciferase (Addgene #34615), CMV promoter and human recombinant MMP-1 sequence with turbo GFP from NM_002421 (OriGene). All sequences of interest were cloned into the promoterless lentiviral transfer vector LV-PL4 (GenTarget). MSCs were transduced by packaging all lentiviral constructs in pMD2.G (Addgene #12259), pRSV-Rev (Addgene #12253) and pMDLg/pRRE (Addgene #12251) as lentiviral vectors in 293T-LV cells using Lipofectamine® LTX and PLUS™ Reagents (Life Technologies). Cells were transduced with LVs by incubating virions in a culture medium containing 100 μg/mL protamine sulfate (Sigma). Cells transduced with LVs containing empty vectors (EV) were used as a control. After selection with medium containing 10 μg/mL Puromycin (MP Biomedicals), fluorescent protein-expressing cells were visualized for fluorescent protein expression using fluorescence microscopy to confirm transduction efficiency.

Tunable polyacrylamide hydrogels

Polyacrylamide hydrogels of different stiffness (~1 kPa, ~10 kPa and ~40 kPa) were synthesized as previously described in the literature [49, 50]. The stiffness of the hydrogel was adjusted by changing the ratio of acrylamide and bis-acrylamide. Hydrogels were formed on glass coverslips, which were then placed into 24-well plates and sterilized by x-ray prior to cell seeding and culture. For fluorescent analysis, DAPI (50 μg/mL, Life

Technologies) in PBS was added to the cells before mounting with Fluoromount-G (Southern Biotech). For bioluminescent analysis, D-Luciferin (150 μg/ml in PBS, Perkin Elmer) was added to the cells, and the luminescence was measured by imaging in Lumina IVIS. After seeding, some cells were also treated with blebbistatin (myosin II inhibitor, 50 uM), ML-7 (myosin light-chain kinase inhibitor, 10uM), or PF228 (focal adhesion kinase inhibitor, 20 uM).

Quantitative PCR

Total RNA extraction was performed on confluent T175 flasks of cells using TRIzol (Invitrogen) following manufacturer's instructions. Samples were treated with DNase I (Thermo Fisher) to remove DNA contamination. cDNA synthesis was performed with Oligo(dT) (Invitrogen) primed SuperScript® III RNase H Reverse Transcriptase (Invitrogen) and Power SYBR® Master Mix (Life Technologies). RT qPCR was performed on quadruplicates on an Applied Biosystems® ViiA™ 7 Real-Time PCR System and data were analyzed with ViiATM 7 Software v1.2. Relative gene expression levels were normalized to the endogenous gene GAPDH. Primers used in this study: GAPDH-C-F1 (5' – CTC CTG CAC CAC CAA CTG CT – 3'), GAPDH-C-R2 (5' – GGG CCA TCC ACA GTC TTC TG – 3'), MMP_fwd1 (5' – GGA GTG CCT GAT GTG GCT CA – 3'), MMP_rev1 (5' – GGT CCA CAT CTG CTC TTG GC – 3').

Enzyme-linked immunosorbent assay (ELISA)

ELISA was performed using Human MMP-1 ELISA Kit for serum, plasma, cell culture supernatant and urine (Sigma) following the manufacturer's directions for sandwich ELISA. Cell culture medium was collected from confluent T175 flasks of cells, and concentrated via

Amicon 10kDa centrifuge filter units (EMD Millipore) by 30 minutes of centrifugation at at 4000 x g and 4°C. 100 µL of concentrated samples or recombinant MMP-1 protein standards were added to the antibody-coated ELISA plate. Signal detection was colorimetric and measured at 450 nm by plate reader (BioTek Synergy HT). All samples were performed in triplicate.

Functional MMP assay

Functional MMP-1 activity was detected using SensoLyte® Plus 520 MMP-1 Assay Kit (AnaSpec), following manufacturer's instructions. Cell culture medium was collected from confluent T175 flasks of cells, and concentrated via Amicon 10kDa centrifuge filter units (EMD Millipore) by 30 minutes of centrifugation at at 4000 x g and 4°C. 100 µL of concentrated samples or recombinant MMP-1 protein standards were added to the antibody-coated plate. MMP-1 was functionally activated by addition of 100 mM APMA. MMP-1 activity was detected by addition of 5-FAM/QXL™ peptide 520 substrate. Kinetic fluorescent readings were taken at Ex/Em = 490 nm/520 nm every 5 minutes for the first 60 minutes, then every 15 minutes for the following 16 hours.

Murine liver fibrosis model

A murine liver fibrosis model was established using carbon tetrachloride (CCl_4) in 6-week-old female C57BL/6J mice (Jackson Laboratory), following dosage guidelines previously used in literature [51, 52]. Mice were weighed weekly, and injected intraperitoneally with 1 mL CCl_4 per 1 kg body weight twice per week for up to 8 weeks. The CCl_4 was diluted in pure olive oil for a total injection volume of 100 µL per injection. The control group received 100 µL of olive oil only with the same injection schedule.

All animal experiments and procedures were performed after the approval from the University of California, Irvine (UCI) Institution of Animal Care and Use Committee (IACUC protocol number 2012-3062) and conducted according to the Animal Welfare Assurance (#A3416.01).

MSC transplantation and in vivo *imaging*

Portal vein injections were performed by surgically exposing the hepatic portal vein, and injecting 1x106 MSCs in PBS per mouse through a 2 in. 33 gauge needle, point style 2 (Hamilton). Mice were anesthetized by ketamine and xylazine for the duration of the procedure. After suturing, mice were given 1 mL/kg ketaprofen and closely monitored post-operation.

After cell transplantation, mice were imaged at time points including 6 hours, 12 hours, 24 hours, 36 hours, 48 hours, 72 hours and 7 days post-operation. For bioluminescence from engineered luciferase-MSCs, *in vivo* luciferase activity was measured using IVIS Lumina 10 minutes after intraperitoneal injection of D-luciferin (150 mg/kg in DPBS). Mice were also directly imaged in IVIS Lumina for fluorescence using ICG filter from MSCs labeled with a far-red lipophilic dye (DiR, Perkin Elmer).

Histology and quantification

Livers were collected from fibrotic and healthy mice and was either flash frozen in Tissue-Tek® O.C.T™ Compound (Sakura Finetek) or fixed in 4% paraformaldehyde then submerged in 30% sucrose solution overnight. 10 μm sections were taken by cryostat for staining.

Picrosirius red staining was performed to visualize collagen. Direct Red 80 (Sigma) was dissolved in picric acid (Sigma, 1.3% in water) at a concentration of 0.5g/500 mL. Tissue sections were stained with Weigert's hematoxylin (Sigma) for 8 minutes to visualize nuclei, then washed under tap water to remove excess dye. Slides were then stained in picrosirius red solution for 1 hour at room temperature, then washed in an acidified water solution (5 mL glacial acetic acid in 1 L distilled water). Slides were dehydrated in three changes of 100% ethanol, cleared in Histoclear (Thermo Fisher) before mounting with Permount (Thermo Fisher). The resulting slides have collagen visualized in bright red, with nuclei in brown and the remaining tissue in a pale brown-red.

Percent fibrosis areas were quantified using images taken by an Olympus slide scanning microscope. 30 randomly selected images from each liver section were processed in ImageJ with color thresholding to calculate fibrotic area as a percentage of total tissue area.

Atomic force microscopy

Livers were collected from diseased and healthy mice after 4 week of CCl_4+olive oil or olive oil only injections, and kept in ice-cold Ringer solution (Thermo Fisher). Liver samples were cut into 500 μm thick slices using a rat heart slicer matrix (Zivic Instruments) and mounted to a 60 mm plastic petri dish using epoxy glue (Devon). Samples were measured using Bruker

BioScope Catalyst Atomic Force/ Zeiss LSM5 Confocal Fluorescence Microscope using contact mode in fluid, using MLCT C Triangular cantilevers (spring constant = 0.01 N/m, Bruker). Data points were taken 5 μm apart on 50 x 50 μm scans. Data was analyzed with Nanoscope Analysis v1.5 software, using a Sneddon conical model with Poisson ratio 0.5 [53].

6.9 Supplemental Figures and Tables

Table 4: Studies using MMP-1 to treat tissue fibrosis

Animal	**Target Organ**	**Disease Model**	**Delivery of MMP-1**	**Results**
Rat	Liver	TAA	Adenovirus	Decreased fibrosis and expression of collagen I, increased liver weight and hepatocyte proliferation
Mouse	Heart	Aortic band	Transgenic	Decreased fibrosis, prevented LV dilation, preserved cardiac function
Rat	Heart	Artery ligation	Gelatin microspheres	Decreased fibrosis, prevented LV dilation, preserved cardiac function
Mouse	Heart	Atherosclerosis	Transgenic	Decreased lesion size, reduced fibrillary collagen, no plaque ruptures
Mouse	Aorta	Laceration	Injection of protein	Decreased connective collagen, improved muscle scarring
Mouse	Kidney	STZ diabetes	Gelatin microspheres	Decreased fibrosis, fibrillary collagen, and blood urea nitrogen

6.10 References

1. Usunier, B., et al., *Management of fibrosis: the mesenchymal stromal cells breakthrough.* Stem Cells Int, 2014. **2014**: p. 340257.
2. Wynn, T.A., *Cellular and molecular mechanisms of fibrosis.* J Pathol, 2008. **214**(2): p. 199-210.
3. Wynn, T.A. and T.R. Ramalingam, *Mechanisms of fibrosis: therapeutic translation for fibrotic disease.* Nat Med, 2012. **18**(7): p. 1028-40.
4. Gulati, A., et al., *Association of fibrosis with mortality and sudden cardiac death in patients with nonischemic dilated cardiomyopathy.* JAMA, 2013. **309**(9): p. 896-908.
5. Cox, T.R. and J.T. Erler, *Remodeling and homeostasis of the extracellular matrix: implications for fibrotic diseases and cancer.* Dis Model Mech, 2011. **4**(2): p. 165-78.
6. Cox, T.R., et al., *LOX-mediated collagen crosslinking is responsible for fibrosis-enhanced metastasis.* Cancer Res, 2013. **73**(6): p. 1721-32.
7. Zhang, D.Y. and S.L. Friedman, *Fibrosis-dependent mechanisms of hepatocarcinogenesis.* Hepatology, 2012. **56**(2): p. 769-75.
8. Wynn, T.A., *Common and unique mechanisms regulate fibrosis in various fibroproliferative diseases.* J Clin Invest, 2007. **117**(3): p. 524-9.
9. Ueki, T., et al., *Hepatocyte growth factor gene therapy of liver cirrhosis in rats.* Nature Medicine, 1999. **5**(226-230).
10. Edgley, A.J., H. Krum, and D.J. Kelly, *Targeting fibrosis for the treatment of heart failure: a role for transforming growth factor-beta.* Cardiovasc Ther, 2012. **30**(1): p. e30-40.
11. Taniyama, Y., Morishita, R., Nakagami, H., Moriguchi, A., Sakonjo, H., Matsumoto, K., Nakamura, T., Higaki, J. and Ogihara, T., *Potential contribution of a novel antifibrotic factor, hepatocyte growth factor, to prevention of myocardial fibrosis by angiotensin II blockade in cardiomyopathic hamsters.* Circulation, 2000. **102**(2): p. 246-252.
12. Richeldi, L. and R.M. du Bois, *Pirfenidone in idiopathic pulmonary fibrosis: the CAPACITY program.* Expert Rev Respir Med, 2011. **5**(4): p. 473-81.
13. Richeldi, L., et al., *Efficacy and safety of nintedanib in idiopathic pulmonary fibrosis.* N Engl J Med, 2014. **370**(22): p. 2071-82.
14. Zeisberg, M.a.K., R, *Cellular mechanisms of tissue fibrosis. 1. Common and organ-specific mechanisms associated with tissue fibrosis.* American Journal of Physiology-Cell Physiology, 2013. **304**(3): p. C216-C225.
15. Yeh, W.C., Li, P.C., Jeng, Y.M., Hsu, H.C., Kuo, P.L., Li, M.L., Yang, P.M. and Lee, P.H., *Elastic modulus measurements of human liver and correlation with pathology.* Ultrasound in medicine & biology, 2002. **28**(4): p. 467-474.
16. Wells, R.G. and D.E. Discher, *Matrix Elasticity, Cytoskeletal Tension, and TGF-β: The Insoluble and Soluble Meet.* Science Signaling, 2008. **1**(10): p. pe13.
17. Hinz, B., *Tissue Stiffness, Latent TGF-β1 Activation, and Mechanical Signal Transduction: Implications for the Pathogenesis and Treatment of Fibrosis.* Current rheumatology reports, 2009. **11**(2): p. 120-126.
18. Ziol, M., et al., *Noninvasive assessment of liver fibrosis by measurement of stiffness in patients with chronic hepatitis C.* Hepatology, 2005. **41**(1): p. 48-54.
19. Beyer, C., Oliver Distler, and Jörg HW Distler., *Biomarkers of Fibrosis*, in *Scleroderma*. 2012, Springer US. p. 283-290.

20. Phinney, D.G. and D.J. Prockop, *Concise review: mesenchymal stem/multipotent stromal cells: the state of transdifferentiation and modes of tissue repair--current views.* Stem Cells, 2007. **25**(11): p. 2896-902.
21. Berry, M.F., Engler, A.J., Woo, Y.J., Pirolli, T.J., Bish, L.T., Jayasankar, V., Morine, K.J., Gardner, T.J., Discher, D.E. and Sweeney, H.L., *Mesenchymal stem cell injection after myocardial infarction improves myocardial compliance.* American Journal of Physiology-Heart and Circulatory Physiology, 2006. **290**(6): p. H2196-H2203.
22. Elnakish, M.T., P. Kuppusamy, and M. Khan, *Stem cell transplantation as a therapy for cardiac fibrosis.* J Pathol, 2013. **229**(2): p. 347-54.
23. Toonkel, R.L., et al., *Mesenchymal stem cells and idiopathic pulmonary fibrosis. Potential for clinical testing.* Am J Respir Crit Care Med, 2013. **188**(2): p. 133-40.
24. Moodley, Y., et al., *Human umbilical cord mesenchymal stem cells reduce fibrosis of bleomycin-induced lung injury.* Am J Pathol, 2009. **175**(1): p. 303-13.
25. Abdel Aziz, M.T., et al., *Therapeutic potential of bone marrow-derived mesenchymal stem cells on experimental liver fibrosis.* Clin Biochem, 2007. **40**(12): p. 893-9.
26. Dai, L.J., et al., *The therapeutic potential of bone marrow-derived mesenchymal stem cells on hepatic cirrhosis.* Stem Cell Res, 2009. **2**(1): p. 16-25.
27. Berardis, S., et al., *Use of mesenchymal stem cells to treat liver fibrosis: current situation and future prospects.* World J Gastroenterol, 2015. **21**(3): p. 742-58.
28. Halder, G., S. Dupont, and S. Piccolo, *Transduction of mechanical and cytoskeletal cues by YAP and TAZ.* Nature Reviews Molecular Cell Biology, 2012. **13**(9): p. 591-600.
29. Engler, A.J., et al., *Matrix elasticity directs stem cell lineage specification.* Cell, 2006. **126**(4): p. 677-89.
30. Park, J.S., et al., *The effect of matrix stiffness on the differentiation of mesenchymal stem cells in response to TGF-beta.* Biomaterials, 2011. **32**(16): p. 3921-30.
31. Nagase, H.a.W., J.F., *Matrix metalloproteinases.* Journal of Biological chemistry, 1999. **274**(31): p. 21491-21494.
32. Nagase, H., Visse, R. and Murphy, G., *Structure and function of matrix metalloproteinases and TIMPs.* Cardiovascular Research, 2006. **69**(3): p. 562-573.
33. Querejeta, R., et al., *Increased collagen type I synthesis in patients with heart failure of hypertensive origin: relation to myocardial fibrosis.* Circulation, 2004. **110**(10): p. 1263-8.
34. Lin, X., Jo, H., Ishii, T.M., Fujita, M., Fu, M., Tambara, K., Yamamoto, M., Tabata, Y., Komeda, M. and Matsuoka, S., *Controlled release of matrix metalloproteinase-1 plasmid DNA prevents left ventricular remodeling in chronic myocardial infarction of rats.* Circulation Journal, 2009. **73**(12): p. 2315-2321.
35. Iimuro, Y. and D.A. Brenner, *Matrix metalloproteinase gene delivery for liver fibrosis.* Pharm Res, 2008. **25**(2): p. 249-58.
36. Iimuro, Y., et al., *Delivery of matrix metalloproteinase-1 attenuates established liver fibrosis in the rat.* Gastroenterology, 2003. **124**(2): p. 445-58.
37. Foronjy, R.F., Sun, J., Lemaitre, V. & D'Armiento, J. M. , *Transgenic expression of matrix metalloproteinase-1 inhibits myocardial fibrosis and prevents the transition to heart failure in a pressure overload mouse model.* Hypertension Research, 2008. **31**: p. 725-735.
38. Lemaître, V., O'Byrne, T.K., Borczuk, A.C., Okada, Y., Tall, A.R. and D'Armiento, J., *ApoE knockout mice expressing human matrix metalloproteinase-1 in macrophages have less*

advanced atherosclerosis. The Journal of clinical investigation, 2001. **107**(10): p. 1227-1234.

39. Kaar, J.L., et al., *Matrix metalloproteinase-1 treatment of muscle fibrosis.* Acta Biomater, 2008. **4**(5): p. 1411-20.
40. Aoyama, T., Yamamoto, S., Kanematsu, A., Ogawa, O. & Tabata, Y. , *Local delivery of matrix metalloproteinase gene prevents the onset of renal sclerosis in streptozotocin-induced diabetic mice.* Tissue Engineering, 2003. **9**(6): p. 1289-1299.
41. Reunanen, N., Li, S.P., Ahonen, M., Foschi, M., Han, J. and Kähäri, V.M., , *Activation of p38α MAPK enhances collagenase-1 (matrix metalloproteinase (MMP)-1) and stromelysin-1 (MMP-3) expression by mRNA stabilization.* Journal of Biological Chemistry, 2002. **277**(35): p. 32360-32368.
42. Low, B.C., Pan, C.Q., Shivashankar, G.V., Bershadsky, A., Sudol, M. and Sheetz, M., *YAP/TAZ as mechanosensors and mechanotransducers in regulating organ size and tumor growth.* FEBS letters, 2014. **588**(16): p. 2663-2670.
43. Dupont, S., et al., *Role of YAP/TAZ in mechanotransduction.* Nature, 2011. **474**(7350): p. 179-83.
44. Lim, Y.S. and W.R. Kim, *The global impact of hepatic fibrosis and end-stage liver disease.* Clin Liver Dis, 2008. **12**(4): p. 733-46, vii.
45. Friedman, S.L., *Mechanisms of hepatic fibrogenesis.* Gastroenterology, 2008. **134**(6): p. 1655-69.
46. Weber, L.W., M. Boll, and A. Stampfl, *Hepatotoxicity and mechanism of action of haloalkanes: carbon tetrachloride as a toxicological model.* Crit Rev Toxicol, 2003. **33**(2): p. 105-36.
47. Schrepfer, S., et al., *Stem cell transplantation: the lung barrier.* Transplant Proc, 2007. **39**(2): p. 573-6.
48. Bianchini, P. and A. Diaspro, *Three-dimensional (3D) backward and forward second harmonic generation (SHG) microscopy of biological tissues.* J Biophotonics, 2008. **1**(6): p. 443-50.
49. Tse, J.R. and A.J. Engler, *Preparation of Hydrogel Substrates with Tunable Mechanical Properties*, in *Current Protocols in Cell Biology*. 2001, John Wiley & Sons, Inc.
50. Wang, Y. and R. Pelham, *Preparation of a flexible, porous polyacrylamide substrate for mechanical studies of cultured cells.* Methods in enzymology, 1998. **298**: p. 489-496.
51. Zhang, D., M. Jiang, and D. Miao, *Transplanted human amniotic membrane-derived mesenchymal stem cells ameliorate carbon tetrachloride-induced liver cirrhosis in mouse.* PLoS One, 2011. **6**(2): p. e16789.
52. Sudo, K., et al., *Lack of tumor necrosis factor receptor type 1 inhibits liver fibrosis induced by carbon tetrachloride in mice.* Cytokine, 2005. **29**(5): p. 236-44.
53. Gang, Z., et al., *Measuring microenvironment mechanical stress of rat liver during diethylnitrosamine induced hepatocarcinogenesis by atomic force microscope.* Microsc Res Tech, 2009. **72**(9): p. 672-8.

CHAPTER 7:

CONCLUSIONS AND FUTURE PERSPECTIVES

Authors: Shirley X. Zhang[1-3], Weian Zhao[1-6]

Affiliations:

[1]Department of Biomedical Engineering, University of California-Irvine, Irvine, California, 92697, USA.

[2]Edwards Life Sciences Center for Advanced Cardiovascular Technology, University of California-Irvine, Irvine, California, 92697, USA.

[3]Sue and Bill Gross Stem Cell Research Center, 845 Health Sciences Road, University of California-Irvine, Irvine, California, 92697, USA.

[4]Department of Pharmaceutical Sciences, University of California-Irvine, Irvine, California, 92697, USA.

[5]Chao Family Comprehensive Cancer Center, University of California-Irvine, Irvine, California, 92697, USA.

[6]Department of Biological Chemistry, University of California-Irvine, Irvine, California, 92697, USA.

7.1 Summary

In recent years, increasing attention has been focused on how mechanical properties of tissues can affect cell behavior. We have made great strides in understanding the scope of mechanotransduction, that everything from proteins to cells to entire organs are regulated by mechanical responses to forces such as flow, tension, and stiffness [1]. Many pathways and mechanisms of mechanotransduction in cells have also been elucidated, including the role of transcription factors such as YAP/TAZ in translating external biophysical cues into cell gene expression [2].

There have also been increasing interest and promising advances in studying mechanical properties of tissues. The ECM is now understood to be a dynamic environment, continuously being remodeled by resident cells and signaling cell behavior in return. In diseased states such as cancer, the precarious balance of ECM deposition and degradation during the matrix remodeling process is disturbed [3]. The excess deposition of interstitial matrix proteins along with increased expression of crosslinking agents such as LOX result in a stiffer microenvironment which contributes to abnormal cell behaviors.

The distinct stiffness of tumor tissues can act as a biomarker to target cancer, as discussed in this work. Currently, there is still a lack of effective treatments for metastatic cancer. Traditional cancer therapies are often non-specific, such as chemotherapy or radiation, and as a result lead to debilitating side-effects. More targeted therapies, using genetic or biochemical markers, can reduce off-target damage but often have low efficacy or cancer recurrence. This is mostly due to the innate heterogeneity of cancer, which can be observed not only across patient populations but also even within the same tumor. Even the well-studied genetic markers can only account for a low percentage of all cancers [4]. This heterogeneity means that patients often undergo multiple drug treatments which target different cancer markers. It also means that treatments which work on some cancer cells within a tumor may not work on others, leading to recurrence from the drug resistant cell population. Throughout decades of research, we have come to conclude that there is a need for different approaches to targeting cancer.

With more recent understanding of mechanotransduction, biophysical cues have emerged as a promising class of biomarkers with several advantages over genetic or molecular markers. In particular, the increased ECM deposition and stiffness is a hallmark of most solid tumors and sites of metastases, and presents similarly across populations. Also, the excess ECM is often not resolved in cancer, and persists for periods of months to years. The lack of heterogeneity and long half-life of stiffness makes it an attractive biomarker for targeting cancer.

Using this ideology, we have engineered MRCS to respond specifically to increased matrix stiffness as a novel method to target tumor tissues using only the mechanical properties of the ECM. In using MRCS to express CD to kill cancer, we have combined the efficacy of indiscriminate chemotherapy with the specificity of a targeted approach to achieve a therapeutic that can be both effective and precise.

While we have discussed and shown in this work that MSCs have natural tumor tropism and have higher retention within tumor tissues, the mechanisms and capacity of MSC homing remains under debate. The addition of the mechano-responsive element, however, seems sufficient to minimize off-target activation and tissue damage. Further studies will be needed to fully assess the behavior of MRCS *in vivo*, in a wider range of cancer models which can more closely recapitulate the nature of metastatic cancer found in human patients. Nevertheless, the use of matrix stiffness represents a new paradigm for targeting cancer and other fibrotic diseases. Beyond what was discussed in this work, the potential applications of biophysical cues as a class of biomarkers remain a new and expansive field for further exploration.

7.2 Perspectives

Given the versatility of mechano-responsive cells, there are many potential applications of this platform technology. Therapeutically, we have shown the potential of using MRCS to treat metastatic cancer. However, many other pathologies also display abnormal biophysical cues which can be targeted. For example, MRCS could be effective in ameliorating tissue stiffening which occurs in diabetes or aging, in preventing heart failure by treating cardiac fibrosis, or in wound healing by dissolving unresolved chronic fibrosis.

Beyond engineering MSCs, it is also possible to modify other cell types to have programmed responses to specific mechanical cues. Recently, immunotherapy has been a promising avenue of research for cancer therapy. In particular, CAR-T, T-cells with chimeric antigen receptors, have been in clinical trials to treat cancer. CAR-T function by the addition of a synthetic receptor to cancer-killing T-cells, which help them recognize and attach to specific antigens found on tumor cells. However, as with any biomarker, there is a risk of non-specific, off-target activation of the CAR-T, resulting in the killing of non-tumor cells. However, CAR-T can be additionally engineered with a mechano-responsive element so that the CAR is not expressed unless the T-cell is in a stiff microenvironment. By limiting the activation of the cancer-killing capabilities of CAR-T to only tumor tissues with increased stiffness, we can decrease the incidence of off-target activation and decrease harmful side effects.

This technology can also be used for the study of cell mechanobiology and tissue mechanics. The dynamic response between mechano-sensing and reporter expression can be used to study properties such as cell mechanical memory. This can, for example, be used to longitudinally study the plasticity of stem cells *in vivo* as a result of changing mechanical environments. We can also use these cell sensors to observe the dynamics of cell mechanical memory after conventional cell culture for research purposes, which is often conducted on stiff, plastic substrates, with implications for any cell-based studies or clinical applications that rely on specific cell behaviors which may be irreversibly modified by previous mechanical environments.

As discussed briefly in previous chapters, there is a need for better methods to interrogate tissue mechanics with better fidelity and precision. To study cancer biology, certain cancer cells themselves are also mechano-responsive and can be modified to express an array of reporters which activate on different ranges of physiological stiffness. These cell sensors will be able to answer many questions about cancer biology that we cannot currently interrogate with existing technologies. We can, for the first time, observe cancer development from the cell's perspective in their native microenvironment. With this new tool, we can correlate tumor mechanics and mechanical heterogeneity with cancer cell biochemical markers such as integrins and actins and cell/disease properties such as invasiveness, growth and drug resistance to illustrate the functional roles of mechanics in cancer. With bioinformatics, we can connect biophysical cues to genetic expression and gain insight into cancer mechanobiology. We can observe, in real time, the reciprocal remodeling of the ECM by tumor cells as the cancer grows. By understanding tumor mechanics at a cellular level, we may be able to identify better therapeutic strategies by starting at the underlying cause of abnormal cell behaviors and specifically modifying the biophysical properties of the cell microenvironment [5, 6].

Transgenic animal models created using mechano-responsive cell sensors can be a novel way to study disease progression or embryonic development. For example, transgenic MMTV-PyMT mice can be used to longitudinally monitor a spontaneous tumor model to observe cancer mechanics during tumor onset, progression, and metastasis. In another model, zebrafish embryos created using the sensor cells can illuminate tissue mechanics during organism development and growth.

Mechano-responsive cell sensors can also answer many general questions regarding cell fate in response to biophysical cues. Engineered epithelial cells can potentially report on their environment and be observed while undergoing epithelial-mesenchymal transition. Stem cell sensors can connect tissue mechanics with differentiation *in vivo*, whereas currently the study of stem cell differentiation in response to biophysical cues has been, by necessity, conducted in *in vitro* models.

In conclusion, this work presents a small subset of the potential capabilities of using mechano-responsive cells to target biophysical cues. Future work in this area will profoundly enhance our understanding of mechanotransduction, tissue mechanics, and disease progression, and lead to the development of improved methods for detection and therapeutics.

7.3 References

1. Orr, A.W., et al., *Mechanisms of mechanotransduction.* Developmental cell, 2006. **10**(1): p. 11-20.
2. Dupont, S., et al., *Role of YAP/TAZ in mechanotransduction.* Nature, 2011. **474**: p. 179.
3. Bonnans, C., J. Chou, and Z. Werb, *Remodelling the extracellular matrix in development and disease.* Nature reviews Molecular cell biology, 2014. **15**(12): p. 786.
4. Sounni, N.E. and A. Noel, *Targeting the tumor microenvironment for cancer therapy.* Clinical chemistry, 2013. **59**(1): p. 85-93.
5. Lampi, M.C. and C.A. Reinhart-King, *Targeting extracellular matrix stiffness to attenuate disease: From molecular mechanisms to clinical trials.* Science translational medicine, 2018. **10**(422): p. eaao0475.
6. Zhang, S.X., L. Liu, and W. Zhao, *Targeting Biophysical Cues: a Niche Approach to Study, Diagnose, and Treat Cancer.* Trends in cancer, 2018. **4**(4): p. 268-271.